HIGH-PRESSURE CYLINDRICAL ION TRAP MASS SPECTROMETRY

Derek Wayne Wolfe

A dissertation submitted to the faculty of the University of North Carolina at Chapel Hill in partial fulfillment of the requirements for the degree of Doctor of Philosophy in the Department of Chemistry.

Chapel Hill
2012

Approved by:

J. Michael Ramsey

James W. Jorgenson

Gary L. Glish

Steven A. Soper

Tomas Baer

ABSTRACT

DEREK WAYNE WOLFE: High-Pressure Cylindrical Ion Trap Mass Spectrometry
(Under the direction of J. Michael Ramsey)

This work describes the development of mass spectrometry (MS) instrumentation capable of operating at helium buffer gas pressures up to 1 torr. This is approximately three orders of magnitude higher than the pressures used in commercially available MS instrumentation. High-pressure operation is desirable since it reduces the size, weight, and power (SWaP) of the instrument by reducing the pumping system workload. A simple and rugged roughing pump could achieve these pressures while reducing SWaP by eliminating the turbo pump. Therefore this technology could be used to develop next generation hand-portable instruments and bring MS to new applications.

Custom MS instrumentation was designed and built to utilize 500 μm radius cylindrical ion trap (CIT) mass analyzers. Two vacuum chamber configurations were used to establish a performance baseline at traditional ion trap operating pressures. The instrument design was refined during these simple experiments before moving to high-pressure operation.

The feasibility of high-pressure CIT operation up to 1 torr was first demonstrated using a differentially pumped instrument. Electron ionization was performed and a mass-selective instability scan was used to eject ions into a low-pressure chamber for detection with an electron multiplier. Peak broadening effects at high pressure were reduced by increasing axial RF amplitude and ejecting ions into a low-pressure detection region.

Peak widths for Xe^+ spectra at pressures from 38.6 to 983.5 mTorr were analyzed and average peak widths for these low and high-pressure spectra were found to be relatively constant.

After demonstrating the CIT operation at high pressure, it was desirable to replace the electron multiplier with a pressure tolerant detector and simplify the instrument to a single vacuum chamber. The first experimental investigation of MS in this isobaric chamber at pressures up to 867 mTorr is reported. A solid-state capacitive transimpedance amplifier (CTIA) was used for ion detection at high pressures. Average peak widths for Xe^+ ions in spectra acquired at pressures from 133 to 867 mTorr were found to be nearly constant. Results presented here demonstrate mass spectra at ~1 torr using a solid-state ion detector capable of operating at atmospheric pressure for MS applications requiring portability.

Dedicated to my family

ACKNOWLEDGEMENTS

I would like to thank my advisor, J. Michael Ramsey, for the opportunity to work in his research group and for his support and guidance of my research. I also thank all the members of the Ramsey group for their help and discussions over the past 5 years. In particular, I thank Travis Falconer for helping me get started on this research. Much of my present achievements would not have been possible without his invaluable MS insight during my early years as a graduate student. I also thank J.P. Alarie, Tina Stacy, and Rose Ramsey for help throughout my graduate career and especially for editing my writing. Finally, I would like to thank my family and friends for their support which helped me get to this point.

TABLE OF CONTENTS

LIST OF TABLES

LIST OF FIGURES

LIST OF ABBREVIATIONS AND SYMBOLS

MS	mass spectrometry
SWaP	size, weight, and power consumption
DAPI	discontinuous atmospheric pressure inlet
CW	chemical warfare
TIC	toxic industrial compound
QIT	quadrupole ion trap
HV	high voltage
RF	radio frequency
3D	three dimensional
CIT	cylindrical ion trap
RIT	rectilinear ion trap
FWHM	full width at half maximum
LIT	linear ion trap
FC	faraday cup
LOD	limit of detection
CTIA	capacitive transimpedance amplifier
CF	conflate
EI	electron ionization
CNC	computer numerical control
CAD	computer-aided design
EM	electron multiplier

IC	integrated circuit
SSR	solid-state relay
SPDT	single pole double throw
GUI	graphical user interface
DAQ	data acquisition
S/N	signal to noise ratio
ppth	part per thousand
CV	constant voltage
CC	constant current
IT	ionization time
LP	low pass
EB	emitter bias

CHAPTER 1

INTRODUCTION

1.1 Portable MS

Interest in portable mass spectrometry (MS) has increased due to applications where rapid in situ or field measurements are critical.[1-18] Conventional mass spectrometers are unsuitable for these situations because their large size, weight, and power consumption (SWaP) confine them to the laboratory.[3] Additionally, the turbo pumps required to maintain high vacuum conditions are costly and fragile due to their ≈90,000 RPM operational speeds. Miniaturized vacuum pumps have made mass spectrometers luggable but hand portability is still limited due to overall system SWaP, low pumping capacity, and lack of pumping system robustness.[10-12, 15] Two strategies to overcome decreased pumping capacity in miniaturized mass spectrometers are high-pressure instrument operation and restricted sample inlet flow rate.[14, 19] Restricted flow through a small orifice decreases gas conductance but at the cost of reduced ion throughput and sensitivity. One alternative to address this limitation is a cycled inlet valve (e.g. discontinuous atmospheric pressure inlet - DAPI) to sample at atmospheric pressure and subsequently pinch off the sample inlet to pump-down to operational pressures.[15, 20] In this case, the time delay required to reach suitable analysis pressures decreases instrument duty cycle, limiting its utility for rapid field analysis.

High-pressure operation is a more attractive strategy than restricted sample flow since a high-pressure instrument could have a significant reduction in SWaP while

maintaining sensitivity and duty cycle. High-pressure MS instrumentation would greatly improve portability by reducing the vacuum pump workload[19] and overall system size while creating a simpler and more robust vacuum system.[21] Ideally the turbo pump could be eliminated to simplify the pumping system to a rugged and relatively inexpensive roughing pump. This new generation of high-pressure MS instruments would be useful for applications such as in situ detection of chemical warfare (CW) agents and toxic industrial compounds (TICs) where hand portability is required.

1.2 Quadrupole ion traps

Quadrupole ion traps (QITs) were first disclosed in 1953 by Paul and Steinwedel.[22] They are commonly used as ion storage devices and mass analyzers for a wide range of mass spectrometry applications. A QIT consists of a confined volume formed by stacking a hyperbolic endcap electrode on either side of a larger diameter ring electrode (Figure 1.1). A QIT is typically operated by applying a high voltage (HV) radio-frequency (RF) sine wave to the ring electrode while holding the endcap electrodes at ground potential. This configuration creates a quadrupolar electric field in the center of the trap and allows the QIT to trap ions in the resulting potential energy well. The geometry of the QIT is described by the distance from the trap center to both the ring electrode (r_0) and endcap electrode (z_0). The ideal QIT geometry is predicted to occur when $r_0^2 = 2z_0^2$.

The three dimensional (3D) electric field inside the QIT can be found by solving the Laplace equation.[23] The resulting potential inside the trap can be represented by a sum of polynomial terms as shown below with A_2, A_3, and A_4 representing the quadrupolar, hexapolar, and octapolar weighting coefficients, respectively.

$$\phi_{r,z} = \phi_0 \left[A_2 \frac{(r^2 - 2z^2)}{2r_0^2} + A_3 \frac{(3r^2 z - 2z^3)}{2r_0^3} + A_4 \frac{(3r^4 - 24r^2 z^2 + 8z^4)}{8r_0^2} + \cdots \right]$$

Where: φ_0 = potential applied to ring electrode
r = radial distance from trap center
z = axial distance from trap center
r_0 = trap radius
A_n = weighting coefficient for n^{th} order field

In this equation, the weighting coefficient (A_n) for each field component describes how much of the n^{th} order field is present in the 3D electric field. In an ideal case, the QIT electrodes extend infinitely and create an electric field that is purely quadrupolar where $A_3 = A_4 = 0$ (Figure 1.2). In this purely quadrupolar electric field, forces applied to an ion are uncoupled in the r and z dimensions. This is represented mathematically in the equation for $\varphi_{r,z}$ by the fact that there are no "cross terms" containing the product of r and z. Consequently, force applied in one dimension doesn't affect the motion of the ions in the other dimension. This allows the user to add energy only in the z dimension of the trap and eject ions toward the detector in a narrow beam. However, it is not feasible to construct a QIT that produces purely quadrupolar (A_2) fields because of the non-idealities introduced by truncated electrodes and endcap holes for ion transmission. This results in A_3, A_4, and higher order coefficients with non-zero values. Since the fundamental QIT theory was developed under the assumption of perfectly quadrupolar electric fields, these higher order field components can cause deviations from ideal QIT behavior. Early commercial ion traps compensated for these higher order fields with a configuration where the QIT was "stretched" by a 10.6% increase in z_0.[24] This modification to the trap geometry helps to offset the detrimental higher order field effects introduced by imperfect electrodes.

A working theoretical knowledge of the QIT is necessary to understand the experiments presented here. A full theoretical explanation can be found in the literature and will not be presented in great detail here.[23] The fundamental theory underlying QIT operation is derived from the Mathieu equation which mathematically describes the motion of ions in a quadrupolar electric field.

$$\frac{d^2u}{d\xi^2} + (a_u - 2q_u \cos 2\xi)u = 0$$

Where: u = displacement
ξ = dimensionless parameter = $\Omega t / 2$
a_u = stability parameter
q_u = stability parameter

The solutions to this second order linear differential equation yield two equations for the dimensionless trapping parameters a_z and q_z which relate experimental parameters to the stability of an ion in the z dimension inside the trap.

$$a_z = -\frac{16eU}{m(r_0^2 + 2z_0^2)\Omega^2}$$

$$q_z = \frac{8eV}{m(r_0^2 + 2z_0^2)\Omega^2}$$

Where: e = charge of the ion
U = DC potential applied to the ring
V = AC amplitude applied to the ring
m = mass of the ion
r_0 = trap radius
z_0 = trap half length
Ω = drive RF frequency

If a stable ion is defined as having a trajectory that is periodic around the center of the trap, regions of stability in the r and z dimensions can be plotted in a_z vs. q_z space to form the QIT stability diagram (Figure 1.3). The ion is considered stable inside the trap where the regions of stability in the r and z dimensions overlap. Although there are a few of

these overlapping regions of stability, the first region is used almost exclusively because it is experimentally easiest to achieve due to lower required voltages (Figure 1.4). The stability of an ion can be predicted by calculating the value of a_z and q_z for the ion of interest and drawing a point on the stability diagram. If the resulting point lies inside the overlapping regions of r and z stability the ion is determined to be stable inside the trap. However, in a typical ion trap experiment there is no DC voltage applied to the ring electrode which results in an a_z value of 0. Therefore it is only necessary to have a q_z value below 0.908 for an ion to be trapped.

QITs are typically operated with a low mass buffer gas such as helium at pressures of ≈1 mTorr for improved resolution. The neutral helium atoms undergo collisions with trapped ions and remove kinetic energy in small increments. This "collisional cooling" causes the ion orbits to collapse toward the center of the trap. The result is a smaller potential energy spread between ions of the same *m/z* and consequently improved resolution as the ions reach the detector with less temporal variation. Sensitivity is also improved as a higher percentage of ions are near the axis of the trap and therefore will eject through the endcap hole toward the detector instead of being lost by striking an electrode.

To further improve QIT resolution, a low voltage supplementary AC signal can be applied to an endcap electrode to perform resonance ejection. The frequency of the supplementary AC corresponds to the frequency of oscillation (secular frequency) which all ions achieve before becoming unstable in the trap and is less than the drive RF frequency. When an ion reaches the resonant point in the mass scan it absorbs energy from the matching supplemental AC signal and is ejected from the trap rapidly. This

results in a smaller temporal variation for ions of a given *m/z* and therefore narrower peak widths and improved resolution. Resonance ejection also extends the mass range of the QIT by ejecting ions at a q_z value below 0.908, thus a larger *m/z* ion can be ejected from the trap with a given RF amplitude value.

A QIT becomes a mass spectrometer by selectively ejecting different *m/z* values as a function of time. A common method to achieve this is via a mass selective instability scan. In this experiment, ions or electrons are first gated into the trap through small holes in the entrance endcap. The ions of interest are trapped and the drive RF amplitude is then ramped linearly to increase the q_z value for all ions in the trap. Eventually the q_z value for a given *m/z* reaches 0.908 and those ions become unstable in the z dimension and are ejected from the trap through holes in the endcaps to be detected. In this fashion the ions are sequentially scanned out from lowest to highest *m/z* value to produce the familiar mass spectrum.

QITs are a popular mass analyzer for portable or high-pressure mass spectrometry due to their relatively high-pressure operation and tandem MS capabilities.[1, 6-8, 10-11, 13, 15, 19] It is known that mTorr pressures of He buffer gas improve ion trap efficiency and resolution[21, 23-26] while similar pressures degrade performance in other mass analyzers.[11, 15] Therefore ion traps have an advantage over other mass analyzer designs for high-pressure mass spectrometry applications. However, to have a significant effect on pumping demands the operational pressures need to increase by several orders of magnitude making conventional QITs inappropriate. Although ion traps can operate at elevated pressures relative to other mass analyzers, special considerations must be taken to further increase operational pressures beyond a few tens of mTorr. It is known that

high buffer gas pressures will cause performance degradation in an ion trap as a reduced mean free path results in more frequent collisions between ions and neutral molecules. However, Whitten *et. al.* predicted that performance degradation at high pressures can be offset by increasing the RF drive frequency and decreasing trap size to maintain mass resolution.[3] Therefore, miniaturizing the ion trap is necessary to achieve truly high-pressure operation. Optimizing the axial RF amplitude can also help to maintain a strong signal by offsetting the effects of increased numbers of collisions at high pressures.[19, 21]

1.3 Cylindrical ion traps

To achieve a significant increase in QIT operating pressure it is necessary to construct traps that are much smaller than the conventional r_0 = 1 cm size. However, it becomes extremely difficult to fabricate hyperbolic electrode shapes at very small sizes because conventional machining inaccuracies represent an increasingly large percentage of the overall trap geometry. If the trap dimensions pass below the capabilities of conventional machining techniques, microfabrication techniques become appropriate but are unable to produce the desired hyperbolic electrode shape. Therefore, to realize trap miniaturization it is desirable to use a simplified version of the hyperbolic QIT geometry that is easier to fabricate but still produces electric fields that are largely quadrupolar. The cylindrical ion trap (CIT) shown in Figure 1.5 is one such geometry and is much easier to fabricate on a miniaturized scale while still functioning as a quadrupole ion trap.[1, 4, 15, 27-32] A CIT consists of simple planar electrodes with cylindrical holes making it amenable to much smaller dimensions using both conventional and microfabrication techniques. Although the shape of the cylindrical CIT electrode profile differs from the hyperbolic QIT electrodes, the CIT still produces electric fields that are largely

quadrupolar (Figure 1.6). However, non-idealities introduced by the electrode shape and endcap holes result in higher-order electric field components in the CIT.[23]

1.4 Ion trap arrays

A disadvantage of miniaturized CITs is that the charge capacity of a single trap decreases with the trap radius (r). However, the area of the trap decreases as r^2 so total charge capacity can be maintained in a given area by employing CIT arrays where multiple traps operate in parallel. This is a convenient strategy because switching from a single trap to an array doesn't require any modifications to the experiment. An array of miniaturized CITs is also significantly smaller than a conventional QIT since volume decreases as r^3. When using a CIT array it is important to ensure each individual trap is fabricated with the best possible positional accuracy and consistent dimensions for the best performance. If there are variations in hole position or size the array elements will not function identically and the resolution of the instrument will be degraded by ions of a given *m/z* ejecting at different times from different traps. Due to inevitable differences between individual traps, the resolution in a CIT array will be limited by the precision of the machining technique utilized and cannot exceed that of a single trap. However, for a properly constructed CIT array the loss in resolution is minimal and typically insignificant.

1.5 High-pressure trap operation

There are relatively few examples of high-pressure MS in the literature. The highest pressure experimental results were generated by Song *et. al.* using a rectilinear ion trap (RIT) instrument to explore MS performance at elevated pressures.[19] The authors demonstrated full width half max (FWHM) peak widths of 2 *m/z* with the RIT

operating at 50 mTorr with air buffer gas. Further experimental exploration of high-pressure MS operation in this instrument was limited by electrical discharge above these pressures. Using theoretical models the authors predicted FWHM peak widths of 9.5 *m/z* for their instrument operating with air buffer gas at 250 mTorr.[21] The RIT was predicted to be capable of mass analysis at pressures of several hundred mTorr but with increasingly degraded resolution.

Previous experiments with microscale CITs utilized a trap with a radius (r_0) of 500 μm operating at pressures of ≈3 mTorr using He buffer gas.[33-35] This trap configuration was used as a basis for the work presented here since it should theoretically be capable of operating at buffer gas pressures significantly higher than the 1 mTorr levels typically used in conventional r_0 = 1 cm hyperbolic QITs.[3] However, to perform MS at these pressures it was necessary to design a differentially pumped vacuum system to maintain a low-pressure chamber for effective electron multiplier operation.

1.6 High-pressure detector

With current technology the detector is the limiting factor in high-pressure MS. There are many examples of high-pressure ionization sources, and mass analysis has recently been demonstrated at high pressures (Chapter 4), but detector technology has seen less development. The electron multiplier is the most common ion detector used in MS instruments due to its high gain and low noise characteristics.[36-37] However, electron multipliers are unable to operate at pressures above a few mTorr due to an ion feedback mechanism that saturates the output and damages the surface coating.[38-40] Furthermore, sustained operation at even moderately elevated pressures will accelerate degradation of the surface coating and shorten the useful lifetime of the multiplier. Therefore it is

necessary to replace the electron multiplier with a pressure tolerant ion detector to truly achieve high-pressure portable MS. Ideally the detector would be capable of operating at any pressure which would allow for a simplified single chamber vacuum system.

One alternative is Fourier transform image current detectors that have been used in CITs without buffer gas[41] and in linear ion traps (LITs) up to 50 mTorr[42]. Although image current detectors don't suffer from the breakdown issues of the electron multiplier, they require long lasting ion motions. At high pressures the large numbers of collisions between ions and neutral gas molecules makes this detector design ineffective. Long detection times would also reduce the spectral acquisition rate of the instrument and increase the overall analysis time.

Solid-state Faraday cup (FC) detectors are a second alternative type of detector that are pressure tolerant.[37] They are also independent of ion energy, stable, inexpensive, measure positive and negative ions, and operate with low voltages. However, they are generally less sensitive than an electron multiplier and require careful design to measure a usable signal.[36, 38, 43-44] These FC detectors can either be configured to measure current or charge from incoming ions. Those that measure current (electrometers) rely on a large feedback resistor for sufficient gain. The small ion currents from a microscale CIT require a very high gain, which would decrease the time response of the detector and limit peak resolution. Furthermore, the limit of detection (LOD) in an electrometer circuit is typically dominated by thermal (Johnson) noise in the feedback resistor which increases with gain.[37, 40] FC detectors that measure charge (integrators) rely on a very small feedback capacitor to store the collected charge. The gain of these detectors is inversely proportional to the feedback capacitance which allows for high gain without

decreasing the time response of the detector. Another advantage is a lower detector read noise and LOD resulting from the inherently superior noise characteristics of a capacitor. An example of a charge detector design is the capacitive transimpedance amplifier (CTIA) which integrates incoming ion current on a feedback capacitor and produces a proportional output voltage. This detector technology has been previously described in detail in the literature.[36] CTIA technology has the same high-pressure advantages as an electrometer but is generally more sensitive due to the ability to microfabricate extremely small fF range capacitors directly on silicon.[45] This makes direct electronic detection of ions via charge integration feasible. There are several reports of these CTIA detectors configured in an array format with up to 1696 individual channels.[36, 40, 44, 46-49] They have been used primarily on magnetic sector MS instruments where they can simultaneously detect multiple *m/z* values across the array. Single channel CTIA detectors have also been demonstrated to operate at atmospheric pressure in an ion mobility spectrometer.[45] Another home built charge detector has been reported to work up to approximately 50 mTorr in a CIT MS but the detector was not described in detail.[50]

Although alternate detector technologies exist, there are relatively few options for pressure tolerant detectors with sufficient gain and time response to detect small numbers of ions arriving on μs time scales from an ion trap. The work presented here uses a second generation single channel CTIA as a pressure tolerant ion detector for an isobaric microscale CIT instrument.

1.7 Objectives

This dissertation describes the development and characterization of MS at buffer gas pressures up to 1 torr. To investigate this previously unexplored region of high-

pressure MS, it was necessary to develop custom high-pressure MS instrumentation (Chapter 2). The instrument was then characterized at typical ion trap operating pressures to empirically optimize various experimental parameters and ensure proper system operation (Chapter 3). High-pressure CIT operation was then performed to demonstrate the feasibility of mass analysis at high pressures (Chapter 4). Finally, high-pressure MS experiments were performed using a pressure tolerant solid-state CTIA detector to demonstrate high-pressure MS in a single vacuum chamber (Chapter 5). This work demonstrates the ability to perform MS at very high pressures which could be achieved with a simple and rugged roughing pump. This represents a significant step toward the next generation of portable MS instrumentation.

1.8 Tables and figures

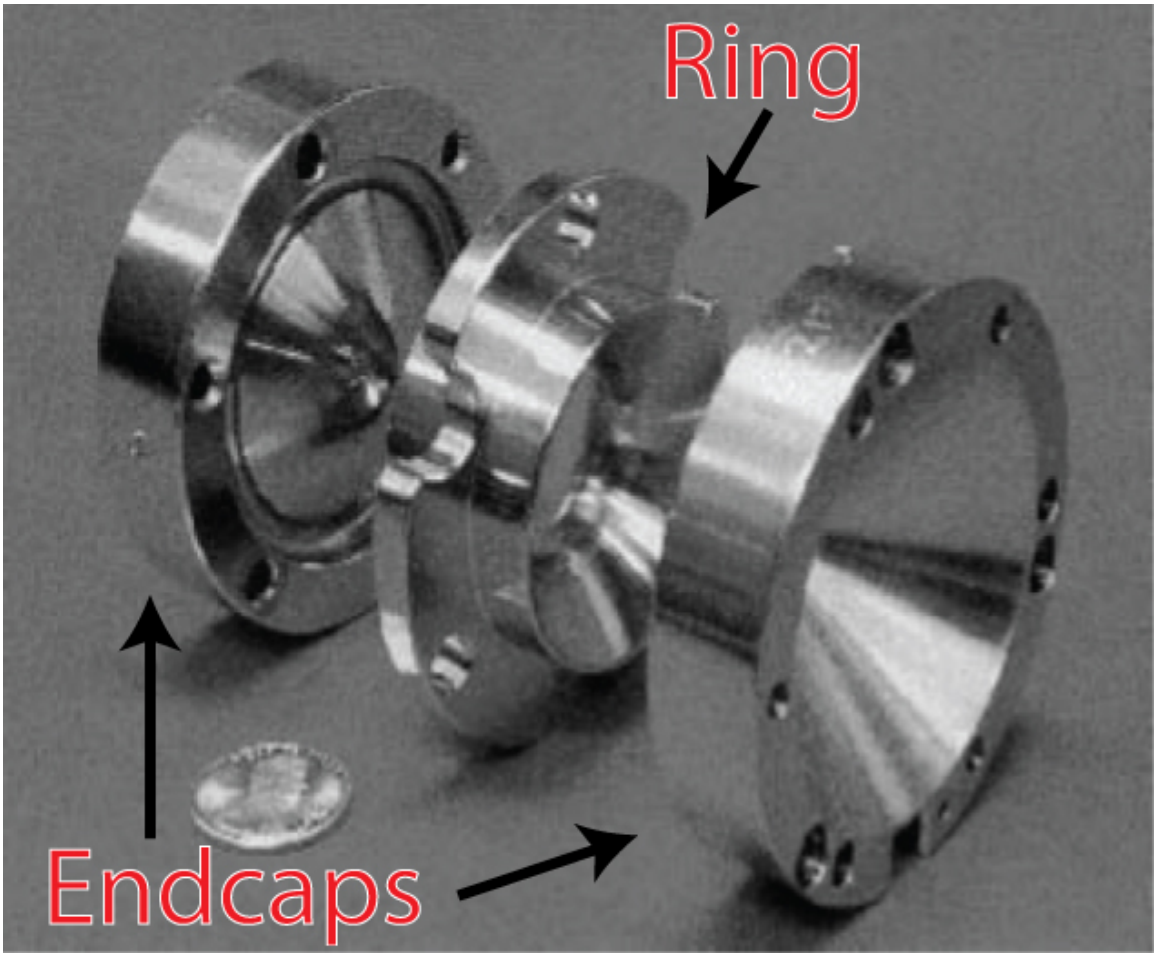

Figure 1.1: Exploded view of a commercial QIT showing the hyperbolic electrode geometry.[23]

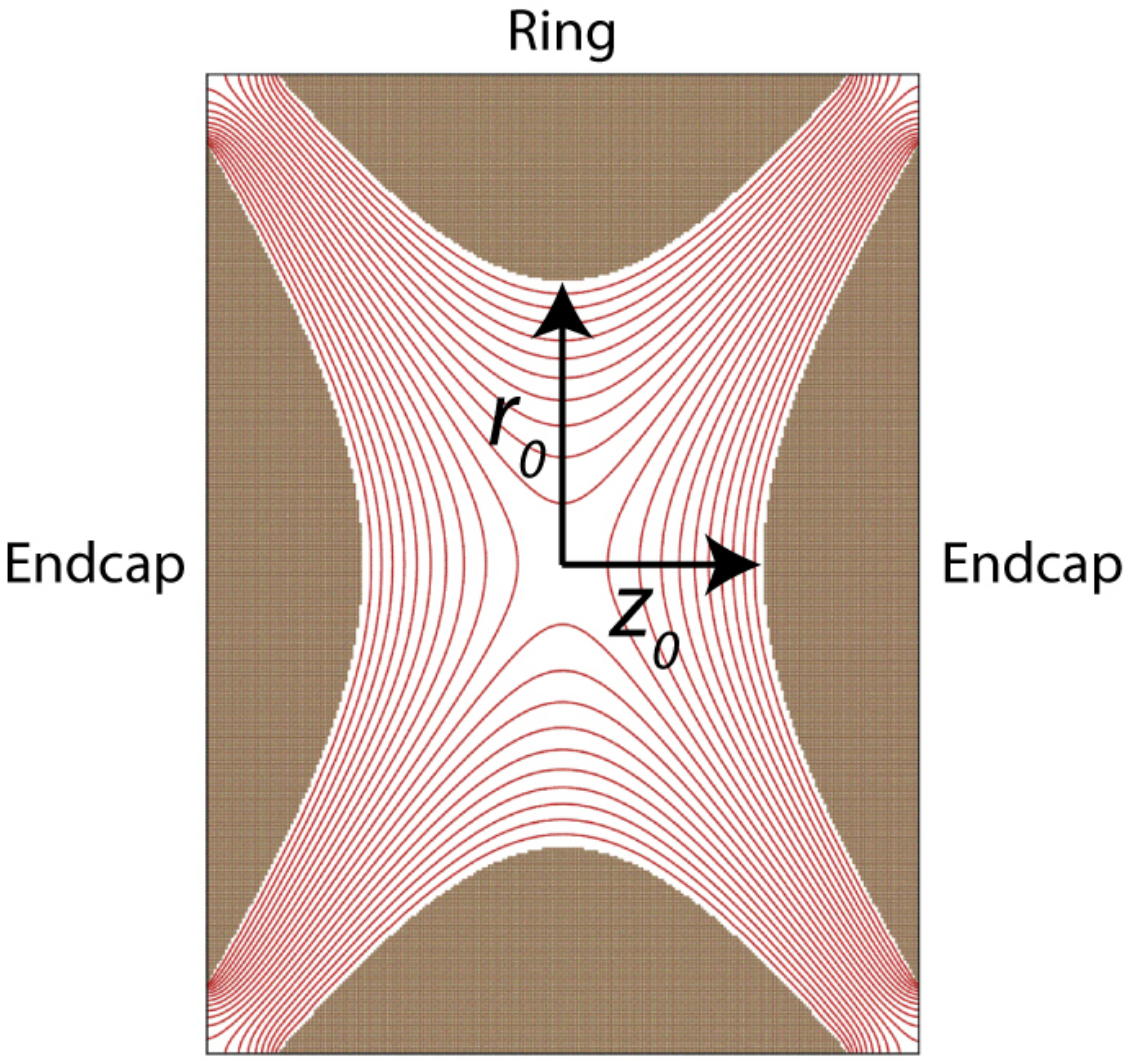

Figure 1.2: SIMION simulation showing the quadrupolar electric field inside a QIT. Critical dimensions r_0 (trap radius) and z_0 (trap half length) describe the trap geometry.

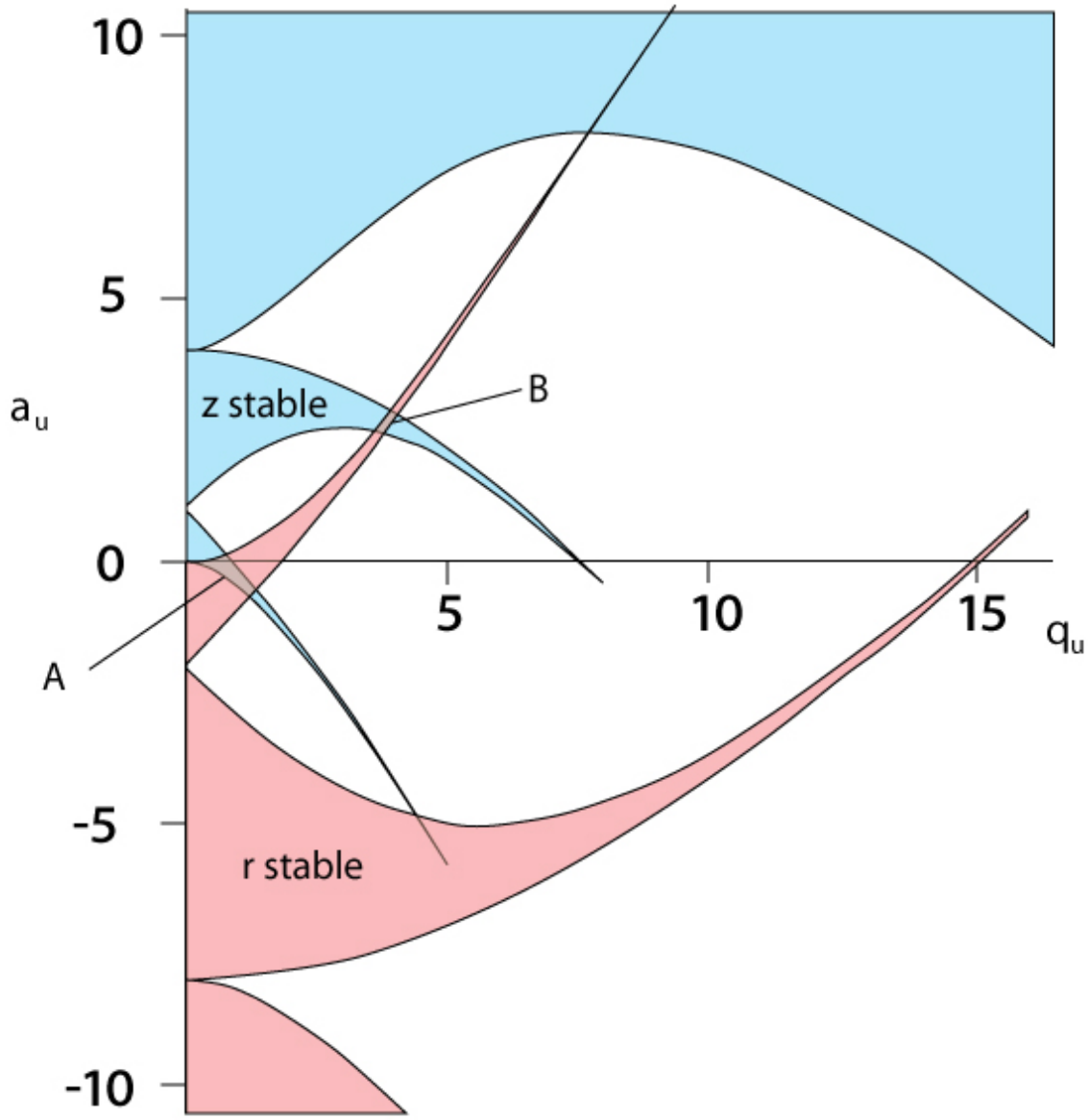

Figure 1.3: The stability diagram derived from the Mathieu equation describes regions of r and z dimension stability plotted in (a_z, q_z) space. Ions are predicted to be trapped in regions where the r and z dimension stability overlap (labeled A and B).[24]

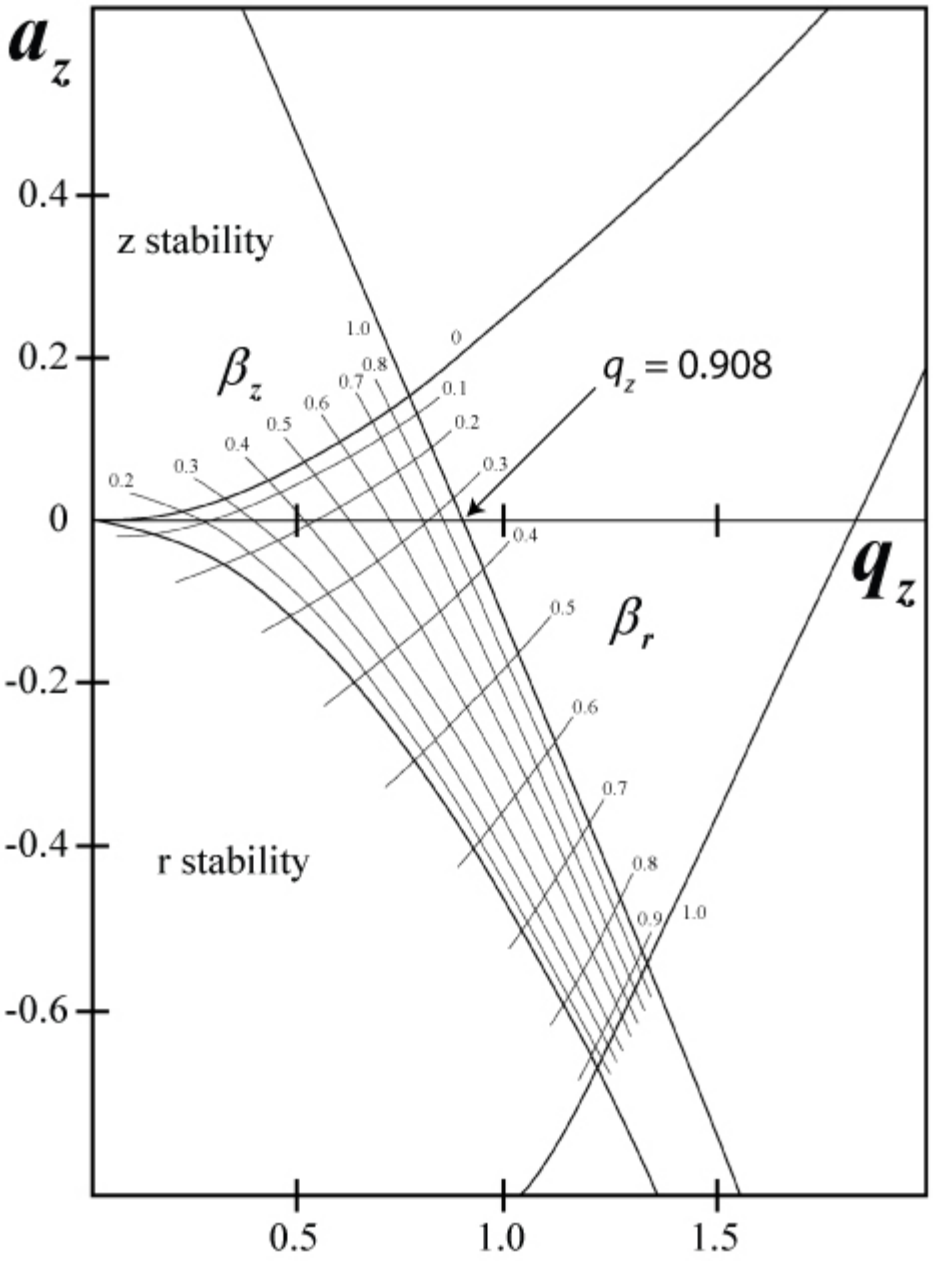

Figure 1.4: QIT stability region "A" close-up view. In a typical experiment $a_z = 0$ so the ion is stable for $q_z < 0.908$. A mass-selective instability scan increases the q_z value for a given *m/z* ion until it reaches 0.908 and passes the stability boundary thus ejecting from the trap.[23] The iso-β_r and iso-β_z lines are shown in this diagram.

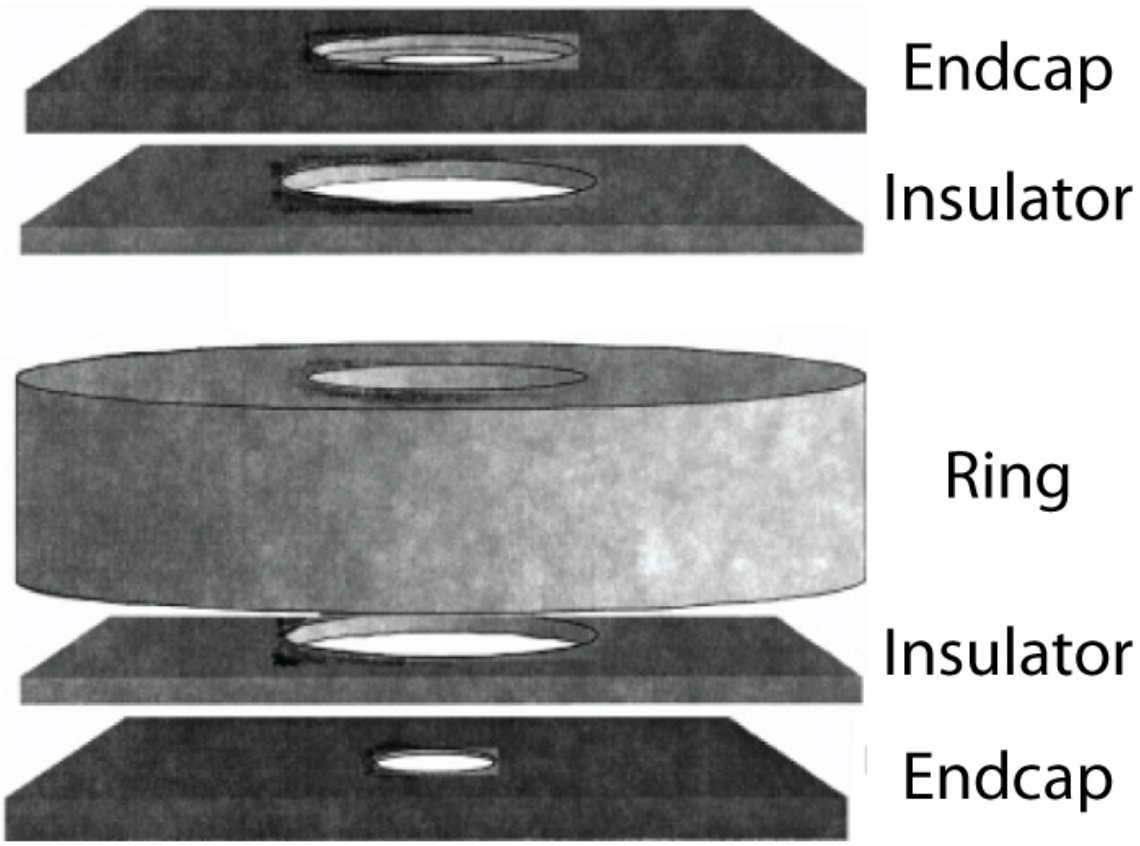

Figure 1.5: Exploded view of a CIT showing the simplified electrode geometry with cylindrical hole profiles.[27]

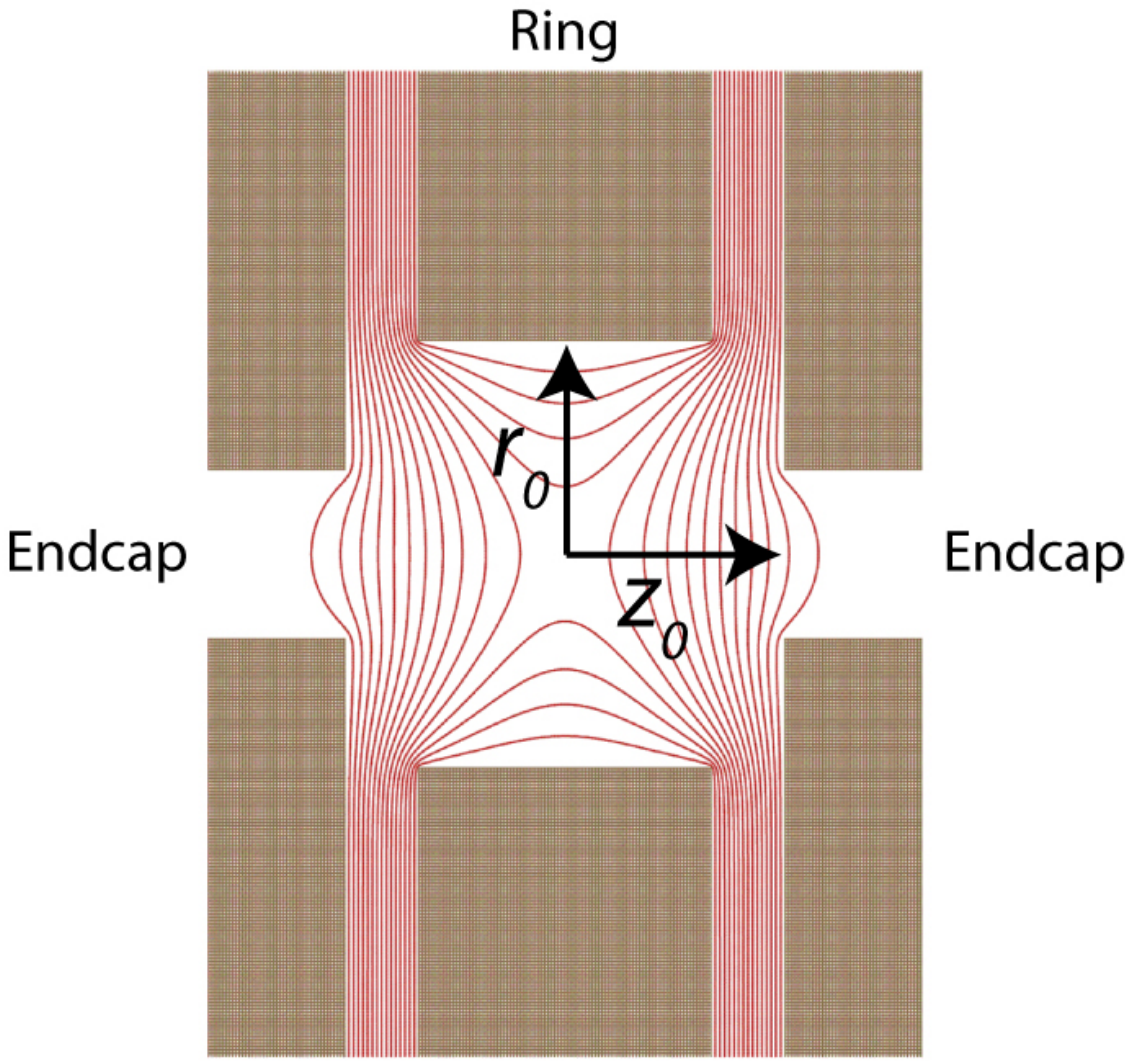

Figure 1.6: SIMION simulation showing the electric field inside a microscale CIT. Although the field is largely quadrupolar, some higher order field components are introduced due to non-idealities near the electrodes and endcap holes. Critical dimensions r_0 (trap radius) and z_0 (trap half length) describe the trap geometry.

1.9 References

(1) Patterson, G. E.; Guymon, A. J.; Riter, L. S.; Everly, M.; Griep-Raming, J.; Laughlin, B. C.; Zheng, O.; Cooks, R. G., *Anal. Chem.* 2002, *74*, 6145-6153.

(2) Chaudhary, A.; van Amerom, F. H. W.; Short, R. T.; Bhansali, S., *Int J Mass Spectrom* 2006, *251*, 32-39.

(3) Whitten, W. B.; Reilly, P. T.; Ramsey, J. M., *Rapid Commun. Mass Spectrom.* 2004, *18*, 1749-52.

(4) Van Amerom, F. H. W.; Chaudhary, A.; Cardenas, M.; Bumgarner, J.; Short, R. T., *Chem. Eng. Commun.* 2008, *195*, 98 - 114.

(5) Yang, M.; Kim, T.-Y.; Hwang, H.-C.; Yi, S.-K.; Kim, D.-H., *J. Am. Soc. Mass Spectrom.* 2008, *19*, 1442-1448.

(6) Ouyang, Z.; Noll, R. J.; Cooks, R. G., *Anal. Chem.* 2009, *81*, 2421-2425.

(7) Blain, M. G.; Riter, L. S.; Cruz, D.; Austin, D. E.; Wu, G.; Plass, W. R.; Cooks, R. G., *Int J Mass Spectrom* 2004, *236*, 91-104.

(8) Fico, M.; Yu, M.; Ouyang, Z.; Cooks, R. G.; Chappell, W. J., *Anal. Chem.* 2007, *79*, 8076-8082.

(9) Ferran, R. J.; Boumsellek, S., *J. Vac. Sci. Technol. A* 1996, *14*, 1258-1265.

(10) Contreras, J. A.; Murray, J. A.; Tolley, S. E.; Oliphant, J. L.; Tolley, H. D.; Lammert, S. A.; Lee, E. D.; Later, D. W.; Lee, M. L., *J. Am. Soc. Mass Spectrom.* 2008, *19*, 1425-1434.

(11) Gao, L.; Song, Q.; Patterson, G. E.; Cooks, R. G.; Ouyang, Z., *Anal. Chem.* 2006, *78*, 5994-6002.

(12) Gao, L.; Sugiarto, A.; Harper, J. D.; Cooks, R. G.; Ouyang, Z., *Anal. Chem.* 2008, *80*, 7198-7205.

(13) Edwards, G. D.; Shepson, P. B.; Grossenbacher, J. W.; Wells, J. M.; Patterson, G. E.; Barket, D. J.; Pressley, S.; Karl, T.; Apel, E., *Anal. Chem.* 2007, *79*, 5040-5050.

(14) Keil, A.; Talaty, N.; Janfelt, C.; Noll, R. J.; Gao, L.; Ouyang, Z.; Cooks, R. G., *Anal. Chem.* 2007, *79*, 7734-9.

(15) Ouyang, Z.; Cooks, R. G., *Annu. Rev. Anal. Chem.* 2009, *2*, 187-214.

(16) Smith, J. N.; Noll, R. J.; Cooks, R. G., *Rapid Commun. Mass Spectrom.* 2011, *25*, 1437-1444.

(17) Orient, O. J.; Chutjian, A., *Rev. Sci. Instrum.* 2002, *73*, 2157-2160.

(18) Keil, A.; Hernandez-Soto, H.; Noll, R. J.; Fico, M.; Gao, L.; Ouyang, Z.; Cooks, R. G., *Anal. Chem.* 2008, *80*, 734-741.

(19) Song, Q.; Xu, W.; Smith, S. A.; Gao, L.; Chappell, W. J.; Cooks, R. G.; Ouyang, Z., *J. Mass Spectrom.* 2010, *45*, 26-34.

(20) Gao, L.; Cooks, R. G.; Ouyang, Z., *Anal. Chem.* 2008, *80*, 4026-4032.

(21) Xu, W.; Song, Q.; Smith, S. A.; Chappell, W. J.; Ouyang, Z., *J. Am. Soc. Mass Spectrom.* 2009, *20*, 2144-53.

(22) Paul, W.; Steinwedel, H., *Zeitschrift fuer Naturforschung* 1953, *a8*, 448-450.

(23) March, R. E., *Mass Spectrom. Rev.* 2009, *28*, 961-989.

(24) March, R. E., *J. Mass Spectrom.* 1997, *32*, 351-369.

(25) Badman, E. R.; Cooks, R. G., *Anal. Chem.* 2000, *72*, 3291-7.

(26) Stafford Jr, G. C.; Kelley, P. E.; Syka, J. E. P.; Reynolds, W. E.; Todd, J. F. J., *Int. J. Mass Spectrom. Ion Processes* 1984, *60*, 85-98.

(27) Kornienko, O.; Reilly, P. T. A.; Whitten, W. B.; Ramsey, J. M., *Rapid Commun. Mass Spectrom.* 1999, *13*, 50-53.

(28) Wells, J. M.; Badman, E. R.; Cooks, R. G., *Anal. Chem.* 1998, *70*, 438-444.

(29) Bonner, R. F.; Fulford, J. E.; March, R. E.; Hamilton, G. F., *Int. J. Mass Spectrom. Ion Phys.* 1977, *24*, 255-269.

(30) Pau, S.; Pai, C. S.; Low, Y. L.; Moxom, J.; Reilly, P. T.; Whitten, W. B.; Ramsey, J. M., *Phys. Rev. Lett.* 2006, *96*, 120801.

(31) Ouyang, Z.; Wu, G.; Song, Y.; Li, H.; Plass, W. R.; Cooks, R. G., *Anal. Chem.* 2004, *76*, 4595-4605.

(32) Beaty, E. C., *J. Appl. Phys.* 1987, *61*, 2118-2122.

(33) Moxom, J.; Reilly, P. T.; Whitten, W. B.; Ramsey, J. M., *Anal. Chem.* 2003, *75*, 3739-43.

(34) Moxom, J.; Reilly, P. T. A.; Whitten, W. B.; Ramsey, J. M., *Rapid Commun. Mass Spectrom.* 2002, *16*, 755-760.

(35) Moxom, J.; Reilly, P. T. A.; Whitten, W. B.; Ramsey, J. M., *Rapid Commun. Mass Spectrom.* 2004, *18*, 721-723.

(36) Knight, A. K.; Sperline, R. P.; Hieftje, G. M.; Young, E.; Barinaga, C. J.; Koppenaal, D. W.; Denton, M. B., *Int J Mass Spectrom* 2002, *215*, 133-139.

(37) Koppenaal, D. W.; Barinaga, C. J.; Denton, M. B.; Sperline, R. P.; Hieftje, G. M.; Schilling, G. D.; Andrade, F. J.; Barnes, J. H. I. V., *Anal. Chem.* 2005, *77*, 418A-427A.

(38) Barnes, J. H.; Hieftje, G. M., *Int J Mass Spectrom* 2004, *238*, 33-46.

(39) Bower, C. A.; Gilchrist, K. H.; Lueck, M. R.; Stoner, B. R., *Sensors and Actuators, A: Physical* 2007, *A137*, 296-301.

(40) Lorincik, J.; Denton, M. B.; Sperline, R. P.; Young, E. T.; Williams, P., *Anal. Lett.* 2011, *44*, 1050-1057.

(41) Badman, E. R.; Wells, J. M.; Bui, H. A.; Cooks, R. G., *Anal. Chem.* 1998, *70*, 3545-3547.

(42) Xu, W.; Maas, J. B.; Boudreau, F. J.; Chappell, W. J.; Zheng, O. Y., *Anal. Chem.* 2011, *83*, 685-689.

(43) Darling, R. B.; Scheidemann, A. A.; Bhat, K. N.; Chen, T. C., *Sensors and Actuators, A: Physical* 2002, *95*, 84-93.

(44) Schilling, G. D.; Shelley, J. T.; Barnes, J. H.; Sperline, R. P.; Denton, M. B.; Barinaga, C. J.; Koppenaal, D. W.; Hieftje, G. M., *J. Am. Soc. Mass Spectrom.* 2010, *21*, 97-103.

(45) Babis, J. S.; Sperline, R. P.; Knight, A. K.; Jones, D. A.; Gresham, C. A.; Denton, M. B., *Anal. Bioanal. Chem.* 2009, *395*, 411-419.

(46) Schilling, G. D.; Ray, S. J.; Rubinshtein, A. A.; Felton, J. A.; Sperline, R. P.; Denton, M. B.; Barinaga, C. J.; Koppenaal, D. W.; Hieftje, G. M., *Anal. Chem.* 2009, *81*, 5467-5473.

(47) Rubinshtein, A. A.; Schilling, G. D.; Ray, S. J.; Sperline, R. P.; Denton, M. B.; Barinaga, C. J.; Koppenaal, D. W.; Hieftje, G. M., *J. Anal. Atom. Spectrom.* 2010, *25*, 735-738.

(48) Schilling, G. D.; Ray, S. J.; Sperline, R. P.; Denton, M. B.; Barinaga, C. J.; Koppenaal, D. W.; Hieftje, G. M., *J. Anal. Atom. Spectrom.* 2010, *25*, 322-327.

(49) Felton, J. A.; Schilling, G. D.; Ray, S. J.; Sperline, R. P.; Denton, M. B.; Barinaga, C. J.; Koppenaal, D. W.; Hieftje, G. M., *J. Anal. Atom. Spectrom.* 2011, *26*, 300-304.

(50) Zhu, Z. Q.; Xiong, C. Q.; Xu, G. P.; Liu, H.; Zhou, X. Y.; Chen, R.; Peng, W. P.; Nie, Z. X., *Analyst* 2011, *136*, 1305-1309.

CHAPTER 2

INSTRUMENTATION

2.1 Introduction

Since there is no source for commercially available high-pressure MS instrumentation, it was necessary to design and build a significant amount of custom hardware and software to perform the MS experiments described here. This chapter discusses the design and development of a custom mass spectrometry instrument capable of operating at high buffer gas pressures. Further specialized instrumentation developed for a specific experiment will be discussed later in the context of those experimental results for clarity.

2.2 Instrument configuration

A complete diagram of the typical MS instrument configuration is shown in Figure 2.1. The EI source, CIT, and electron multiplier are mounted inside a vacuum chamber and connected to electrical feedthroughs. The differential vacuum chamber was used to perform high-pressure experiments with the electron multiplier. A brief description of a typical experiment begins by passing electrons through the CIT to ionize analyte molecules inside the trap. The ions are trapped inside the CIT for a few milliseconds until they collisionally cool toward the center of the trap. The RF amplitude is then linearly increased to sequentially destabilize the ions and eject them toward the detector.

Instrument software written in LabVIEW (National Instruments, Austin, TX) was used to synthesize control waveforms using an analog voltage output card (PXI-6733, National Instruments). Two pulse waveforms were connected to the HV pulsing power supply to control the timing of ionization and detection. Two benchtop DC power supplies were used to provide the heating current and bias voltage necessary for driving the hot cathode EI source. A third pulse waveform was used to gate the axial RF signal from an arbitrary function generator (AFG3022, Tektronix, Beaverton, OR) to perform resonance ejection during the mass scan. This low voltage axial RF was applied directly to one CIT endcap. A fourth analog output waveform was connected to an RF signal generator (HP 8648A, Hewlett Packard, Palo Alto, CA or E4428C, Agilent, Santa Clara, CA) to produce an amplitude modulated RF signal. This low voltage RF signal was passed through an RF preamplifier and power amplifier to generate the required HV RF signal applied to the ring electrode. Output from the electron multiplier was connected to a current preamplifier and finally to a 16 bit analog voltage input card (PXI-6122, National Instruments, Austin, TX) for digitization.

The timing diagram used for a representative MS experiment is shown in Figure 2.2. Initially 0 V is applied to the gate electrode to pass electrons through during the ionization period. The drive RF amplitude is held at a fixed voltage to trap ions generated inside the CIT. At the end of the ionization period the gate electrode voltage is driven to -150 V to block the electron beam and stop ionization. The drive RF amplitude is then held constant for 5 ms to collisionally cool trapped ions towards the center of the trap. The electron multiplier is activated by driving it to -1600 V a few ms before the mass scan to stabilize the applied voltage for a constant gain. The drive RF amplitude is

then linearly ramped to perform a mass instability scan and eject ions toward the detector in order of increasing *m/z*. The axial RF signal is simultaneously gated on to perform resonance ejection during the mass scan for improved resolution and mass range. Data is acquired during the mass instability scan and converted to a *m/z* axis using custom LabVIEW software to produce a mass spectrum. Finally the drive RF amplitude is dropped to a low voltage to clear any remaining ions from the trap and prepare for the next scan.

2.3 Vacuum chamber designs

Vacuum chambers were designed to accommodate the experiments required to explore MS at high pressures. Two chamber designs were developed to perform the MS experiments described here. An isobaric chamber was designed for low-pressure MS and high-pressure MS using a pressure tolerant detector. A differentially pumped chamber was designed for high-pressure MS using a conventional electron multiplier detector which required a low-pressure region for safe detector operation.

2.3.1 Isobaric chamber

The first vacuum chamber was an isobaric design where the components under vacuum operated at an equilibrated pressure. This chamber was built using a standard 6" conflat (CF) cube (Figure 2.3) and a variety of flanges for vacuum pumps, gauges, gas inlets, electrical feedthroughs, and viewports. A custom electrical feedthrough flange (Accu-Glass, Valencia, CA) with 18 isolated coaxial connections provided electrical connectivity into the vacuum chamber (Figure 2.4). A dry scroll roughing pump and turbo pump were used to achieve the desired pressures inside the chamber (SH110 / Turbo-V 70D, Varian, Palo Alto, CA). A manual gate valve between the chamber and

turbo pump was used to decrease vacuum conductance for performing high-pressure experiments. The mounting system employed inside the chamber consisted of two parallel 1/4”-20 threaded rods protruding from the electrical feedthrough flange. All components of the MS under vacuum were secured to these rods using custom mounting fixtures and jam nuts. Independent positioning and alignment of instrument components inside the chamber was simple and straightforward with this design. Modifications to components under vacuum were performed by removing the electrical feedthrough flange from the cube and extracting the MS components for servicing on the benchtop. This design is capable of performing MS experiments up to the pressure tolerance of the particular detector in use.

2.3.2 Differentially pumped chamber

The second vacuum chamber design was a differentially pumped system with a high-pressure region for the ionization source and cylindrical ion trap (CIT) and a second low-pressure region for safe electron multiplier operation (Figure 2.5). Separate turbo pumping systems (TPS Bench / TPS Compact, Varian, Palo Alto, CA) and conductance limiting valves independently controlled the pressure in each chamber (Figure 2.6). This differentially pumped design was custom built for exploring MS performance at ≈1 torr pressures using a standard electron multiplier detector. A key aspect of this design is the use of the exit endcap electrode of the CIT to create a seal against the chamber wall and function as a flow-restricting orifice (Figure 2.7). This is what effectively separates the two regions and creates the differential pressure during an experiment. Each chamber has three 1.33” CF flange ports for vacuum pumps, gauges, gas inlets, and electrical connections. An optional port expander manifold was created to increase the original

three vacuum ports to a total of seven on each chamber so more functionality can be added as required. The chamber covers utilized o-rings and polished grooves to achieve a vacuum seal against the chamber wall. Multi-pin (9C-133, Accu-Glass, Valencia, CA) and SMA coaxial (IFDCF012012, Kurt J. Lesker, Clairton, PA) electrical feedthroughs were used to connect low and high frequency signals to the vacuum chamber components, respectively. A photo of the assembled chamber with several connections to the port expander manifold is shown in Figure 2.8. The positioning and alignment scheme in this chamber utilized a precision rail system where components were designed with a common mounting section for connecting to the rail. This made possible very precise positioning and alignment of components inside the chamber. With this mounting system, select components can be removed or replaced without disturbing other components therefore simplifying system integration. Modifications to the instrument were typically performed in place by removing the rectangular chamber cover exposing the internal components and connections. It is also possible to easily remove the entire rail with all components still attached for performing modifications on the benchtop. This chamber design is more flexible than the isobaric chamber and can perform both low and high-pressure MS experiments by maintaining pressures below 1 mTorr in the detection chamber.

2.4 Ionization source

An electron ionization (EI) source was chosen for experimental simplicity and the availability of standard EI spectral libraries. Commercially available thermionic emitters were used as electron sources for all MS experiments presented here (Figure 2.9). Although designed for operation in high vacuum, these emitters will operate at high

pressure in an inert atmosphere without burning out, much like an incandescent light bulb. Initial MS experiments were performed using a simple tungsten wire filament (ES-020, Kimball Physics, Wilton, NH) (Figure 2.9a) but the relatively large emission area of a yttria-coated iridium disk emitter (ES-525, Kimball Physics, Wilton, NH) (Figure 2.9b) provided a higher emission current over a wider area for more efficient ionization in CIT arrays. The yttria coated disk emitters can also tolerate higher partial pressures of oxygen without degradation. A pair of benchtop DC power supplies provided the heating current and bias voltage to drive the emitter. Floating the emitter to -70 V provides the 70 eV electron energy typically used for EI experiments. A custom mount secured the ceramic base of the emitter to the mounting system inside each chamber (Figure 2.10). A gate electrode with a small hole in the center was placed between the emitter and the CIT to selectively block electron current from the emitter and stop further ionization. During the ionization time the gate electrode is grounded thus allowing electrons to pass and perform EI inside the trap. When a negative voltage (i.e. -150 V) is applied to the gate electrode, electrons are blocked and the EI source is effectively turned off. This strategy enables EI source activation and deactivation on μs time scales without disturbing the relatively slow thermal equilibrium of the thermionic emitter. A complete EI assembly installed on a rail is shown in Figure 2.11.

2.5 CIT

A CIT consists of a stack of three planar electrodes with an endcap electrode on either side of a relatively large diameter ring electrode.[1] These CIT electrodes were fabricated using brass, copper, or beryllium copper sheet metal stock. Two different fabrication methods were employed with each resulting in trap electrodes with slightly

different performance characteristics. The simplest fabrication strategy is to conventionally machine the electrodes using a computer numerical control (CNC) mill. With this approach a computer-aided design (CAD) model of the electrode is interpreted by a computer that machines the electrodes from a piece of brass sheet metal using a three axis mill. Brass was chosen because it is easy to machine with a CNC but hard enough to make accurate features. This fabrication strategy produces electrodes with nearly cylindrical hole profiles as shown in Figure 2.12. The machined CITs used for this work were fabricated on a MicroMill DSLS3000 CNC mill (MicroProto Systems, Chandler, AZ). The machining process creates imperfections around the edge of the hole but these should not cause issues with trap operation because they don't protrude into the trap. Advantages of this approach include rapid turnaround time for prototyping new electrode designs and a very low cost for small numbers of parts. CITs made from conventionally machined electrodes were more difficult to correctly align due to feature placement accuracy but produced the highest resolution spectra when a properly functioning trap was built.

Photolithography followed by a wet chemical etch was also used to create electrodes. This slightly more complex fabrication strategy uses a CAD model of the electrodes to produce a photolithographic mask. The stock copper or beryllium copper sheet metal is covered with a light sensitive photoresist coating and exposed by passing light through the mask to directly write electrode features into the photoresist. Subsequent chemical development steps remove exposed areas of the photoresist and the entire sheet is then placed into a wet chemical etching solution. Only exposed areas of metal are removed by the etching process. Wet chemically etched CIT electrodes in this

work were purchased from Towne Technologies, Somerville, NJ. Since the etching process is isotropic, it is necessary to etch from both sides of the sheet metal to keep the ring electrode profiles symmetric and uniform. This method does not produce CIT electrodes with perfectly cylindrical sidewalls. A small cusp feature is visible around the center of the ring electrode as a result of the two-sided isotropic etching process (Figure 2.13). The endcap electrodes were etched from a single side to produce bowl shaped features with cylindrical openings (Figure 2.14). The flat side of the endcap electrode faces the center of the trap to correctly define the trap half-length (z_0) value and create appropriate electric fields. The bowl shaped side of the endcap doesn't contribute to the electric field inside the trap. However, it provides a funnel shaped opening where electrons or ions can pass from a larger solid angle than an equivalent cylindrical endcap hole formed by conventional machining techniques. This etched endcap profile is similar to the shape of quadrupole ion trap (QIT) endcap electrodes[2] and should result in improved signal intensity due to higher ion and electron transmission into and out of the trap. This was consistent with the observed performance of many chemically etched traps. However, the most significant advantage to this chemically etched fabrication method is the excellent positional accuracy of a photolithography based process. The electrode features could be positioned to an accuracy below 1 μm vs. the ≈25 μm accuracy of a conventional CNC mill. This is especially important with CIT arrays because optimal performance is achieved when each set of endcap and ring electrodes is accurately aligned. The experimental consequence of this improved positional accuracy in etched traps was much more consistent and reproducible behavior in terms of signal strength and resolution between different traps. Overall, both fabrication strategies have

advantages for different types of experiments and are very inexpensive with a total cost below $25 per trap. These strategies are also amenable to batch fabrication for scaling up the number of traps produced per fabrication run.

The CIT electrode design shown in Figure 2.15 contained a number of important elements, which affected the ease of use and overall trap performance. Each electrode started as a 1" diameter circle with three mounting holes for mechanically fastening the assembled trap to a mounting fixture. Excess electrode material near the perimeter was removed to decrease trap capacitance and consequently the RF amplifier load. Solder tabs protruding from the electrodes were included for convenient electrical connections to the CIT. Pin connectors were soldered to the electrode tabs so wires could be disconnected easily for trap modification or removal. Polyimide washers (McMaster-Carr, Atlanta, GA) were used as spacers beneath the mounting screws to electrically isolate each electrode and create the desired z_0 spacing value for the trap. Three 1 mm diameter holes around the perimeter were used to accurately align the stack of three CIT electrodes relative to each other using 1 mm pins (McMaster-Carr, Atlanta, GA). Three adjacent holes have concentric features of decreasing size for measuring electrode alignment under a microscope. With these alignment features, rapid screening of traps with poor electrode alignment could be completed prior to installation in the instrument and subsequent vacuum pumpdown. The active area on the CIT consists of holes in the middle of each electrode that align concentrically with the other stacked electrodes. Parallel arrays of CITs can be fabricated by simply increasing the number of holes in the electrodes. The particular arrangement of holes doesn't have much effect but the pattern needs to be identical on all three electrodes so the endcap and ring electrode holes align

concentrically when the electrodes are stacked together. Alignment of these array electrodes is performed in the same manner as aligning a single trap and doesn't add a significant amount of difficulty. For the CIT arrays used here a symmetric pattern of 19 hexagonally close-packed holes were chosen as a reasonable number of parallel CITs and since symmetric, the electrodes could be rotated 120° without affecting trap operation. CIT arrays were primarily used to maximize signal strength for experiments where a larger number of ions was beneficial.

After a CIT was constructed and secured to the mounting flange, the entire assembly was secured directly to the differential chamber wall to achieve a vacuum seal where the endcap hole limits gas conductance between the two chambers. The spacer material used to construct the trap created an open structure between electrodes to maintain equilibrium between the high-pressure chamber and the trap. Therefore the pressure inside the trap was the same as that measured in the high-pressure chamber. A CIT assembled on a differential chamber trap mounting fixture is shown in Figure 2.16 with the endcap hole visible in the center of the top electrode. An assembled 19 hole CIT array assembled on an isobaric chamber mounting fixture is shown in Figure 2.17. Both single traps and arrays could be used in either mounting fixture design.

2.6 Electron multiplier

The most commonly used detector for MS experiments is the electron multiplier (EM).[3] An EM was chosen for most experiments presented here because it is a mature and proven detector technology that requires no developmental work. The EMs used here are replacement modules (2300 or 2312, DeTech, Palmer, MA) originally designed for commercial instruments (Figure 2.18) and were easily adapted for use in these custom

MS instruments. They are both continuous dynode type EMs where the active region consists of a specially designed continuous resistive coating deposited on a glass substrate. Custom mounting fixtures were fabricated to secure these EMs and make electrical connections to the front and rear of the resistive glass surface (Figure 2.19). To activate an EM, a negative HV is applied to the front while the back side is grounded. The negative potential on the front end attracted positive ions exiting the CIT. When an ion strikes the resistive coating a plume of secondary electrons are ejected from the surface. Since the front of the EM is at a negative potential relative to the rear, the negatively charged electrons are pushed toward the rear by the electric field and strike the surface further down the tube releasing several more plumes of secondary electrons. This process repeats multiple times until the original positively charged ion that struck the front of the EM is converted into approximately 10^6 electrons at the rear. The multiplication of the original number of charge carriers made reading an EM's output easy with a commercially available current preamplifier (SR570, Stanford Research Systems, Sunnyvale, CA). Recording the detector's output current as a function of time with a 16 bit analog voltage input card (PXI-6122, National Instruments) produced the familiar mass spectrum.

This physical mechanism of electron multiplication where plumes of secondary electrons eject from the surface can cause undesired ionization of neutral gas molecules through an EI mechanism.[3] These unwanted ions are generated after mass analysis and therefore have an unknown *m/z* value that contributes to detector noise. At low pressures the density of neutral molecules is sufficiently low such that these events do not initiate uncontrolled feedback. However, at high pressures there are significantly more neutral

molecules near the EM surface and these unwanted ions create a feedback loop that saturates the detector output almost immediately.[4-5] This breakdown overwhelms any usable signal and can damage the sensitive EM surface coating and reduce the lifetime of the multiplier. Therefore the detector chamber pressure must be maintained below 1 mTorr to ensure safe EM operation.

2.7 CTIA detector

An ideal detector would be capable of operating at any pressure which would simplify the vacuum system to a single chamber and significantly reduce SWaP. Therefore, it is desirable to replace the electron multiplier with a pressure tolerant ion detector to achieve high-pressure portable MS. Faraday cup (FC) detectors are an alternative ion detector technology that utilize pressure tolerant solid-state electronics to detect charge.[6] In addition, they are independent of ion energy, stable and inexpensive. They measure positive and negative ions and operate with low voltages. FC detectors that measure charge (integrators) rely on a very small feedback capacitor to store the collected charge. The gain of these detectors is inversely proportional to the feedback capacitance, which allows for high gain without decreasing the time response of the detector. An advantage of an integrating style of FC detector is a lower detector read noise and LOD resulting from the inherently superior noise characteristics of a capacitor. An example of this charge detector design is the capacitive transimpedance amplifier (CTIA), which integrates incoming ion current on a feedback capacitor and produces a proportional output voltage. This detector technology has been described in detail previously.[6] CTIA technology has high sensitivity and low noise due to the ability to microfabricate extremely small fF range capacitors directly on silicon.[7] This makes

direct electronic detection of ions via charge integration feasible. Although alternate detector technologies exist, there are relatively few options for pressure tolerant detectors with sufficient gain and time response to detect small numbers of ions arriving on μs time scales from an ion trap.

The work presented here uses a second-generation, single-channel CTIA designed by a collaborator (M. Bonner Denton, UA, Tuscon, AZ) as a pressure tolerant ion detector for an isobaric microscale CIT instrument.[7] A complete diagram of this instrument is shown in Figure 2.20. Most of this instrument operates in the same fashion as the differential chamber instrument with the electron multiplier except for some electronics related to the detector. The CTIA is fully differential with two inputs to reject input noise and two outputs which reject common mode noise by subtracting the outputs to generate the final signal. The detector consists of a custom integrated circuit (IC) and copper Faraday cup electrode mounted on a 1.5 x 2" circuit board (Figure 2.21). The custom IC includes four independent CTIA amplifiers with differential inputs and outputs for common mode noise rejection. Each CTIA amplifier includes independent gain control implemented with two built-in feedback capacitors to accommodate a larger range of signal intensities. A 10 fF feedback capacitor is used for high gain and a second 990 fF capacitor is connected in parallel for a total capacitance of 1000 fF in low gain mode. This represents two orders of magnitude in signal intensity between high and low gain mode. The detector operates by collecting incoming charges at the Faraday cup electrode and storing them on the feedback capacitor. This results in an integrating style detector where the output voltage is proportional to the number of collected charges and inversely proportional to the feedback capacitance. Common mode noise is picked up by

a second reference input and the CTIA differentially amplifies the input signal and produces two identical but inverted outputs. The differential output can further reduce noise picked up after the amplifier and double the resulting signal intensity by subtracting the outputs before digitization.

A 12 V DC supply was used to power the detector and a second -125 V DC supply provided the detector bias voltage to attract low energy ions exiting the CIT. A custom designed aluminum enclosure was used to shield the CTIA's sensitive amplifier circuitry from RF interference. An isolated wire mesh grid was placed over an opening in the shield box and a 1 μF high voltage ceramic shunt capacitor was connected between the grid and the grounded shield box. This isolated grid configuration can be biased along with the CTIA detector while still providing a low impedance path to ground for RF interference.

Since the detector circuitry was biased to attract charged particles, a few special considerations had to be taken for safely interfacing to the floating detector. To reset the detector it was necessary to bias the TTL reset pulse using a custom digital pulse isolator circuit based on the H11N1 logic optocoupler (Figure 2.22). This circuit converted a ground referenced pulse to a bias referenced pulse for resetting the detector. To safely connect the detector output to a ground referenced analog input channel it was also necessary to remove the bias voltage from both differential outputs. This was achieved with a custom high-voltage subtraction circuit based on the AD629 HV difference amplifier. This circuit simultaneously removed the bias and combined the differential outputs by subtracting both signals. The 500 kHz bandwidth of this subtraction circuit ensures the time response of the detector won't be degraded by the isolation circuitry.

The resulting ground referenced output was then connected to a 16 bit analog voltage input card (PXI-6122, National Instruments) for digitization. Due to the integrating functionality of the CTIA it was then necessary to perform a numerical derivative in software to produce the recorded mass spectrum.

2.8 Electronics

Custom circuitry was designed and built to produce appropriate voltages for driving various instrument components. The circuits described here were critical to performing most MS experiments and were used extensively in the lab.

2.8.1 RF amplifiers

A HV RF signal needs to be applied directly to the CIT ring electrode to produce appropriate quadrupolar electric fields for trapping ions.[8] This RF signal is initially created by an RF generator at low voltage. The signal is then passed into a RF preamplifier circuit based on the Linear Technology LT1206 current feedback amplifier. This circuit amplifies a low power input waveform to an appropriate power level for driving the input of a larger power amplifier.

A first generation RF power amplifier was built by the UNC electronics facility using a modified Motorola EB63A 140 W communications amplifier kit (Communications Concepts, Beavercreek, OH). The amplifier was powered by a 12 V DC switching power supply and featured an air core roller inductor for resonating the capacitive CIT connected to the output to maximize the applied voltage. This roller inductor design tunes the amplifier to a new frequency or capacitive load on the fly by turning a knob. An oscilloscope monitored and measured the RF signal during MS experiments (TDS3034B, Tektronix, Beaverton, OR). This amplifier design is capable of

generating 500 $V_{0\text{-}p}$ RF waveforms at ≈6 MHz with ≈2 ppth amplitude stability as measured by a real-time spectrum analyzer (FSVR7, Rohde & Schwarz, Columbia, MD).

A second generation RF power amplifier was built with the help of the UNC electronics facility using a modified Motorola AN762 140 W communications amplifier kit (Communications Concepts). A number of modifications were performed to improve the RF amplitude stability including input power bypass capacitors, power supply filters, and a custom double-regulated 12 V DC power supply. This power supply used a large bank of capacitors and two stages of voltage regulation to produce a very stable 12 V DC output at several amps of current. The tunable roller inductor was replaced with a fixed tap inductor to improve the electrical connection and therefore improve amplitude stability. This amplifier is capable of generating 500 $V_{0\text{-}p}$ RF waveforms at ≈6 MHz with <1 ppth amplitude stability.

2.8.2 HV pulsing power supply

A circuit to generate the HV pulses for driving the ionization gate electrode and EM detector was designed using the EMCO F series miniature HV DC power supplies (Figure 2.23). This circuit is controlled by two 5 V input pulses and generates variable output pulses up to -200 V and -2 kV for the gate electrode and EM, respectively. A variable voltage regulator powers each HV supply to generate a proportional HV DC voltage. A solid-state relay (SSR) is used to switch the gate electrode voltage between ground and -200 V for controlling ionization. A custom HV single pole double throw (SPDT) switch was constructed using two Voltage Multipliers OC100HG optocouplers. Activating an optocoupler electrically connects the two sides together so it can be used as a HV switching element. Alternately activating the two optocouplers switches the output

between ground and -2 kV in ≈2 ms. Since the EM is only activated for the mass scan, a fast switching time is highly desirable to avoid limiting the type of experiments that can be performed due to a long detector turn-on delay. An inverter is used on one of the optocoupler inputs to prevent both switching elements from activating simultaneously and shorting the HV power supply.

2.9 Instrument control

In the early stages of development for this project all of the timing, control, and data acquisition functionality of the instrument were performed with separate benchtop devices like pulse delay generators, arbitrary function generators, and oscilloscopes. Although this method was functional, it was slow, cumbersome, and prone to mistakes because a simple modification to the experimental design required changes in multiple locations. It was also necessary to meticulously record all experimental parameters by hand for any saved data, which was also prone to oversights and mistakes. Therefore it was highly desirable to combine as much functionality as possible into an integrated instrument control system to automate the instrument and enable users to rapidly perform a variety of MS experiments.

An integrated control system was developed based on a PXI chassis with analog input and output cards from National Instruments. The LabVIEW programming environment was chosen because the excellent hardware integration and high level programming style are made for rapid software development. Using this foundation, a suite of software was written in LabVIEW to integrate the tasks of previously separate benchtop control devices and provide a much more efficient and user-friendly interface to the custom MS instruments. A modular design was chosen for this control software to

make the code easy to understand, reuse, or modify. It was designed to be very flexible so the same program could be distributed to several MS instruments to perform a variety of experiments without needing to maintain specialized software on each system.

To begin an experiment, the user opens the main graphical user interface (GUI) program which incorporates most instrument functionality (Figure 2.24). This program controls waveform generation and timing, data acquisition, and viewing of previously saved data files. Since the operation of this program is dependent on user interaction, an event-driven methodology was chosen so the software would only respond to specific events instead of forcing it to constantly check the input parameters. By taking advantage of the events that are generated when a user interacts with a LabVIEW GUI, it was possible to configure the program to restart waveform generation only when a change was made to a control. When no events are being generated the software continuously writes the desired waveforms without further interaction or data transfer between the computer and analog output card.

A diagram illustrating the hierarchy of various modules of the control software is shown in Figure 2.25. All user interaction with the software is handled by the main GUI control program (Control_Experiment.vi). The three major functions performed by this software can be operated independently or simultaneously to give the user more flexibility for performing different experiments. Global variables were used to communicate between modules when necessary.

When the user starts the waveform generation module (Write_Experiment_Waveforms.vi), experimental parameters feed into separate programs for creating a pulse waveform (Create_Pulse.vi) and a linear ramp waveform

(Create_Ramp.vi) to generate the correct timing and amplitude of the instrument control signals. Another program is used to convert this waveform data inside the computer to the corresponding real voltages (Write_Waveforms.vi) by writing this waveform data to the analog outputs. This program calculates the experimental control waveforms once and then continuously writes them to the analog outputs until the user changes one of the input parameters or stops waveform generation. This is much more efficient than writing a set of waveforms once since there is a significant amount of overhead involved with calculating new waveforms and transferring that data to the analog output cards continuously.

When the user starts the data acquisition (DAQ) module, the analog voltage input program (Analog_In.vi) records two channels of analog voltage waveforms. When activated this program takes the DAQ input parameters and acquires the requested number of spectra. The output of this module is two digitized waveforms representing the averaged signals present on the two analog input channels. If the user chooses to save the resulting data it is passed to a data saving program (Save.vi) along with a list of all computer controlled experimental parameters converted to a string (Parameters_to_String.vi). This information is combined and saved as a text file (Write_Data.vi) along with an image of the data as displayed on the screen for quickly browsing through data files (Write_Image.vi).

A final module quickly reads saved data files (Read_Data.vi) and displays the data on a graph. The text file header information is parsed from a large string back into individual experimental parameter variables (String_to_Parameters.vi) for making programmatic decisions based on these parameters.

2.10 Post-processing software

Several LabVIEW programs were written to perform post-processing operations on saved MS data files. A general purpose signal processing program (signal_processing.vi) can be used to apply a variety of signal processing algorithms to a MS data file for improving the signal to noise ratio (S/N) (Figure 2.26). This program was designed to be used in a standalone mode for processing single files or in an embedded mode where it can be placed inside another program. The implemented algorithms include standard low-pass filtering and boxcar averaging which are primarily used for data taken with an electron multiplier. The remaining algorithms were implemented specifically for processing data taken with the pressure tolerant Faraday cup detector. Processing this data is more challenging because the integrating style of detector requires a numerical derivative to produce the final mass spectrum. This derivation reduces the S/N significantly by effectively amplifying small signal changes due to noise in the data. The first algorithm performed a sliding window derivative which is similar to a typical point-by-point derivative except the slope is calculated using a linear regression through more than two consecutive data points. This helps to remove high frequency noise from the data by reducing the influence of a single noisy point. The multi-read average derivative algorithm combines multiple consecutive data points into a single averaged point to reduce the inherent read noise in the analog input process. A standard numerical derivative is then performed on the new data to produce a mass spectrum. This effectively reduces the sampling rate in exchange for a reduced read noise so it is important to oversample any data processed by this algorithm. Since this algorithm effectively reduces the sampling rate, a sampling rate reduction algorithm was

also implemented to compare data before and after the derivative. This algorithm simply eliminates data points to simulate the same data recorded at a lower sampling rate. The final signal processing algorithm utilized a MATLAB library named Cromwell that was developed by the University of Texas M. D. Anderson Cancer Center specifically for processing MS proteomics data.[9] This library performs a wavelet transformation on the raw data using wavelets designed specifically for signal processing applications. It effectively separates different components of the data, some of which contain primarily noise components and are removed with a threshold value before transforming the data back into its original form to produce the final filtered data. This wavelet deconvolution would be appropriate for extremely noisy data when the simpler algorithms aren't able to sufficiently improve S/N.

A batch processing program (signal_processing_batch.vi) for rapidly performing signal processing on an entire folder of data files was developed using the embedded signal processing program. Creating this batch processing program was simply a matter of looping through all MS data files in a given folder, passing the individual files to the embedded signal processing program, and saving the resulting filtered data in a separate folder. This program was able to process 100 MS data files in a few seconds.

Since the raw instrument data is recorded as a function of time a program was written (create_calibrated_mass_axis.vi) (Figure 2.27) to convert the X-axis time units to *m/z* units for generating a real mass spectrum. Using the experimental parameters saved inside each file, the program automatically extracted the portion of data corresponding to the mass scan and provided two cursors to define two known mass values in the data. By defining two mass values and assuming a linear RF amplitude ramp, the program

converted every time point to a corresponding *m/z* value using the equation of a line. Signal processing functionality was embedded inside this program to clean up data and make assignment of the two known *m/z* values more accurate. An additional feature of this program is the ability to display NIST standard spectra along with the experimental data on an *m/z* axis. These spectra are automatically generated based on an Excel file to make addition of more standard spectra easy. The user can add an arbitrary number of NIST standard spectra to the graph for comparison to the experimental data. The superimposed standards also help delineate any mass shifts as a result of incorrect peak assignment before the data is saved.

2.11 Tables and figures

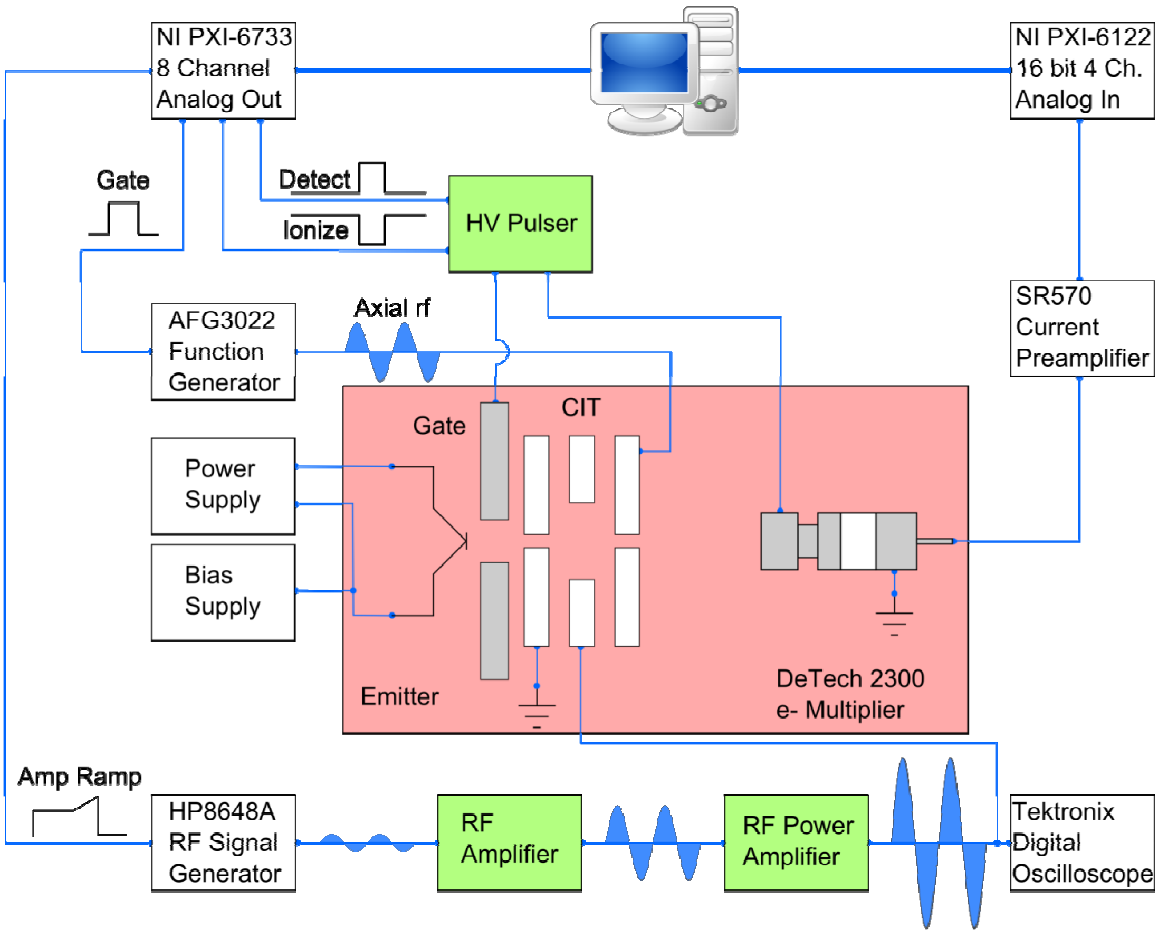

Figure 2.1: Schematic diagram of microscale CIT MS instrument with EM detector. Custom and commercially available electronics are represented in green and white, respectively. The vacuum chamber is represented in red.

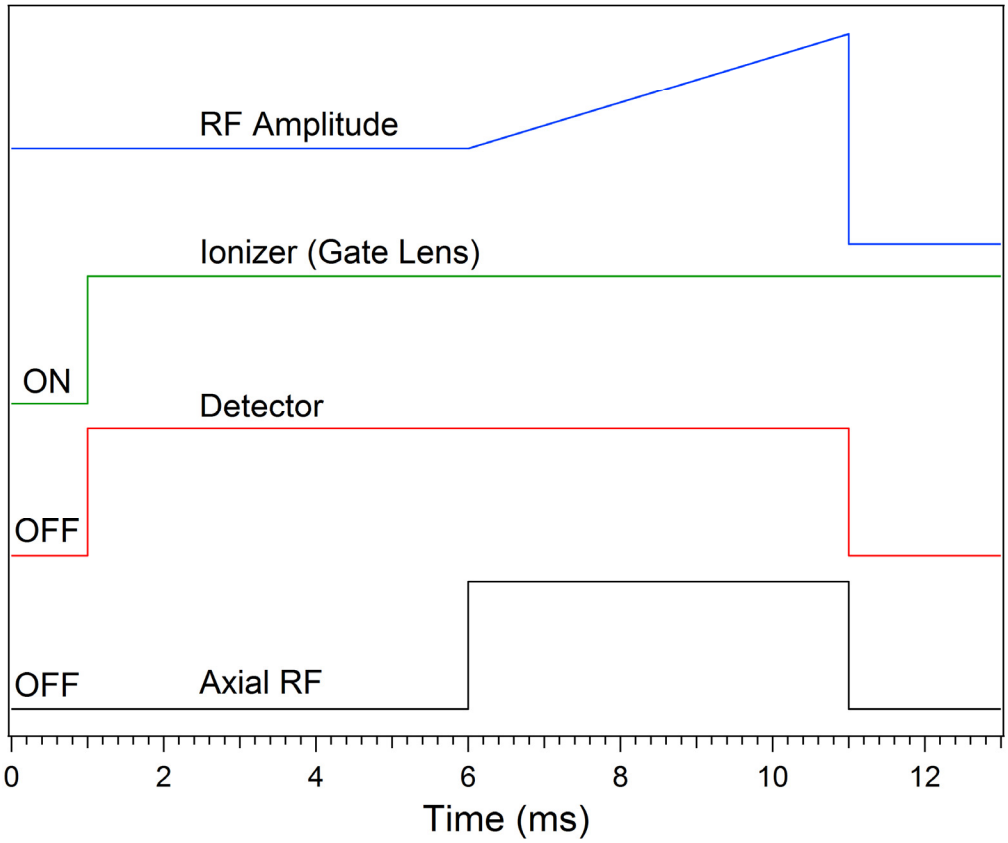

Figure 2.2: Timing diagram used for a representative MS experiment. The ramp waveform modulates the RF amplitude throughout the experiment and the three pulses control the timing of ionization, detection, and axial RF voltages applied to the instrument.

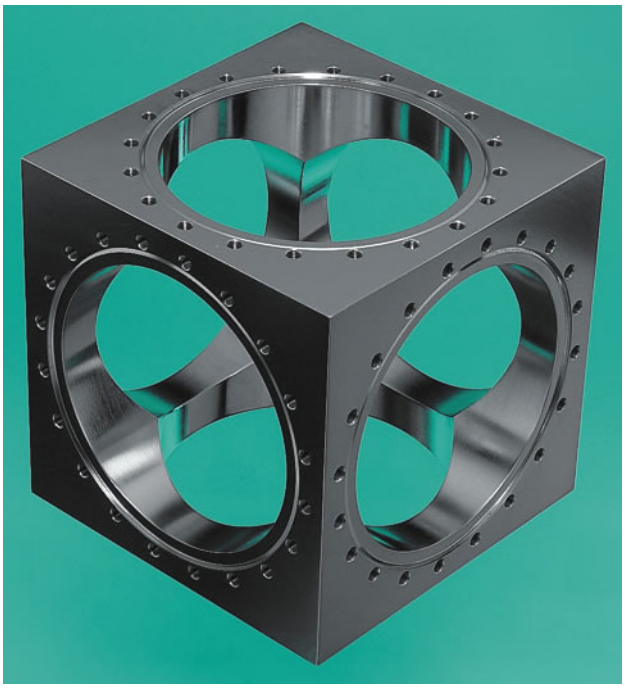

Figure 2.3: 6" CF cube used for isobaric chamber design. Connections for vacuum pumps. gauges, gas inlets, viewports and electrical feedthroughs are made by attaching flanges to the cube.

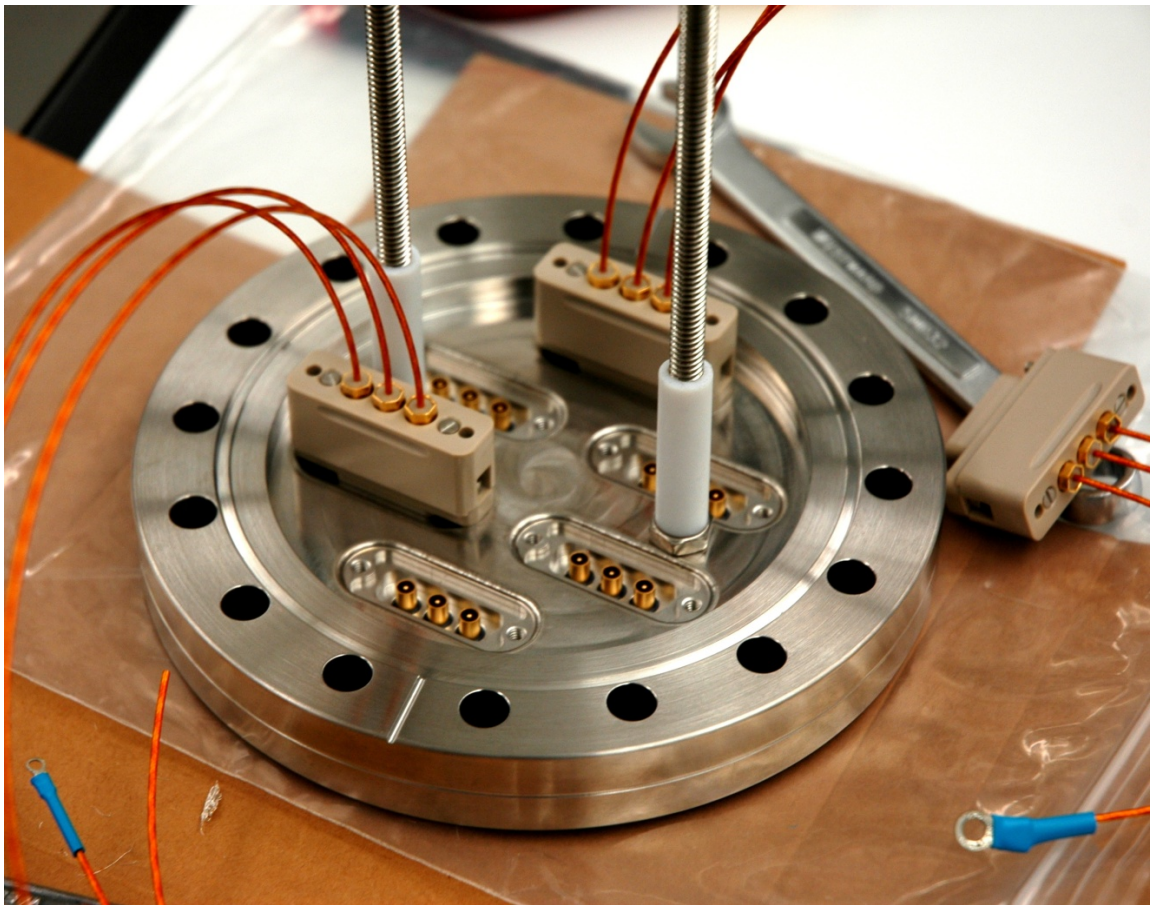

Figure 2.4: Internal view of custom 6" CF electrical feedthrough flange with 18 isolated coaxial connections and threaded rods for mounting components.

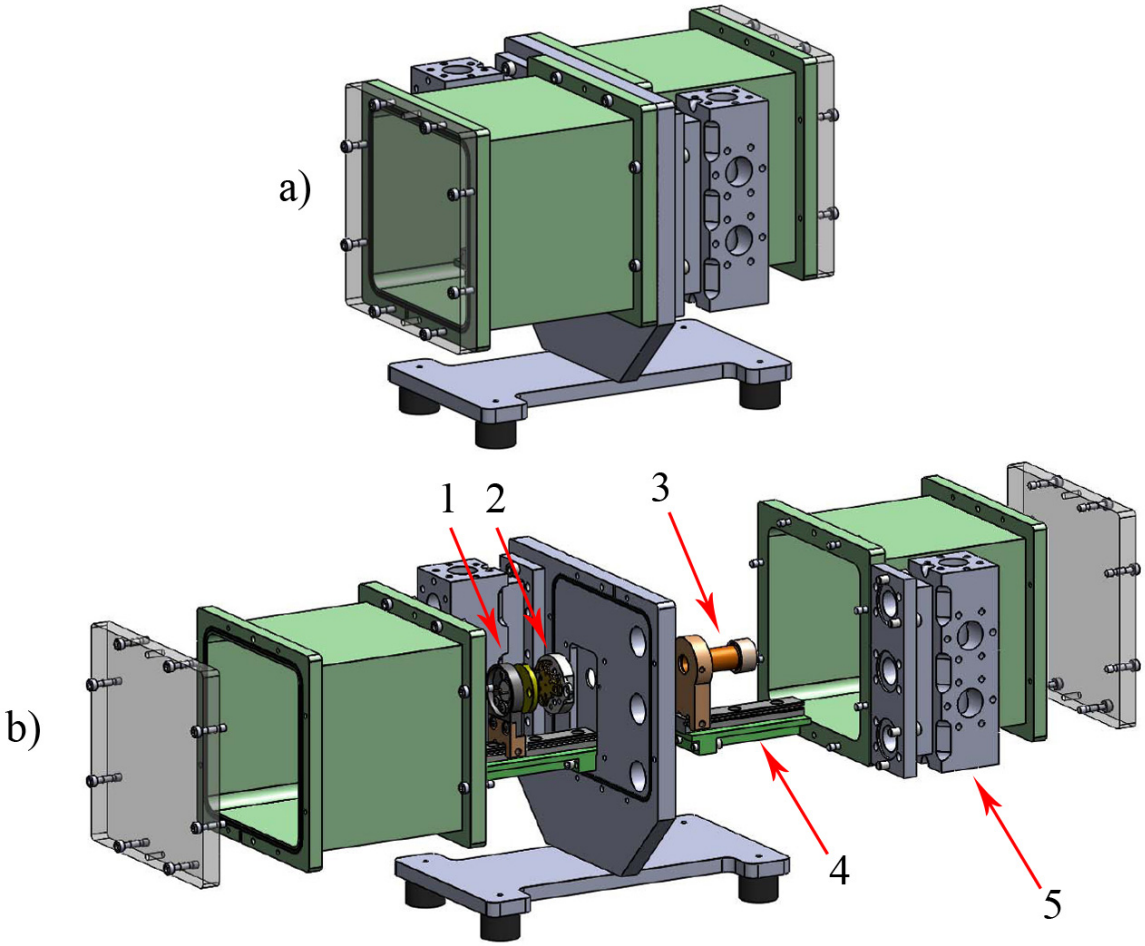

Figure 2.5: (a) Differential vacuum chamber design with high and low pressure chambers used for high-pressure MS experiments. (b) Exploded view showing internal components (1) EI source, (2) CIT, and (3) Electron multiplier mounted on a precision rail (4) for accurate alignment. The vacuum chambers have 4" inside dimensions and are easily removable for working on internal components. An optional 1.33" CF manifold block (5) was designed to accommodate up to 7 total ports on each chamber.

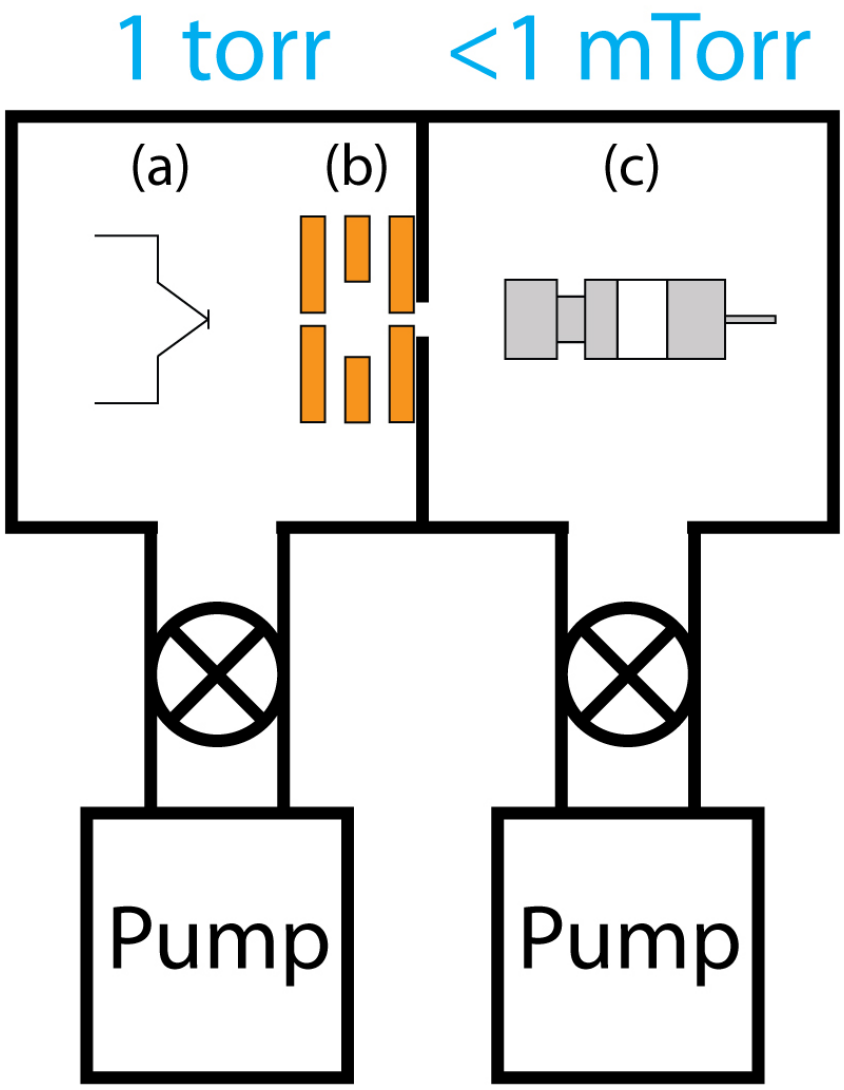

Figure 2.6: Schematic of differential vacuum chamber showing high and low pressure chambers. (a) Ionization source, (b) CIT, and (c) EM detector are pictured in their respective chambers. Separate pumping systems and conductance limiting valves controlled pressure independently in each chamber.

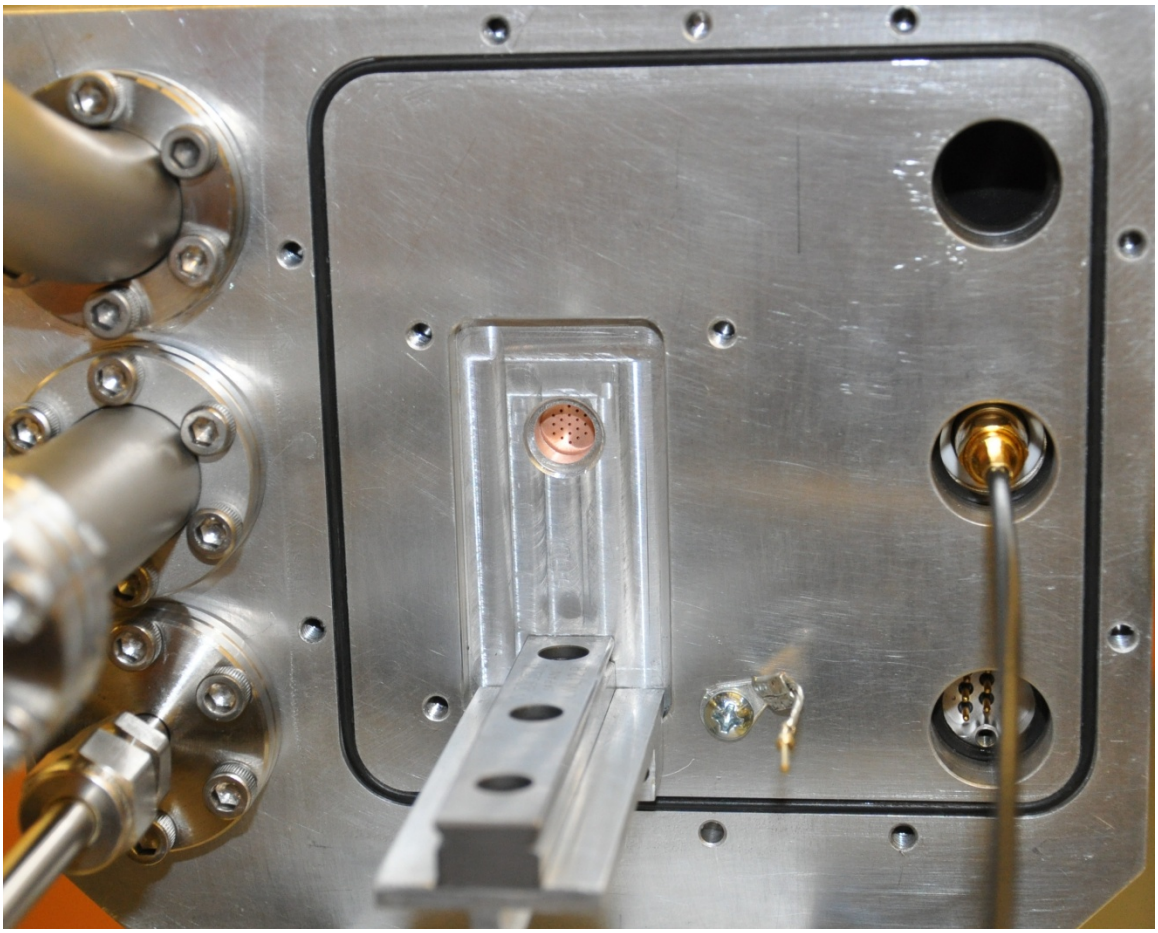

Figure 2.7: Image of endcap electrode sealed against the chamber wall as viewed from the detector chamber.

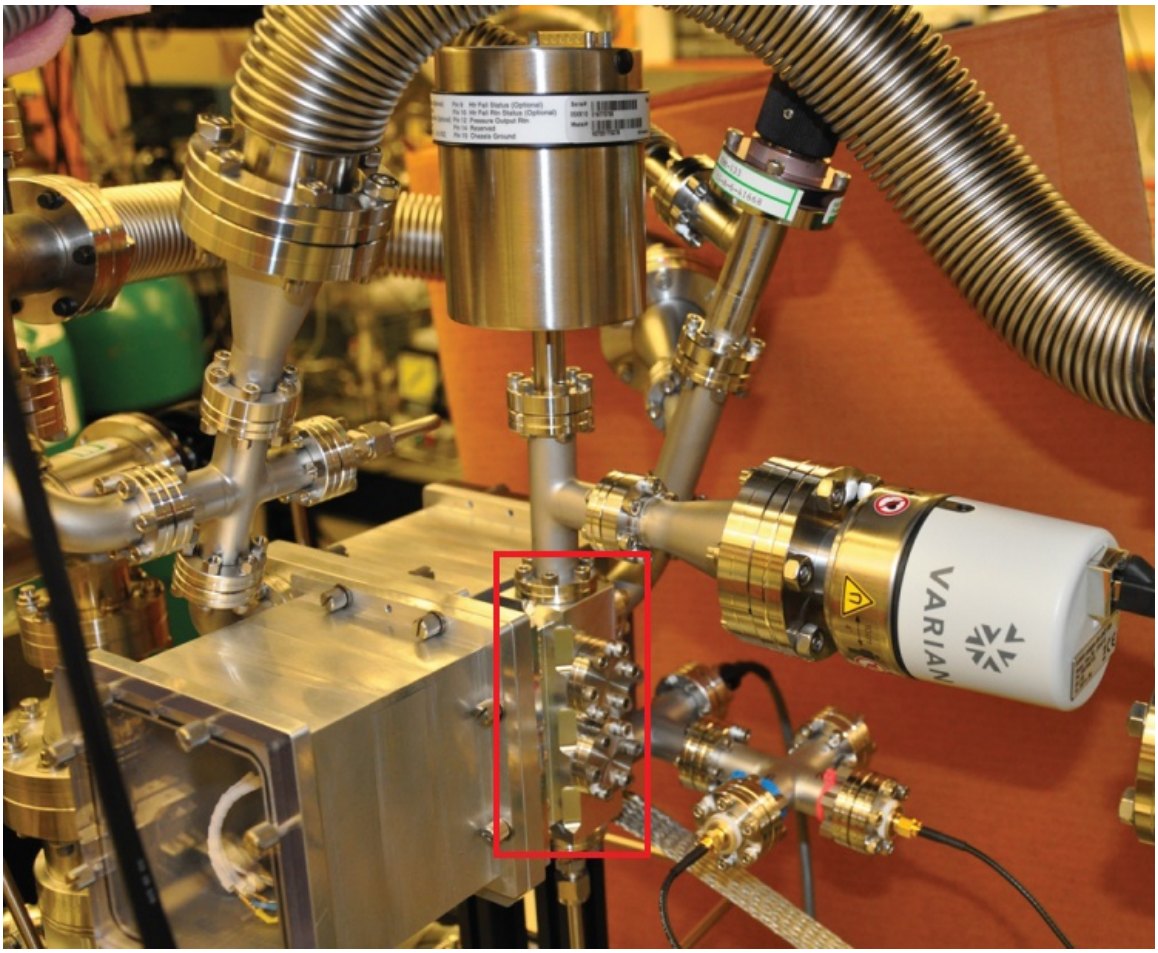

Figure 2.8: Image of assembled differential chamber instrument showing multiple vacuum connections on the 7 port manifold indicated in red.

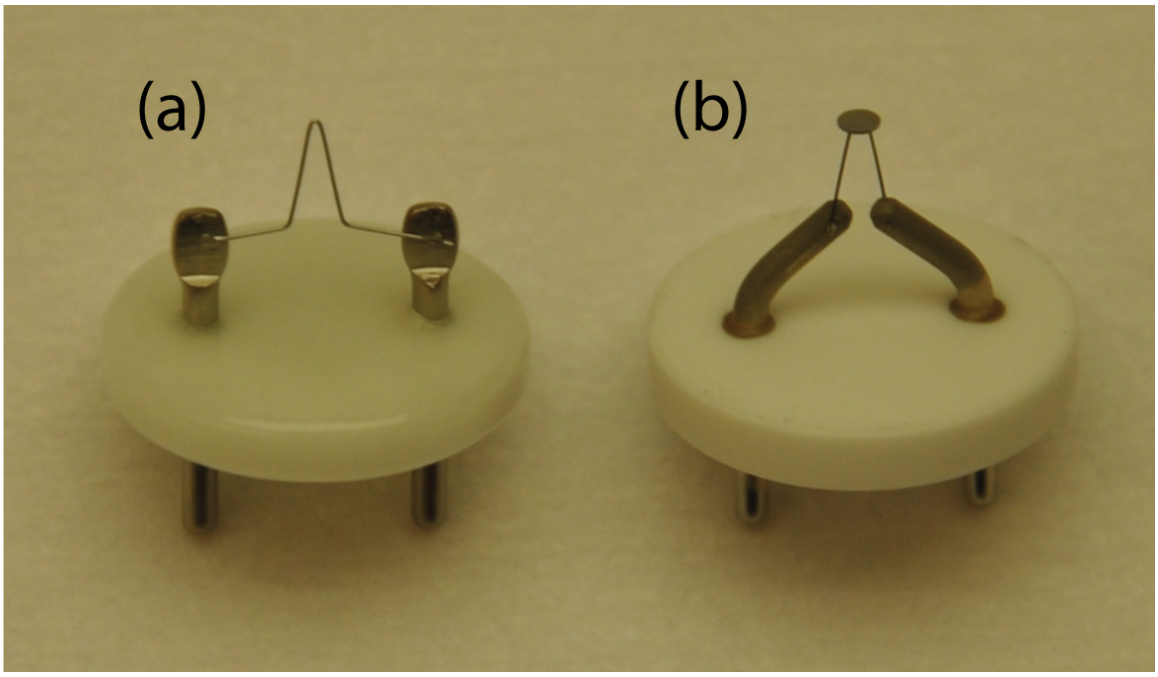

Figure 2.9: Commercially available (a) tungsten filament and (b) yttria coated iridium disk emitter EI sources. The disk emitters have a much larger emission area than the filament which results in a higher emission current and consequently a larger signal intensity.

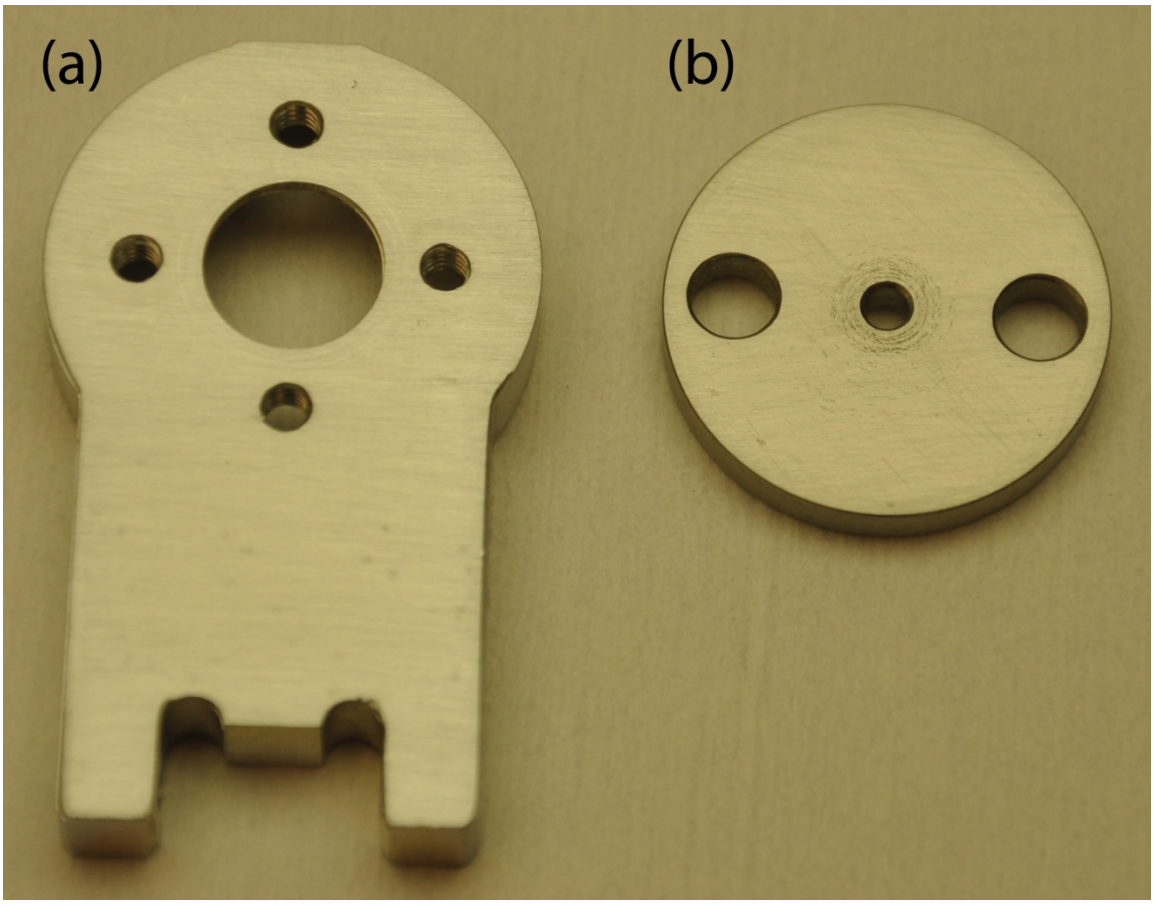

Figure 2.10: (a) Custom mounting fixture for EI sources with a standard rail mount base. (b) Ionization gate electrode with mounting holes and a hole in the center for electron passage.

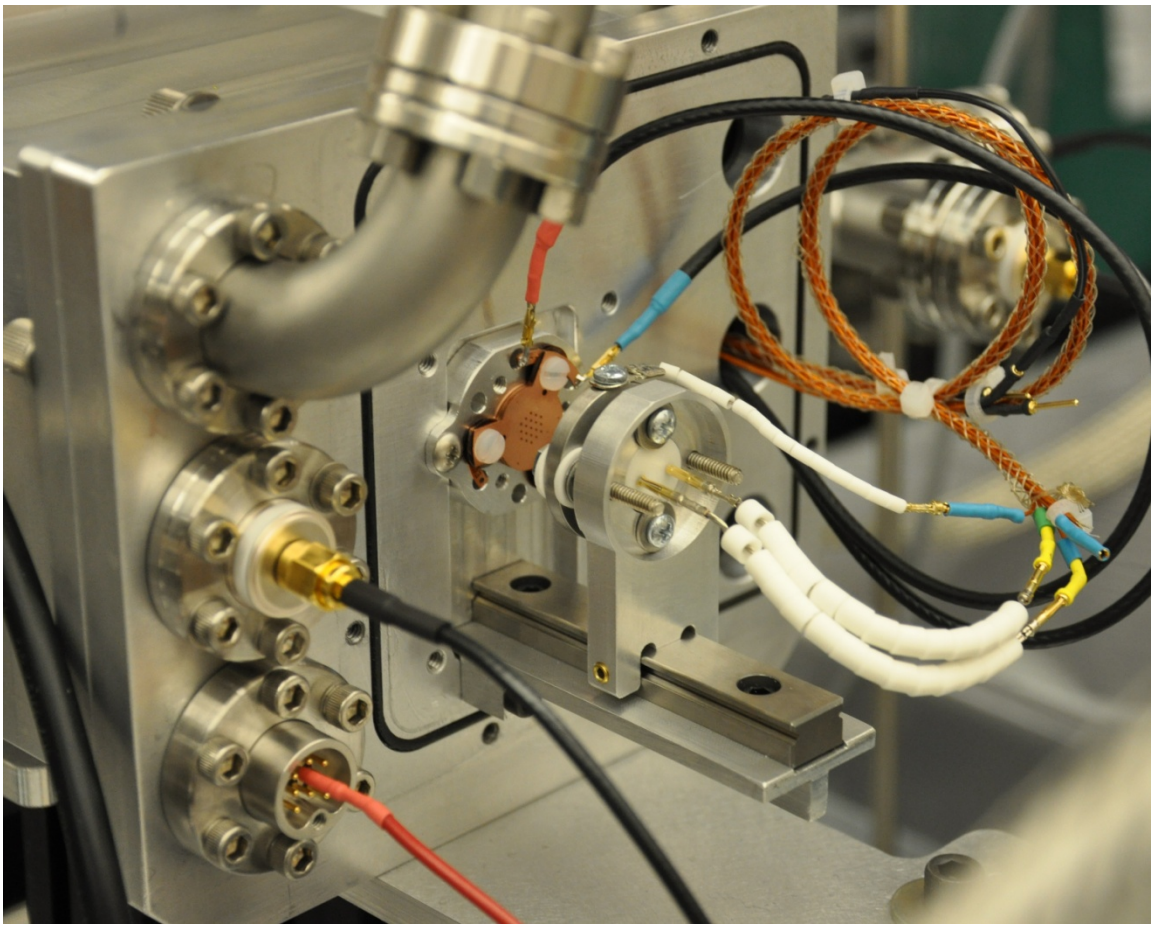

Figure 2.11: Image of the complete EI source assembly installed on the mounting rail. Two electrical connections covered with large ceramic beads provide the heating current and bias for the emitter and a third connection covered with small ceramic beads provides the voltage for controlling the gate electrode.

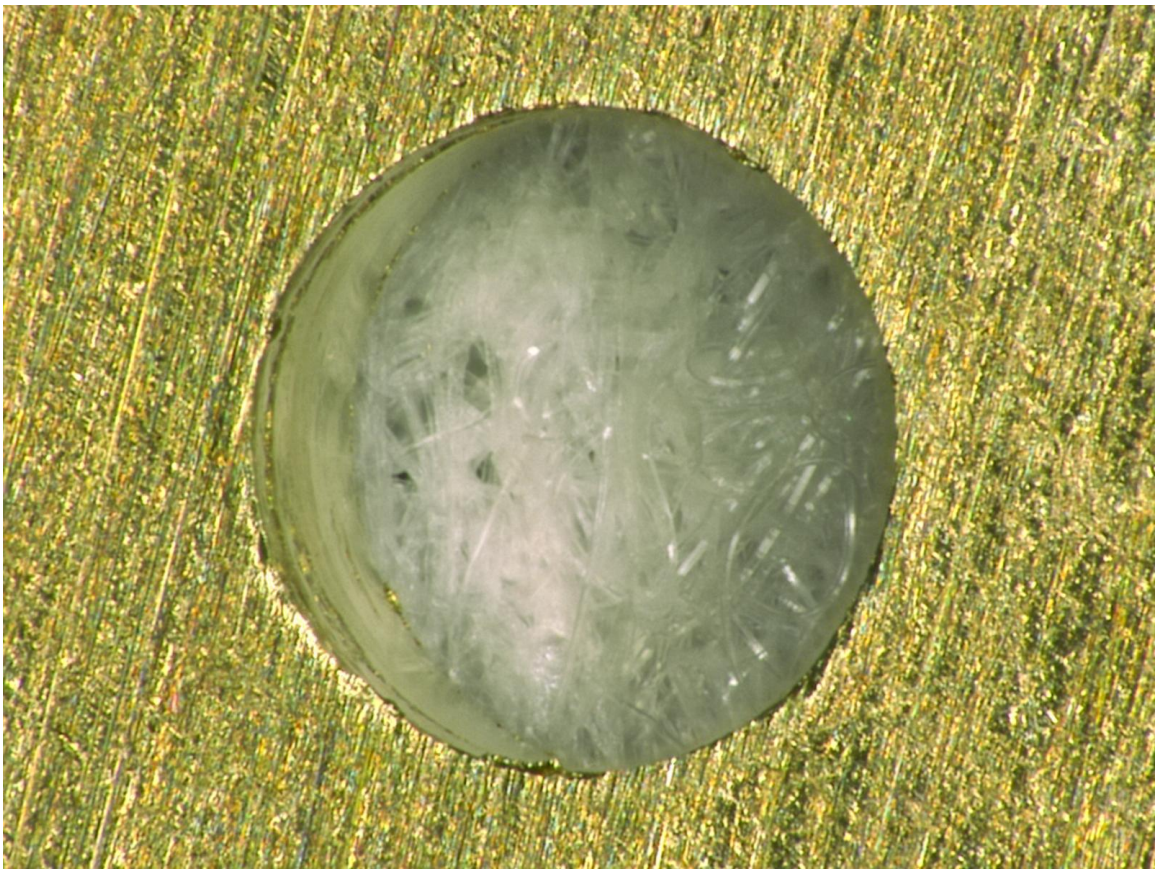

Figure 2.12: Image taken at a 15° angle of 1 mm cylindrical ring electrode hole formed by CNC machining a piece of brass sheet metal. Small burrs and imperfections from the machining process are visible around the edge of the hole.

Figure 2.13: Image taken at 30° angle of 1 mm cylindrical ring electrode hole formed by wet chemical etching a piece of copper sheet metal. The cusp feature created by the two sided isotropic chemical etching process is visible inside the hole.

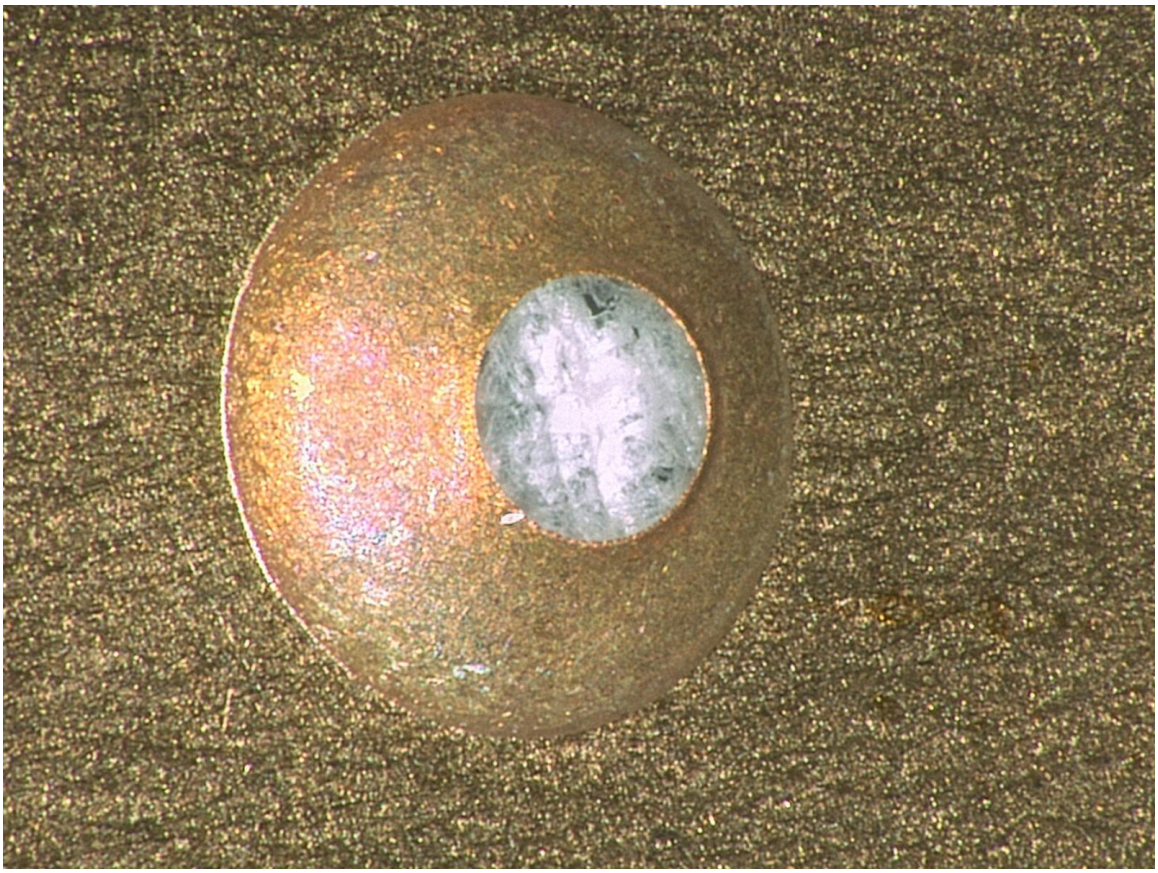

Figure 2.14: Image taken at 30° angle of 400 μm endcap electrode formed by wet chemical etching a piece of beryllium copper sheet metal. The bowl shaped feature formed by the one sided isotropic chemical etching process is visible from the outside of an assembled trap.

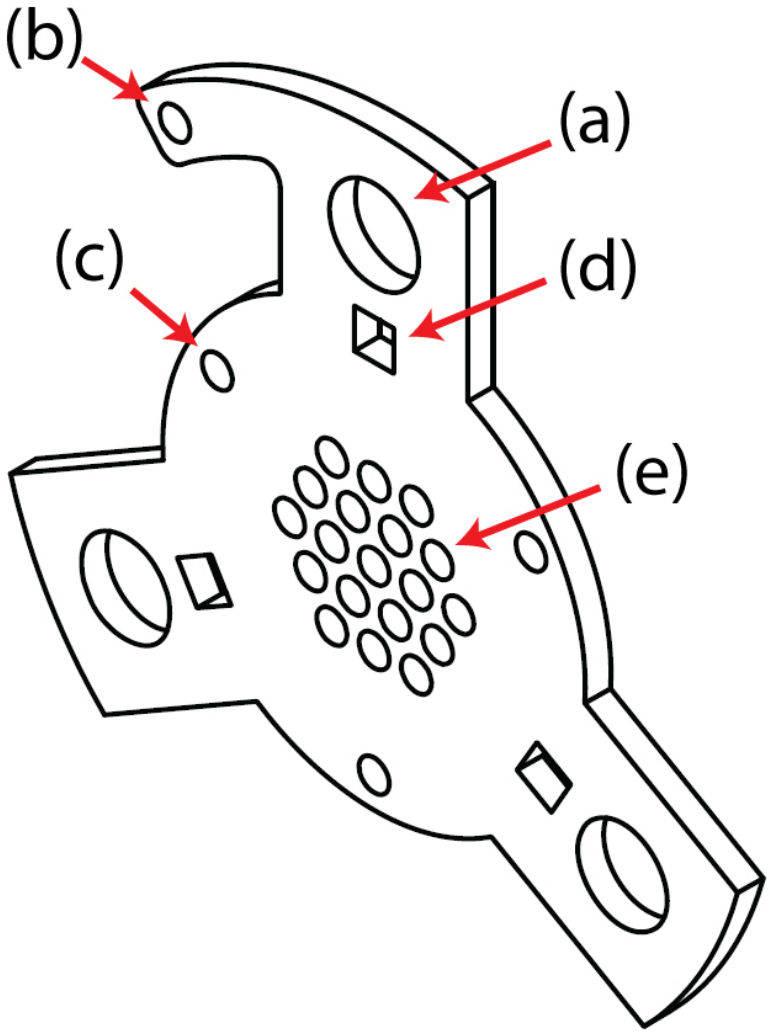

Figure 2.15: CAD drawing of a ring electrode showing (a) #4 mounting screw holes, (b) solder tab, (c) 1 mm diameter holes for alignment pins, (d) optical alignment verification features, and (e) array of CIT holes.

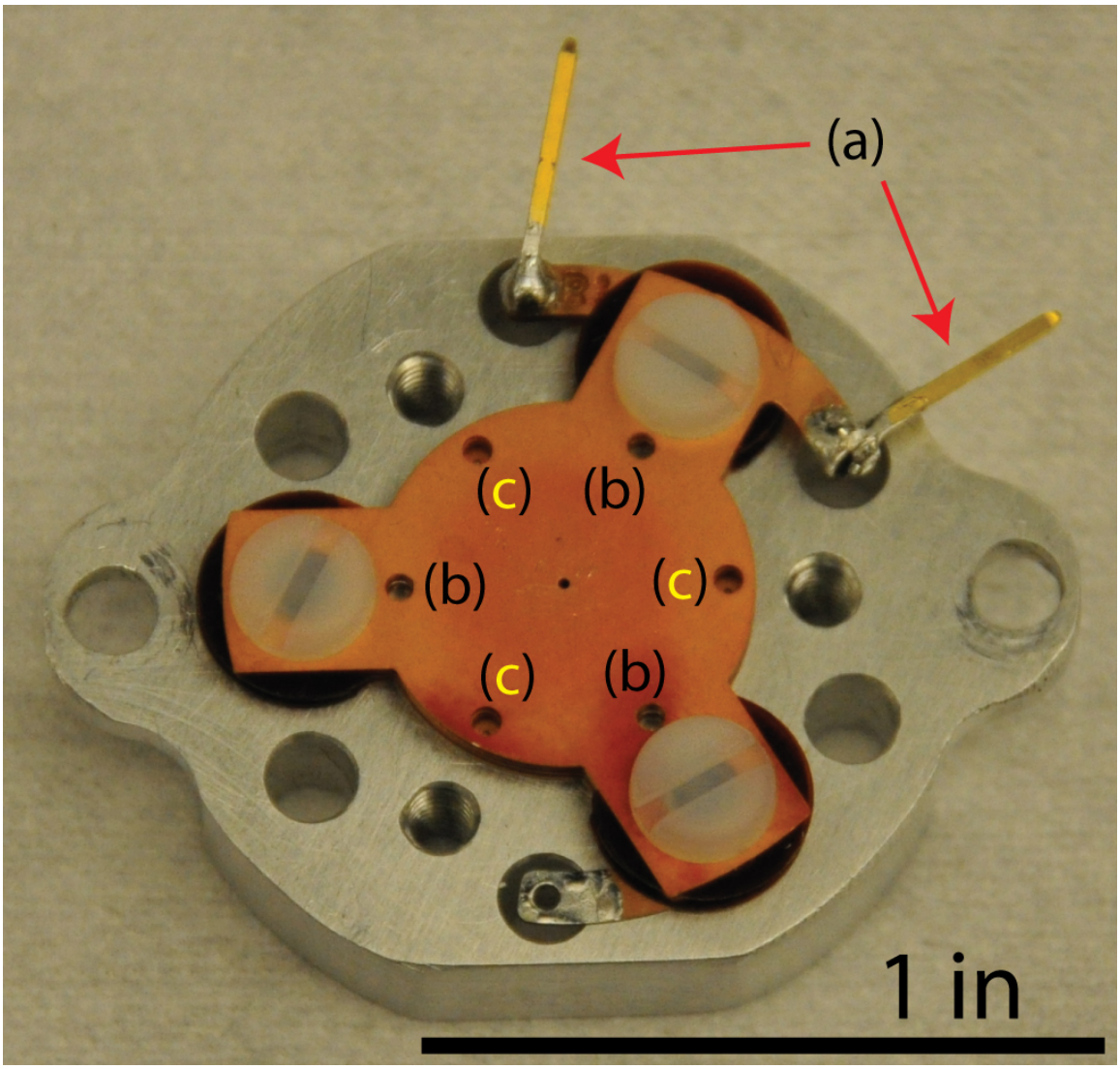

Figure 2.16: Image of single hole CIT assembled on a differential chamber trap mounting fixture. Electrical connections were made using (a) removable pin connectors. (b) Holes for alignment pins are visible near the three nylon screw heads with (c) three adjacent holes that enable optical alignment measurement. The CIT endcap hole is in the center of the electrode.

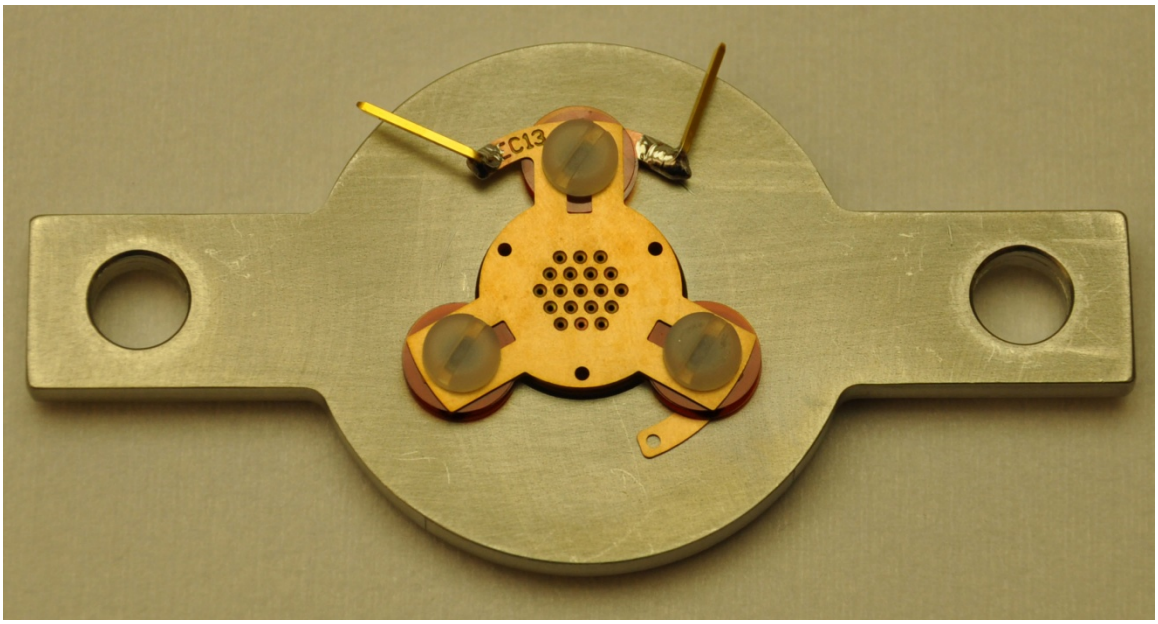

Figure 2.17: Image of 19 hole CIT array assembled on an isobaric chamber trap mounting fixture.

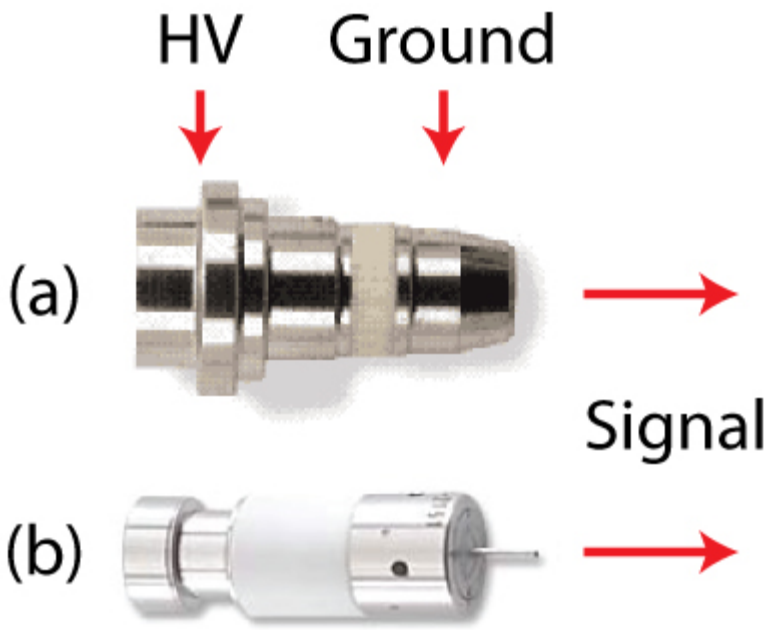

Figure 2.18: (a) DeTech 2312 and (b) DeTech 2300 EM detector modules and associated electrical connections.

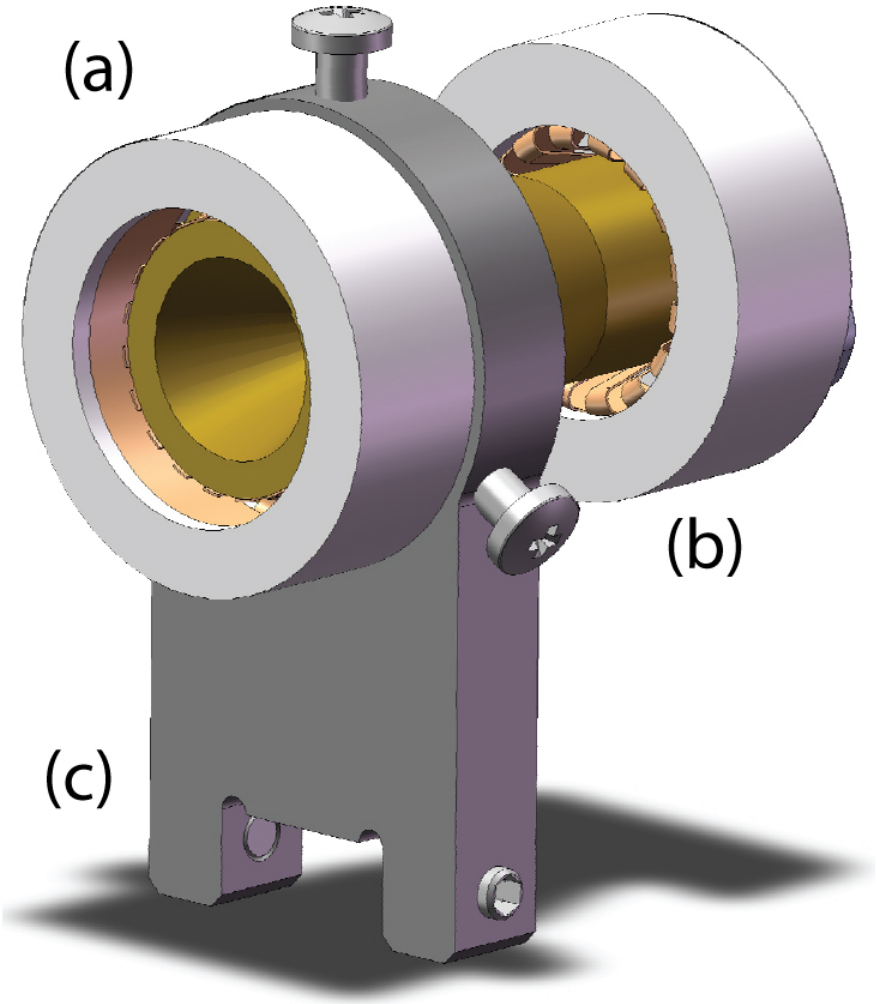

Figure 2.19: CAD model of EM detector mounting fixture for the differential chamber. (a) HV connection, (b) ground connection, and (c) rail mount base are shown.

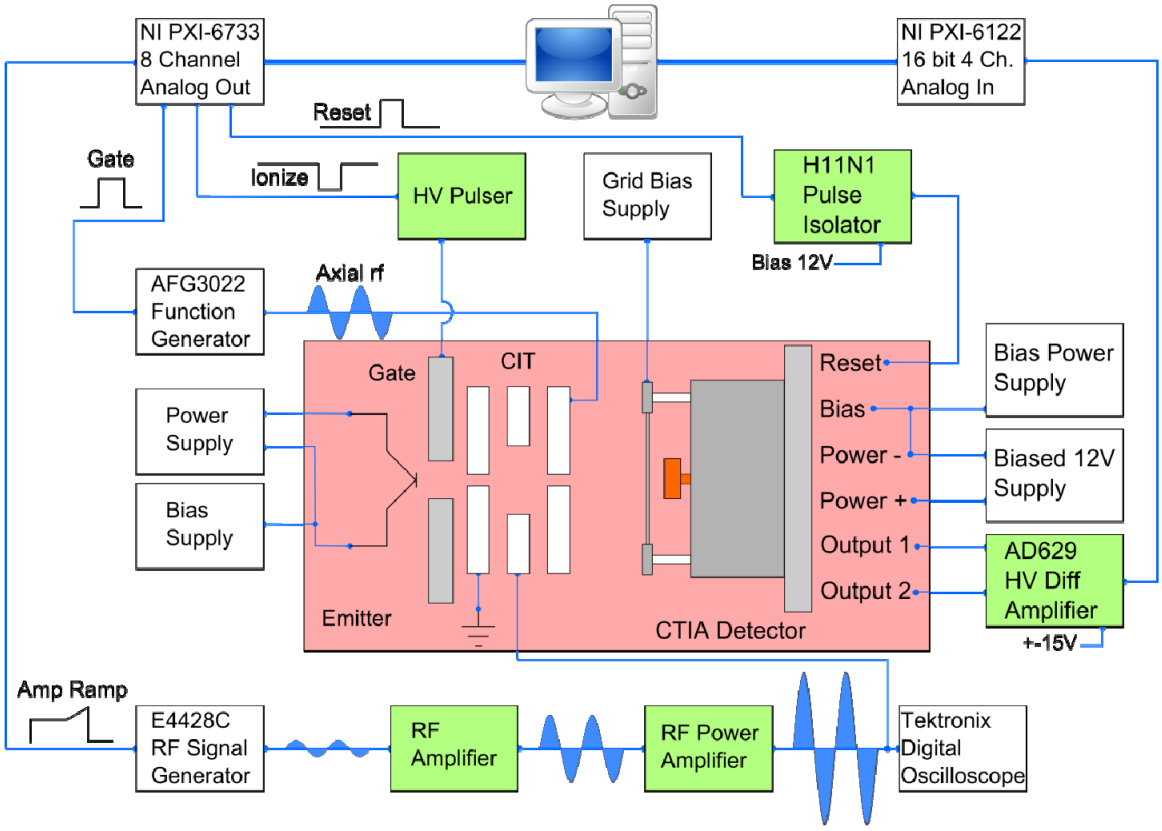

Figure 2.20: Schematic diagram of microscale CIT MS instrument with pressure-tolerant FC detector. Custom and commercially available electronics are represented in green and white, respectively. The vacuum chamber is represented in red.

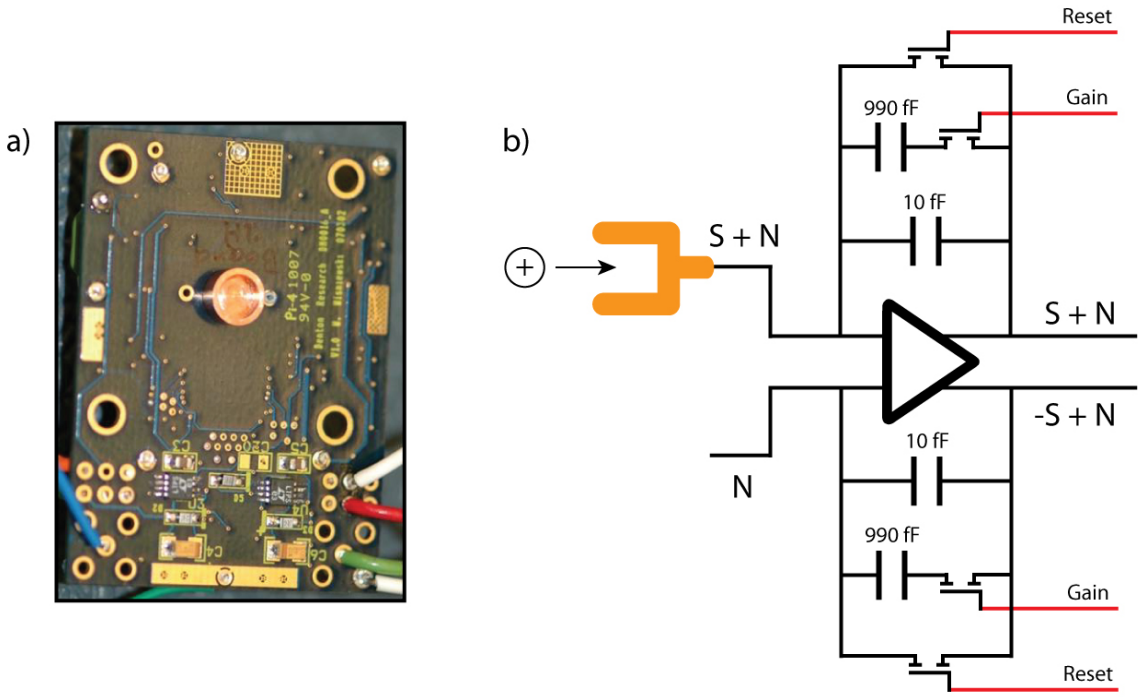

Figure 2.21: (a) Image of assembled CTIA detector circuit board. The copper Faraday cup is visible near the center. (b) Schematic of a single CTIA inside the custom IC. Feedback capacitors provide two gain settings for each amplifier and the CTIA is reset by shorting these capacitors to dissipate stored charges. Signal (S) is present only on one input while common mode noise (N) is present on both. The differential outputs are subtracted to double the signal intensity and cancel common mode noise.

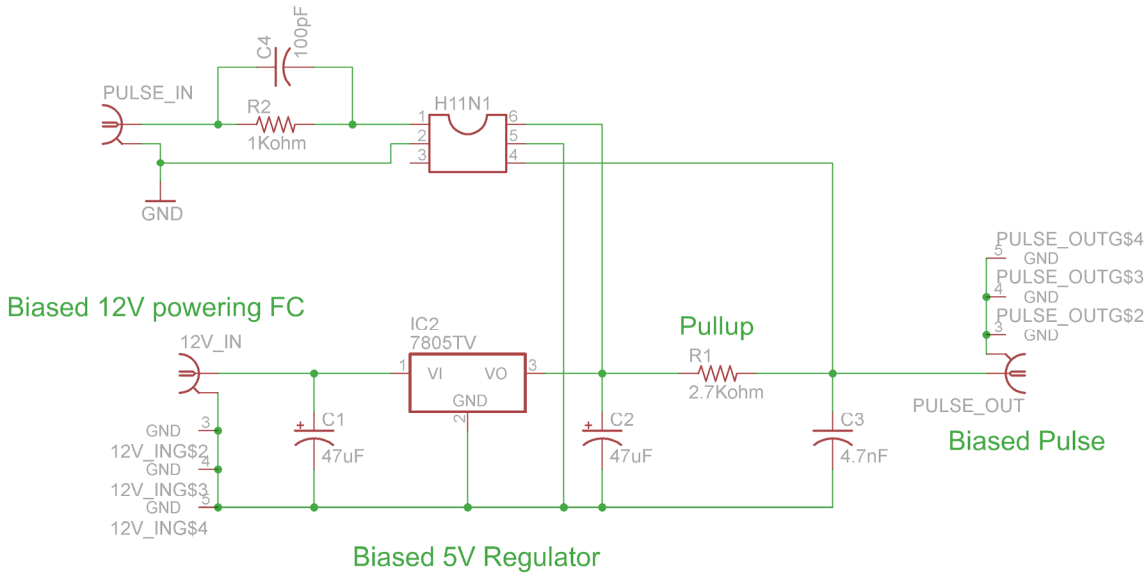

Figure 2.22: H11N1 logic optocoupler circuit used for biasing FC detector reset pulse.

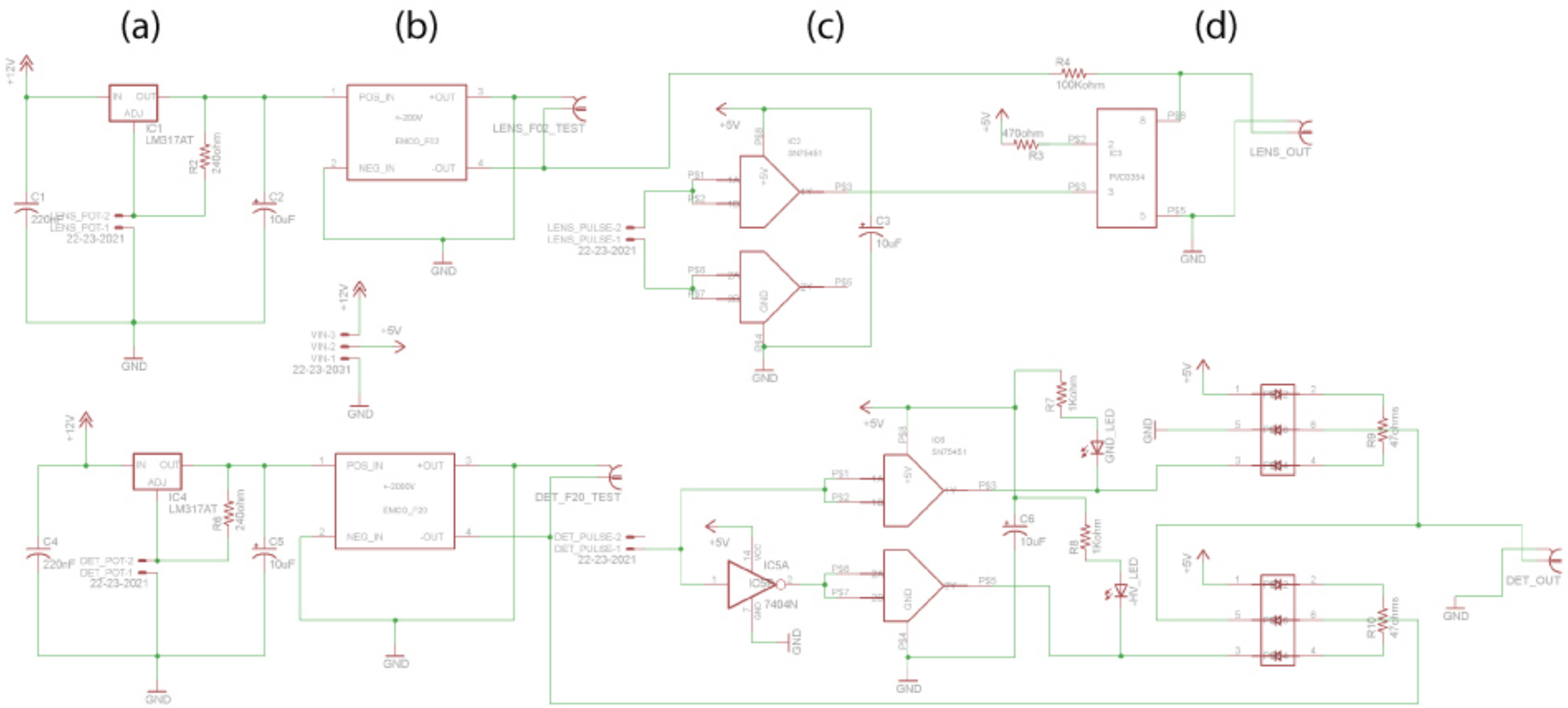

Figure 2.23: Schematic of HV pulsing power supply v2.0 designed to drive the ionization gate electrode (top) and EM detector (bottom). Each channel has a separate (a) variable power supply, (b) HV power supply, (c) 5 V logic circuitry, and (d) HV switch.

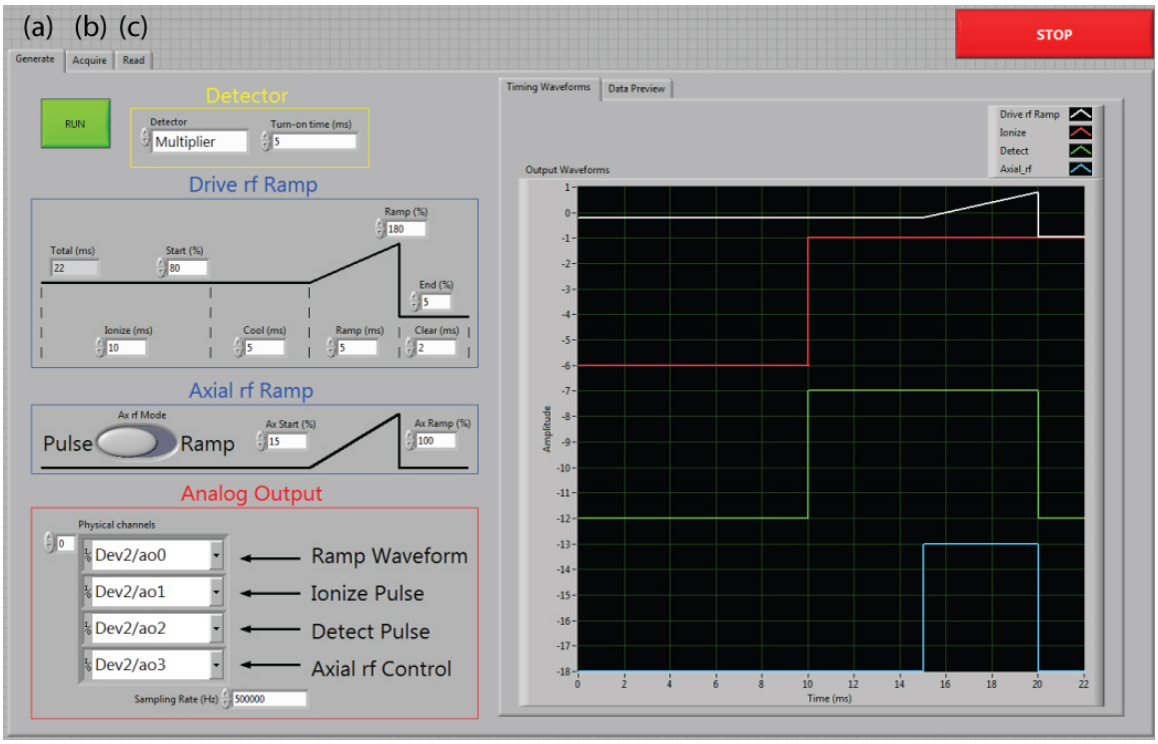

Figure 2.24: Instrument control software GUI (Control_Experiment.vi) showing modules for (a) generating control waveforms, (b) acquiring data, and (c) reading saved data.

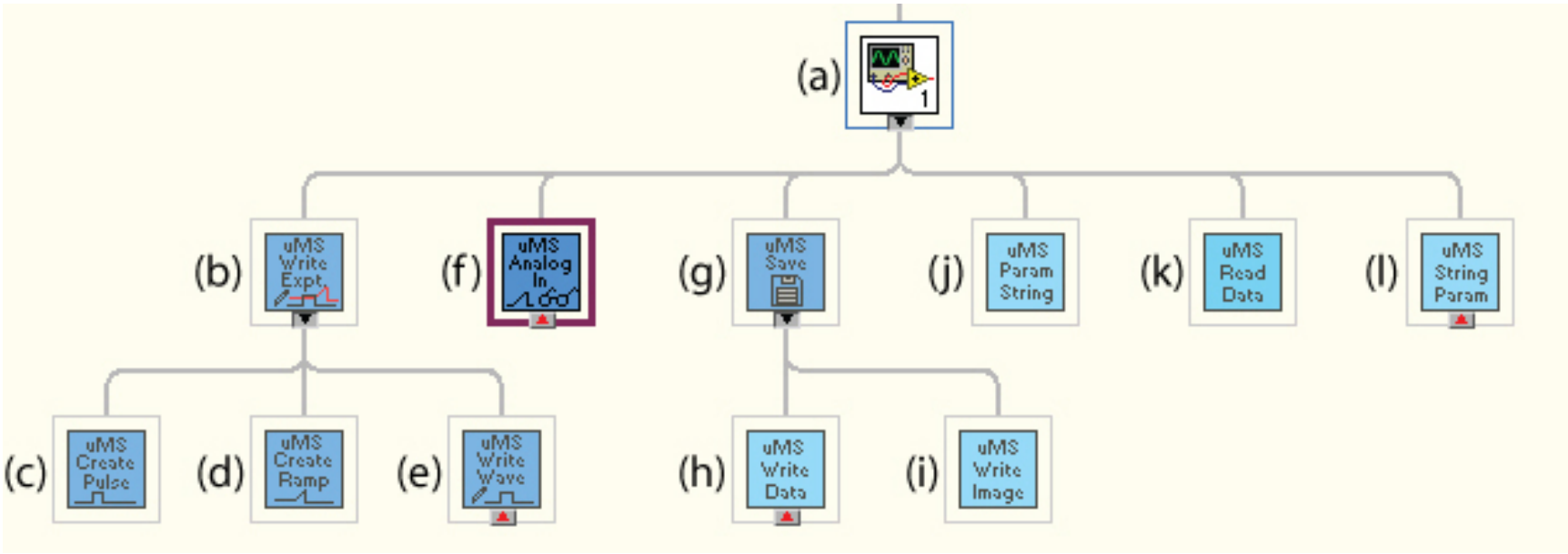

Figure 2.25: Instrument control software diagram illustrating the relationships between various subprograms. The programs shown are (a) Control_Experiment.vi, (b) Write_Experiment_Waveforms.vi, (c) Create_Pulse.vi, (d) Create_Ramp.vi, (e) Write_Waveforms.vi, (f) Analog_In.vi, (g) Save.vi, (h) Write_Data.vi, (i) Write_Image.vi, (j) Parameters_to_String.vi, (k) Read_Data.vi, and (l) String_to_Parameters.vi.

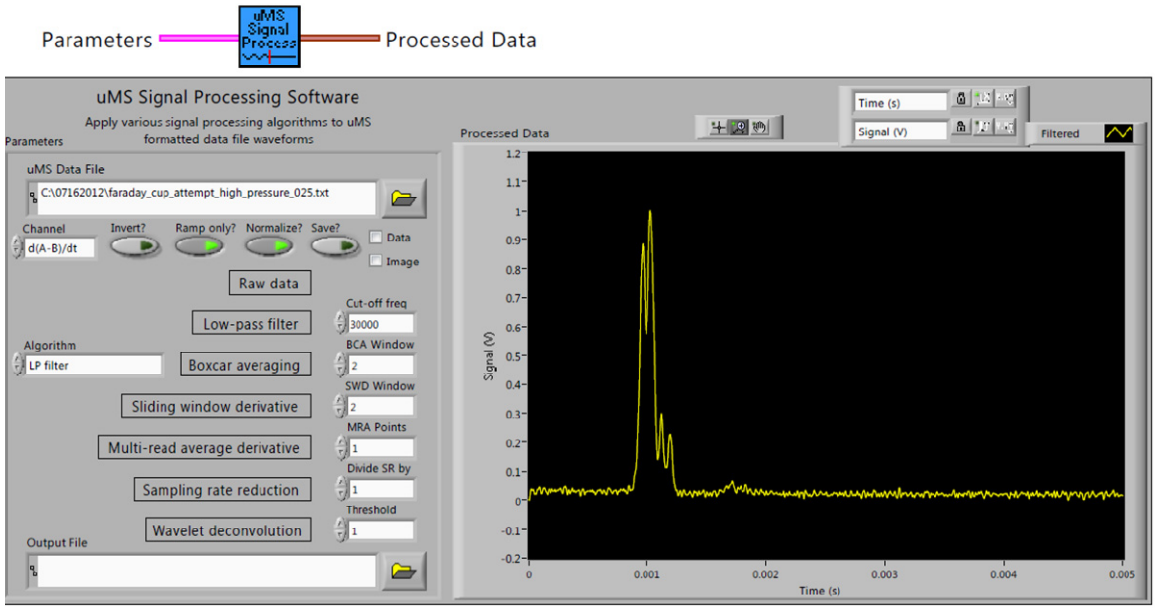

Figure 2.26: Signal processing program for performing various processing algorithms to MS data (signal_processing.vi). This program can be used in a standalone mode or embedded inside another program.

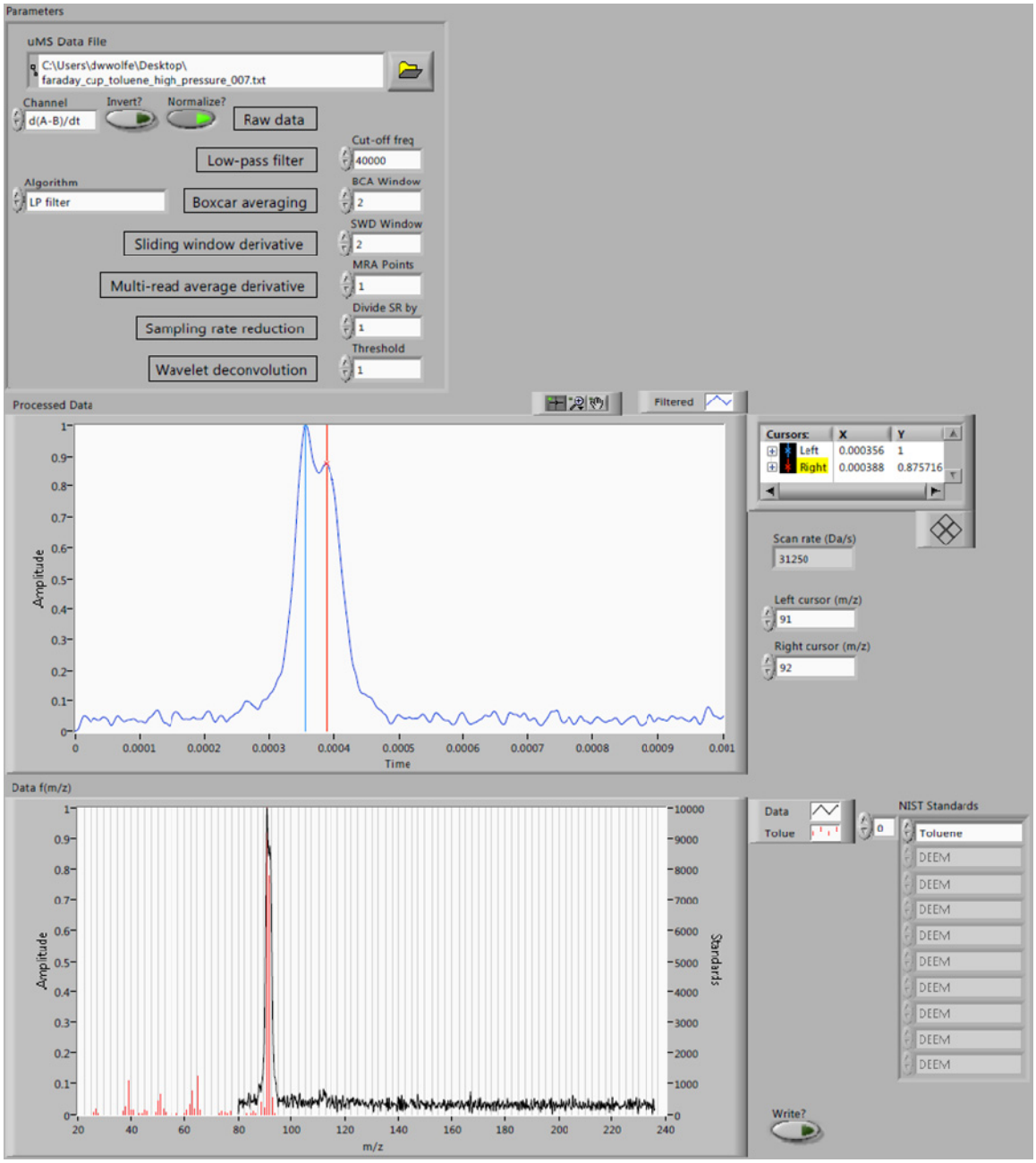

Figure 2.27: Post-processing program for converting MS data from a time axis to a *m/z* axis (create_calibrated_mass_axis.vi). The user moves two cursors to known *m/z* value peaks (top graph) and runs the program to display the data as a function of *m/z* (bottom graph). Signal processing functionality is embedded and NIST standard spectra can be overlaid with experimental data for validation.

2.12 References

(1) Bonner, R. F.; Fulford, J. E.; March, R. E.; Hamilton, G. F., *Int. J. Mass Spectrom. Ion Phys.* 1977, *24*, 255-269.

(2) March, R. E., *Mass Spectrom. Rev.* 2009, *28*, 961-989.

(3) Koppenaal, D. W.; Barinaga, C. J.; Denton, M. B.; Sperline, R. P.; Hieftje, G. M.; Schilling, G. D.; Andrade, F. J.; Barnes, J. H. I. V., *Anal. Chem.* 2005, *77*, 418A-427A.

(4) Andresen, R. D.; Page, D. E., *Nucl. Instrum. Methods* 1970, *85*, 141-142.

(5) Wiza, J. L., *Nucl. Instrum. Methods* 1979, *162*, 587-601.

(6) Knight, A. K.; Sperline, R. P.; Hieftje, G. M.; Young, E.; Barinaga, C. J.; Koppenaal, D. W.; Denton, M. B., *Int J Mass Spectrom* 2002, *215*, 133-139.

(7) Babis, J. S.; Sperline, R. P.; Knight, A. K.; Jones, D. A.; Gresham, C. A.; Denton, M. B., *Anal. Bioanal. Chem.* 2009, *395*, 411-419.

(8) March, R. E., *J. Mass Spectrom.* 1997, *32*, 351-369.

(9) Coombes, K. R.; Tsavachidis, S.; Morris, J. S.; Baggerly, K. A.; Hung, M. C.; Kuerer, H. M., *Proteomics* 2005, *5*, 4107-17.

CHAPTER 3

LOW-PRESSURE MS

3.1 Introduction

After building a functional MS instrument it was necessary to characterize its operation at conventional buffer gas pressures. This was accomplished through a series of experiments each varying a single experimental parameter. Resulting mass spectra were then compared to evaluate the effects of parameter variation on system performance. These characterization experiments generated a working knowledge of the system which served as a basis of operation for future experiments. Because many factors contribute to overall instrument performance, it usually was not possible to optimize a parameter only once and utilize the same value for all subsequent experiments. Therefore, typical experiments began with parameter values that were known to generally work and performance was then further optimized for a given instrument configuration.

Some mass spectra in this chapter are displayed as a function of time because conversion to a *m/z* axis would not add value in terms of data analysis. The time axis data is presented exactly as it was recorded from the instrument without any further data processing or manipulation. This raw data analysis is instructive since the time domain contains some information that is lost in the conversion to the *m/z* domain. For example, it would not be possible to see long-term signal drift or the effects of changing the RF amplitude if the spectra are plotted on a calibrated mass axis. Although a proper mass spectrum displays the data as a function of *m/z*, the time domain data will also be

considered spectra for the purpose of these characterization experiments since the conversion is a simple linear relationship between time and *m/z*.

3.2 Experimental parameter effects

MS experiments were performed at conventional ion trap pressures of a few mTorr to evaluate the effect of a given experimental parameter and to optimize instrument performance. These experiments were performed multiple times in the course of characterizing changes to the instrument or as a diagnostic tool in system troubleshooting. Representative data presented here were chosen to illustrate the effect of each experimental parameter on the resulting mass spectra.

The first step was to perform ionization inside the trap by activating the EI source. The number of ions created and therefore the signal intensity of the resulting mass spectrum was proportional to this ionization time for a fixed EI current (Figure 3.1) as anticipated. It was also verified that the signal intensity of the spectra increased as a function of the current supplied to the thermionic emitter (Figure 3.2). The emission current from a thermionic EI source is a function of temperature and increasing the heating current increases the emission current. This was verified using a picoammeter to measure the current at the entrance endcap, the ring electrode, and at the front of the electron multiplier as a function of the heating current supplied to the tungsten filament (Figure 3.3). Additionally, the alignment between the emitter tip and CIT endcap hole is important for maximizing signal intensity since tungsten filament EI sources have a small emission area of 5×10^{-5} cm^2. Figure 3.4 shows spectra taken with ≈100 μm lateral changes in filament position. An increase in signal of approximately one order of magnitude was obtained when the endcap and filament were properly aligned. Disk

emitter EI sources were found to eliminate this alignment issue because the emission area is large enough to tolerate small misalignments between the EI source and endcap hole. The larger emission area was also found to be advantageous when working with CIT arrays because it was possible to perform EI simultaneously in multiple traps due to the larger electron beam size.

The RF waveforms applied to the CIT had the most noticeable influence on instrument performance. As was previously described[1], applying axial RF to the endcap electrode to perform resonance ejection significantly improved resolution (Figure 3.5). The achievable resolution for a given CIT and drive RF frequency is extremely sensitive to the frequency and amplitude of this axial RF signal. Therefore axial RF optimization is required for every experiment. The drive RF scan rate is also important as it affects the location in the mass scan where a given ion will appear (Figure 3.6). The peaks simultaneously spread apart and move toward the right side of the ramp because it takes longer for the RF amplitude to reach the ejection voltage for a given ion at a slower scan rate. The RF amplitude ramps used for this scan rate experiment are shown in Figure 3.7. The slope of these ramps define the mass scan rate for the spectra in Figure 3.6. If the scan rate is too fast, the various ions will be bunched together increasing the signal intensity but reducing the resolution. Slowing the scan rate causes the peaks to spread apart resulting in increased resolution. This is clearly demonstrated in Figure 3.8 where all seven Xe^+ isotopes are visible at the slower scan rate while at the faster scan rate only five peaks were detected. However, this strategy of reducing the scan rate has practical limitations because if the rate is too slow the ions will not eject from the trap within a reasonable time frame resulting in very broad peaks and low signal intensity. Therefore

it is desirable to choose a scan rate that is as fast as possible to maintain signal intensity while still resolving the ions of interest. The scan rate is initially measured in V/s but is later converted to Da/s when the data is converted to the *m/z* domain. The drive RF amplitude also affects the location of a given ion in the mass scan. Figure 3.9 shows Xe^+ ions shifted in time toward the right side of the ramp as the RF amplitude is decreased since it takes longer for the RF amplitude to reach the ejection voltage for a given ion. In this experiment the peaks also spread apart slightly because the scan rate also decreases when the RF amplitude is decreased. This is a consequence of the RF ramp generation because it is configured to scan between values specified by percentage multipliers for the amplified signal generator output. The same percentage of a smaller amplitude value results in a smaller voltage range and therefore a slower scan rate.

The construction and alignment of the CIT electrodes were also found to be very important for achieving optimum performance.[2] Figure 3.10 shows poor performance in an improperly aligned trap and improved performance of the same trap following electrode realignment. The exact magnitude of the electrode misalignment is unknown but it was estimated to be ≈100 μm. To address this problem, a procedure was developed for improved electrode alignment utilizing pins and concentric alignment holes in the electrodes. The spacing between electrodes is also important because it changes the z_0 value for the trap and therefore affects the quality of the resulting electric field by changing the relative strength of higher-order field components.[2] Figure 3.11 shows an experiment with the same trap electrodes at several different spacing values. These data demonstrate that an optimum spacing value of 375 μm for this trap significantly improves both resolution and signal intensity. Optimizing the electrode spacing for a given trap

size is time consuming because the chamber needs to be vented and subsequently pumped down each time a new trap configuration is tested.

To address the need for rapidly optimizing electrode spacing, a custom system was designed for changing the spacing of the trap in place without venting the vacuum (Figure 3.12). This custom electrode positioning system utilized a motion control system (NSC200, Newport, Irvine, CA) to allow movement of the trap electrodes under vacuum. The completed system included two vacuum compatible linear actuators to control the position of one endcap and the position of the ring electrode while the second endcap remained stationary (Figure 3.13). The actuators allow for convenient and reproducible adjustments to the CIT electrode spacing under vacuum with a step size of 0.1 μm. Figure 3.14 shows this positioning system installed on the isobaric vacuum chamber flange. Custom LabVIEW software (Figure 3.15) was written to control the linear actuators using LabVIEW drivers supplied by Newport. This control software provides independent functionality for reading the electrode positions, seeking to new positions, moving a given number of steps, and saving or returning to given positions. In addition, the software implements a fully automated geometry adjustment that moves both electrodes the appropriate number of steps to create the desired trap spacing value. The manual electrode spacing experiments in Figure 3.11 were repeated using this electrode positioning system (Figure 3.16). Signal intensity in this data is low because the trap was not operating under optimum conditions. Electrode alignment is the most likely cause of the low signal intensity. At the time these experiments were performed it was difficult to properly align the electrodes and make them parallel to each other in the moveable mounting scheme used for the positioning system. Although the trap was not working

perfectly, it was still possible to record spectra of Xe^+ at the spacing values used for the manual spacing experiments. The data are more difficult to interpret but they also indicates that a 375 μm spacing value yields the best combination of resolution and S/N. A major advantage of this positioning system is the possibility of evaluating much smaller changes to electrode spacing than a manual spacing experiment could achieve. Theoretically, the smallest achievable change in spacing is 0.1 μm but it is unlikely there will be any significant difference in trap performance with this small of a change. To evaluate the effects of finer spacing value changes, a similar experiment was performed in which the electrode spacing was changed in 25 μm increments (Figure 3.17). The resulting data indicated an optimum spacing value of 400 μm, illustrating the effectiveness of the positioning system for optimizing the spacing value more quickly and accurately than what would be possible with manual spacing experiments. Overall, this electrode positioning system functioned as expected although alignment of the trap is a significant challenge because of the extra degrees of freedom inherent in the moveable electrode mounting scheme. It should be possible to achieve better MS performance with this system in future experiments by incorporating the advances to electrode design and fabrication made over the past few years.

Other attempts at optimizing CIT geometry involved using two different fabrication methods for producing electrodes (Figure 3.18). Initially the electrodes were fabricated using conventional machining procedures on a CNC mill. Traps built from these machined electrodes had nearly cylindrical wall profiles (Figure 3.19) and produced good resolution but relatively low signal intensities. These machined traps were difficult to reproducibly assemble to a working condition on initial attempts because uncertainties

in the hole locations caused misalignment problems. Second generation devices were fabricated using wet chemical etching methods and photolithographic processes to produce the electrodes. This strategy significantly improved the reproducibility of a given trap because the features were more accurately located on the electrodes. The signal intensities produced by these etched traps were found to be significantly greater than the machined electrodes. A small cusp feature was left on the inside of the ring electrode as a consequence of the isotropic etching process (Figure 3.20). This cusp likely causes changes to the electric field inside the trap resulting in a slightly lower resolution for the etched traps compared to a properly functioning machined trap. The size of the endcap hole can also affect performance because a larger hole will allow more electrons to enter the trap and more ions to leave the trap. However, if the endcap hole becomes too large it will adversely affect the electric fields inside the trap and degrade instrument performance.[2] These effects are evident in Figure 3.21 as the signal intensity increases between 300 and 400 μm endcaps but then decreases between 400 and 600 μm endcaps. Additionally the spectrum taken with 600 μm endcaps is distorted and contains more noise due to improper ion ejection from the trap.

Signal averaging was employed to improve S/N at the expense of spectral acquisition time. When the trap was generating strong signal intensities a single scan spectrum would be recognizable, although noisy (Figure 3.22). Increasing the number of averaged scans to 10 and finally 100 caused the S/N to improve significantly. In these cases it was possible to use low numbers of averaged scans to produce sufficient S/N in the resulting spectra. However, in experiments with weak signal intensity, a single scan spectrum is not recognizable (Figure 3.23). For these experiments it was necessary to

perform signal averaging with 100-1000 consecutive scans to generate a recognizable mass spectrum. If the averaged signal intensity is too low it is possible to increase the current preamplifier gain to generate a larger voltage from the same detector output. In practice a preamplifier gain of 200 nA/V was almost exclusively used because it provided the largest gain with sufficient bandwidth to resolve the mass peaks (Figure 3.24). When the gain was increased to 100 nA/V, the internal circuitry of the preamplifier changed and a drastic decrease in bandwidth was observed. These high preamplifier gain values were only used to find very small signals when the instrument was not functioning properly.

The final parameter varied during these characterization experiments was the helium buffer gas pressure since it is known to have an effect on instrument performance.[3] The isobaric chamber instrument was initially limited in terms of achievable buffer gas pressures because there was no valve between the chamber and pump to reduce vacuum conductance. However, preliminary experiments with increased helium pressure showed promising results (Figure 3.25). This data shows an increase in both signal intensity and resolution when the helium buffer gas pressure was increased from 1.3 to 19 mTorr. This is a relatively small change in buffer gas pressure but the results justified construction of the differential vacuum chamber to further explore the MS performance as a function of buffer gas pressure.

3.3 RF noise effects

Since the stability parameter q_z is directly proportional to RF amplitude, any uncertainty in the RF amplitude will cause a corresponding uncertainty in q_z. Therefore ion ejection directly depends on the short and long-term stability of the drive RF amplitude. Figure 3.26 illustrates the effects of severe short-term RF amplitude

instability. This data consists of single scan spectra recorded two seconds apart. In this experiment, the Xe^+ peaks were shifting between two discrete locations in the ramp due to RF amplitude instability on the order of 20 V. If these short-term instabilities occur while the instrument is averaging spectra, reduced resolution and increased noise results due to the superposition of two sets of mass peaks (Figure 3.27). In this case the instability was caused by a tuning problem with the RF amplifier. Instrument performance improved significantly after re-tuning the RF amplifier (Figure 3.28). Figure 3.29 shows a second example with a smaller RF amplitude instability but the effects are still significant. The magnitudes of these instabilities are unknown since it wasn't possible to accurately measure the RF amplitude at the time of these experiments. Re-tuning the RF amplifier resulted in a resolution improvement in this data as well. Long-term amplitude instability that occurred on the order of minutes had a less significant detrimental impact on mass spectra because the amplitude shifts did not occur while the instrument was averaging consecutive spectra. Figure 3.30 shows two spectra with a small time shift after 95 minutes of elapsed time. This type of longer term amplitude instability can be corrected when the mass axis is calibrated or could be eliminated with an RF amplitude feedback loop. Cross-talk between different RF amplifiers operating simultaneously at the same frequency was also observed to have a significant impact on instrument resolution (Figure 3.31). In this experiment, simply activating the drive RF on an adjacent MS system caused the S/N to decrease and peak widths to increase by at least a factor of 2. The performance returned to the original state after turning the other RF amplifier off. This problem was addressed by tuning RF

amplifiers to different frequencies when they are operating simultaneously in the same room.

To further investigate how sensitive the instrument was to RF amplitude instability, the control software was modified to digitally add white noise to the RF amplitude ramp waveform. This was the most convenient way to introduce a measured amount of noise for quantifying the effect of RF amplitude instability. Figure 3.32 shows an example of the noisy ramp waveforms used in these experiments. Ramp waveforms used in each scan were different because the noise was recalculated for each scan to simulate real noise. RF amplitude noise was added in mV quantities to a 1 V amplitude ramp waveform so in this case 1 mV = 1 part-per-thousand (ppth) noise. The results of this experiment show a significant decrease in resolution and signal intensity as the amplitude noise is increased from 0 to 21 ppth (Figure 3.33). This is a consequence of ions of a given *m/z* ejecting at slightly different times between subsequent scans. When these individual scans are averaged together the peaks broaden out significantly. Figure 3.34 shows the quantitative effects on peak width as a function of added noise. This experimentally confirmed the importance of good RF amplitude stability for optimizing instrument performance.

3.4 Analytes

Xenon gas was used for most experiments presented here because it was convenient to introduce as a gaseous analyte and has no associated reactivity or residue issues. It also provides a set of closely spaced isotope peaks that are good for evaluating the resolution of the instrument. Because it is an atomic species there is no fragmentation and the isotopic ratios can be directly compared to NIST standard spectra. Figure 3.35

shows a Xe^+ spectrum with all seven major isotopes present. Although xenon was used in most experiments, some common lab solvents were also used to demonstrate the feasibility of detecting small volatile organic analytes. These chemicals were introduced by first using a rough pump to remove atmospheric gasses from a sealed tube containing the solvent in liquid form. The vapor pressure of the solvent then filled the tube and was introduced into the instrument as a gas using a leak valve. Figure 3.36 shows a spectrum of toluene and Figure 3.37 shows a spectrum of hexane obtained in this manner.

Using these low-pressure MS experiments, we characterized the instrument performance and established a set of operating parameters for a typical experiment. Critical parameters such as CIT electrode alignment, axial RF configuration, and drive RF amplitude stability were identified. The knowledge gained in these low-pressure experiments proved essential for identifying and overcoming the experimental difficulties associated with high-pressure experiments.

3.5 Tables and figures

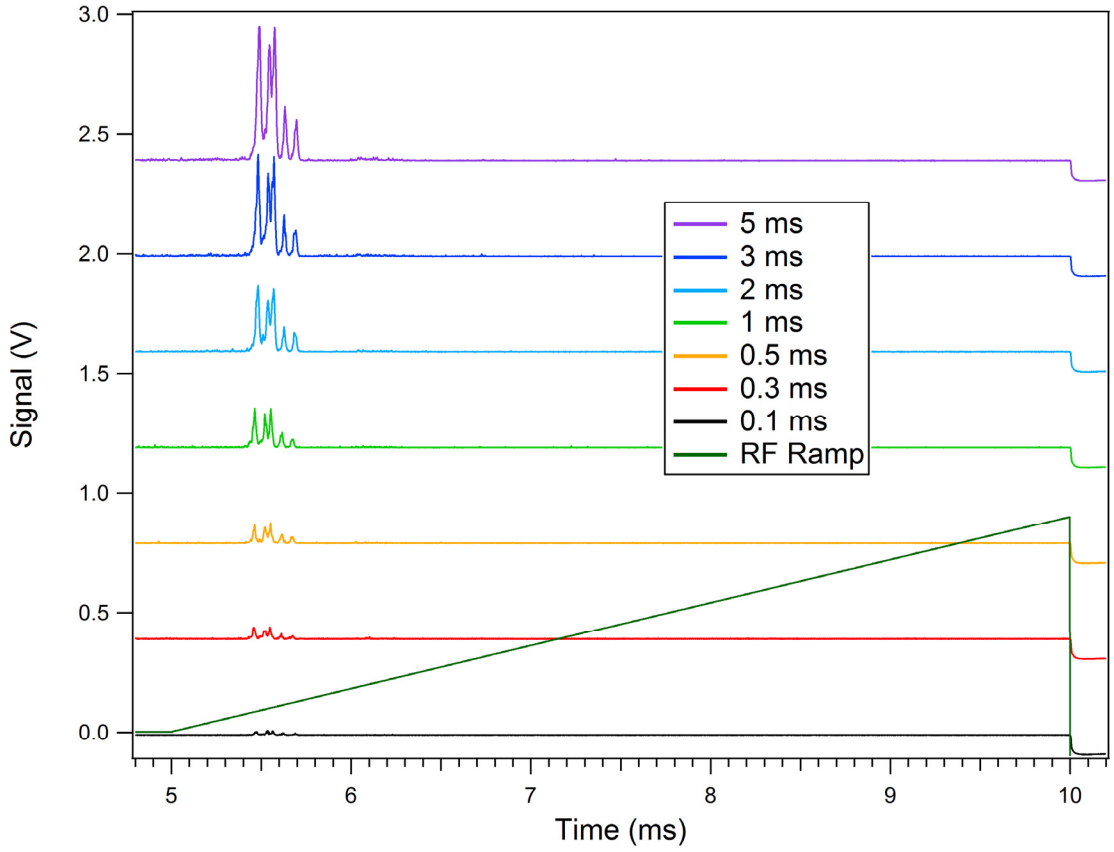

Figure 3.1: Plots of Xe^+ signal intensity as a function of ionization time (0.1 ms to 5 ms).

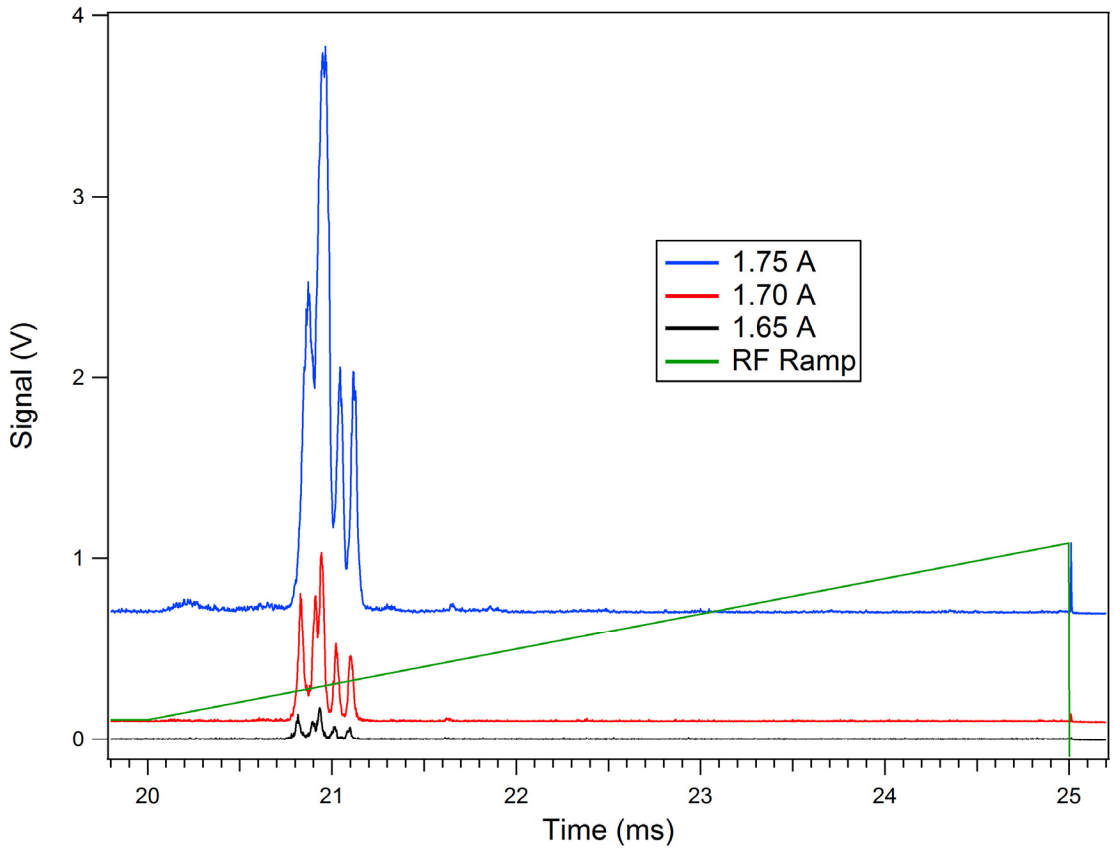

Figure 3.2: Xe^+ signal intensity increased with the heating current supplied to the EI source due to increased electron emission at higher temperatures.

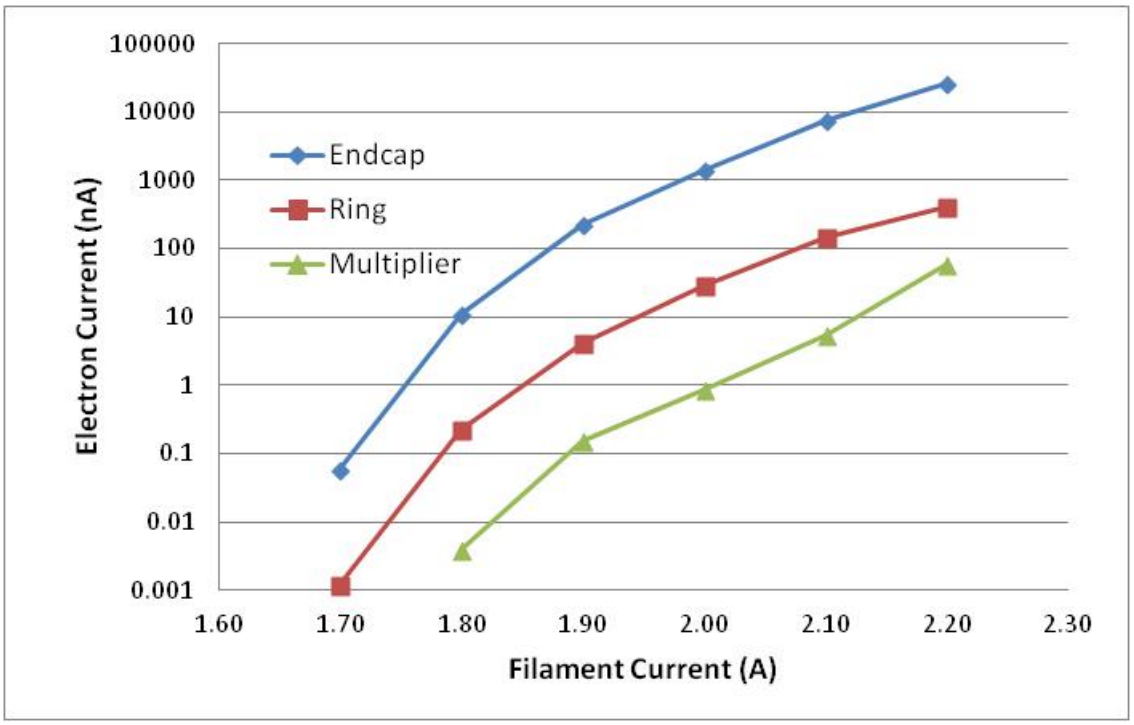

Figure 3.3: Electron emission current as a function of heating current for a tungsten filament EI source. Current was measured at the entrance endcap, the ring electrode, and the front of the electron multiplier to characterize the amount of current passing through the CIT.

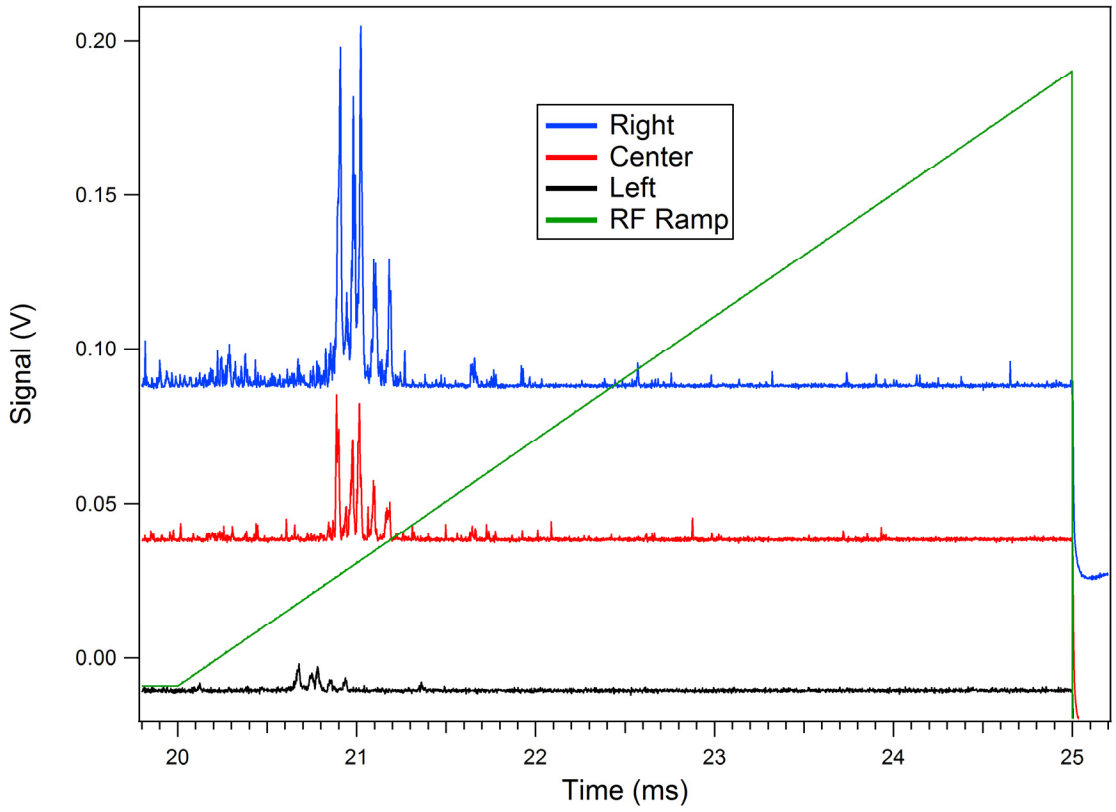

Figure 3.4: Plots demonstrating the changes in signal intensity as a function of tungsten filament positioning. The small emission area of the filament requires proper alignment with the CIT endcap hole to maximize the signal.

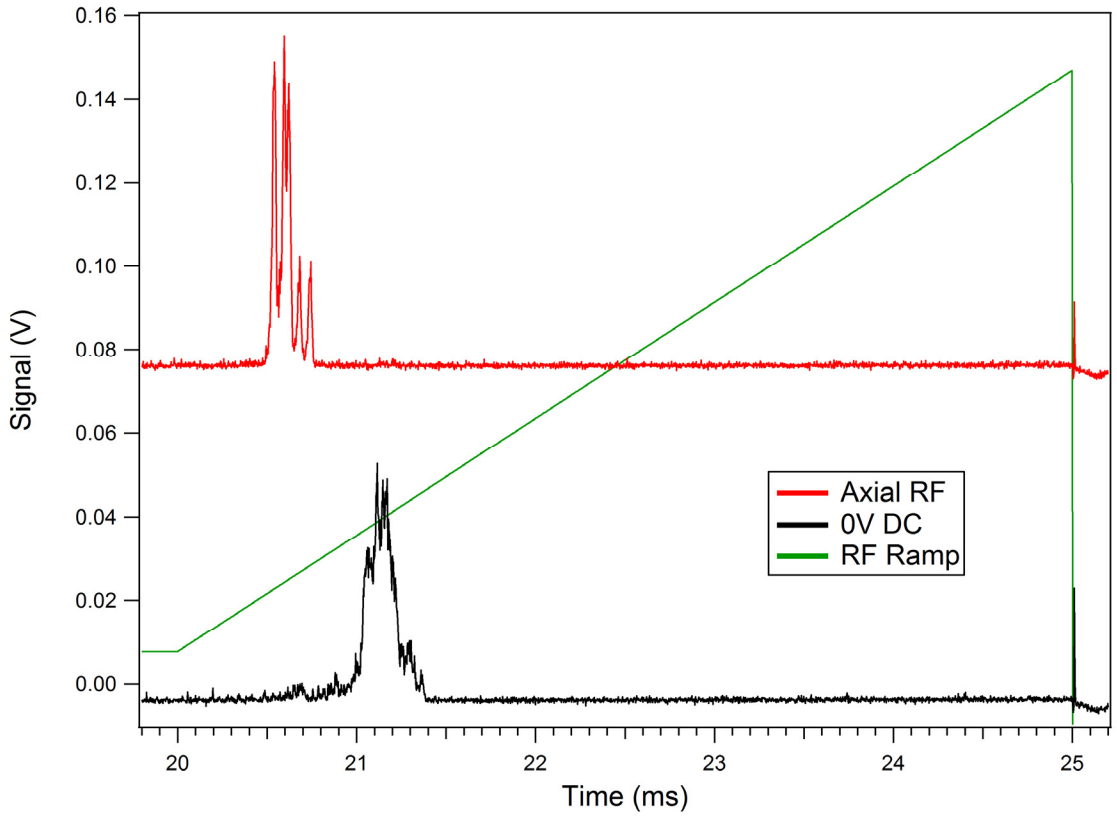

Figure 3.5: Applying axial RF to one endcap for performing resonance ejection significantly increased instrument resolution.

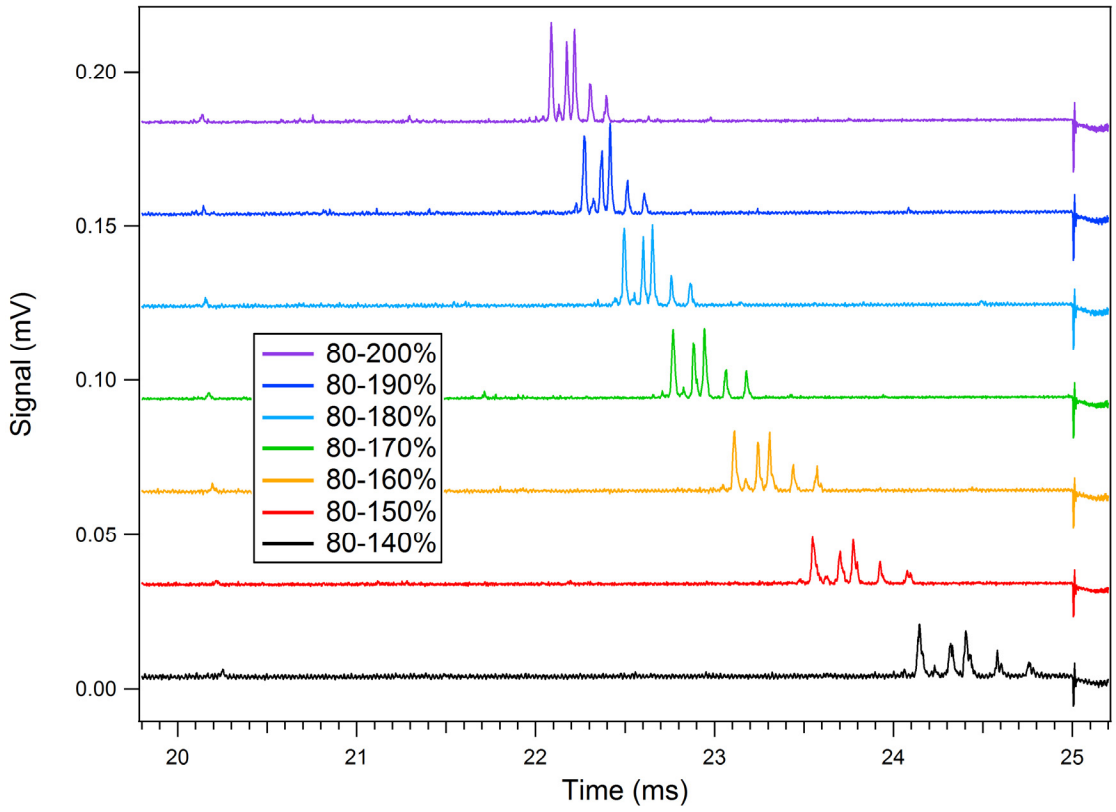

Figure 3.6: Decreasing the RF scan rate causes peaks to move toward the right side of the ramp and spread apart. This is a consequence of the slower scan rate because it takes longer to reach the ejection voltage for a given ion.

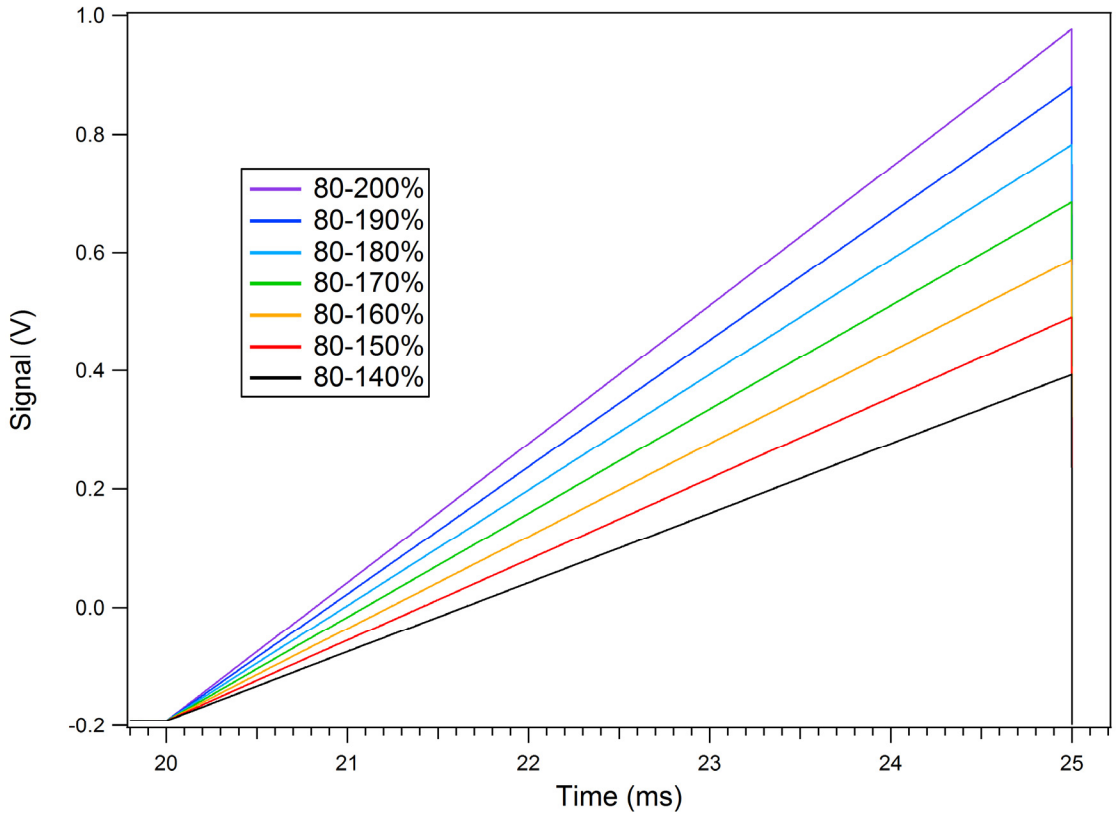

Figure 3.7: RF amplitude ramps used for scan rate experiment. A slower scan rate is graphically represented by a smaller slope during the ramp.

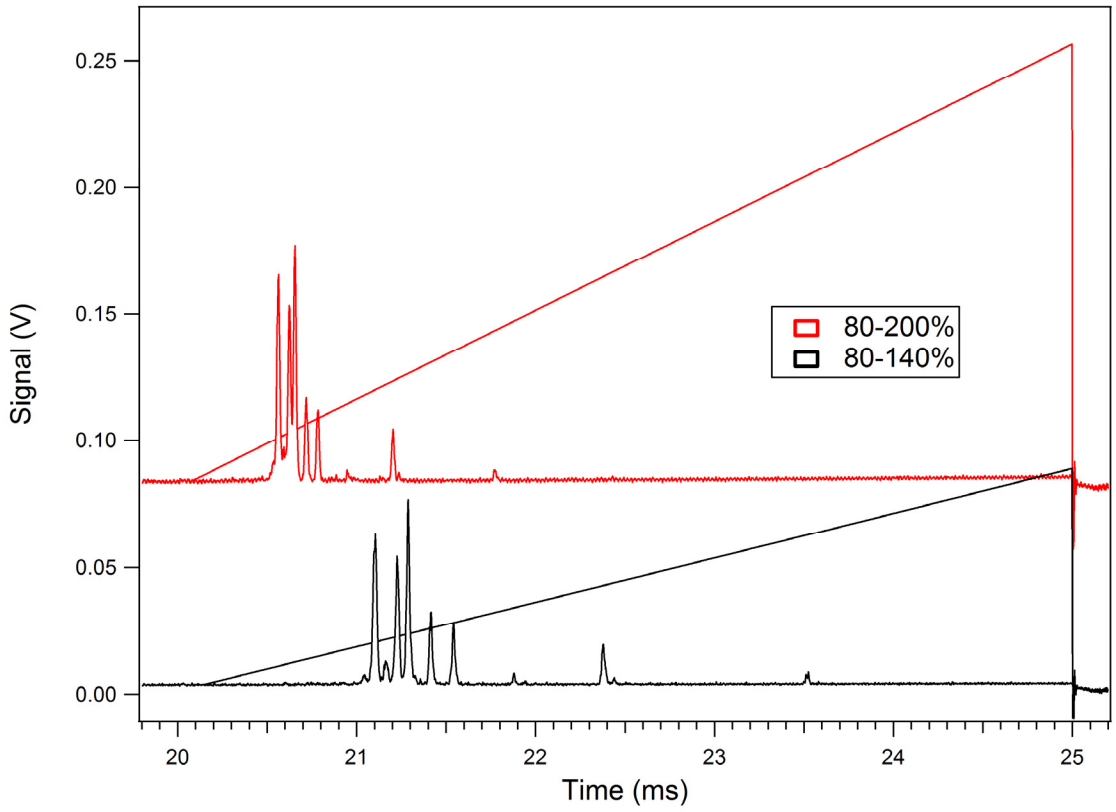

Figure 3.8: Decreasing RF scan rate causes peaks to move right and spread apart (increased resolution). The number of visible Xe^+ peaks increased from five to seven with this decreased scan rate.

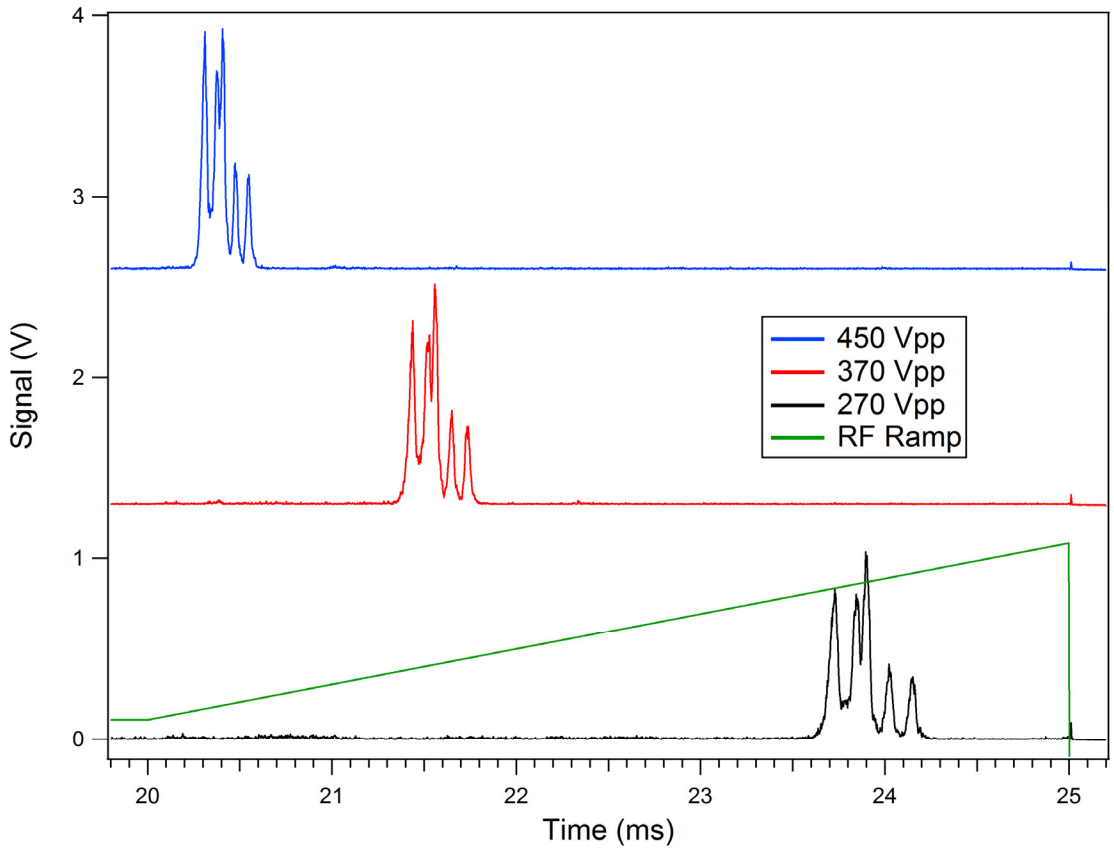

Figure 3.9: Decreasing drive RF amplitude causes peaks to shift toward the right side of the ramp because it takes longer to reach the ejection voltage for a given ion. The peaks also spread apart because the ramp scan is based on a percentage of the RF amplitude. Therefore, a decrease in RF amplitude causes a corresponding decrease in scan rate.

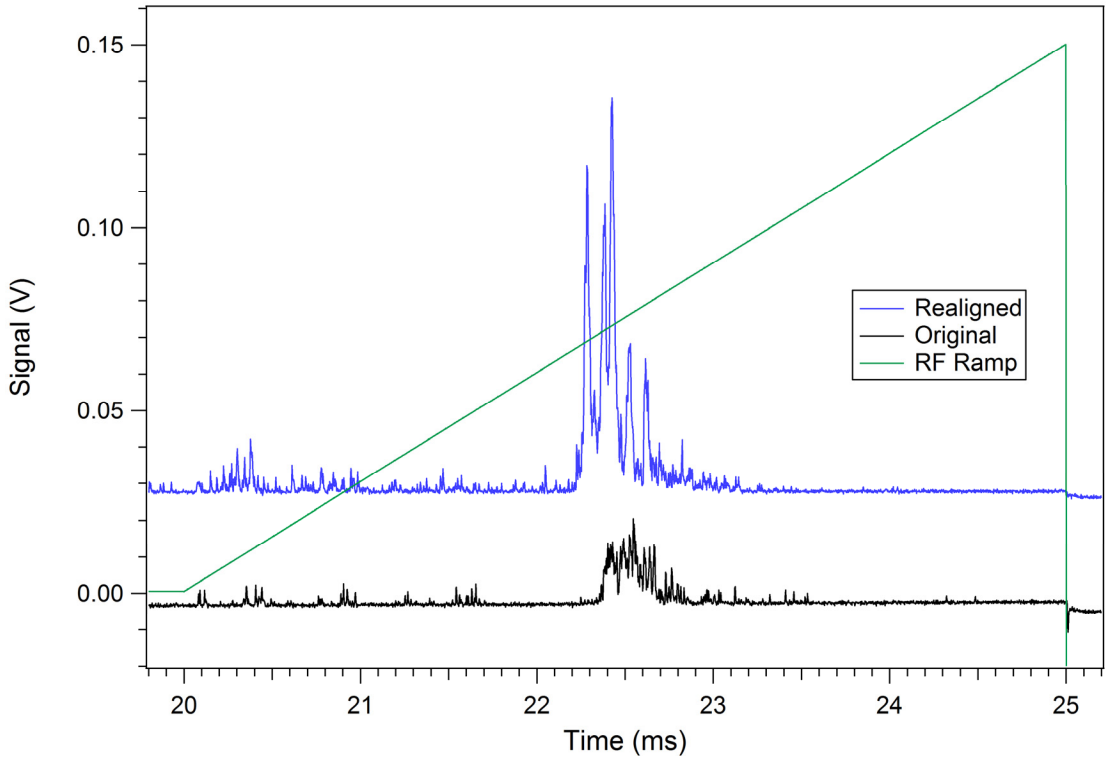

Figure 3.10: CIT electrode misalignment caused poor instrument performance. Realigning the same CIT resulted in a significant increase in resolution and signal intensity.

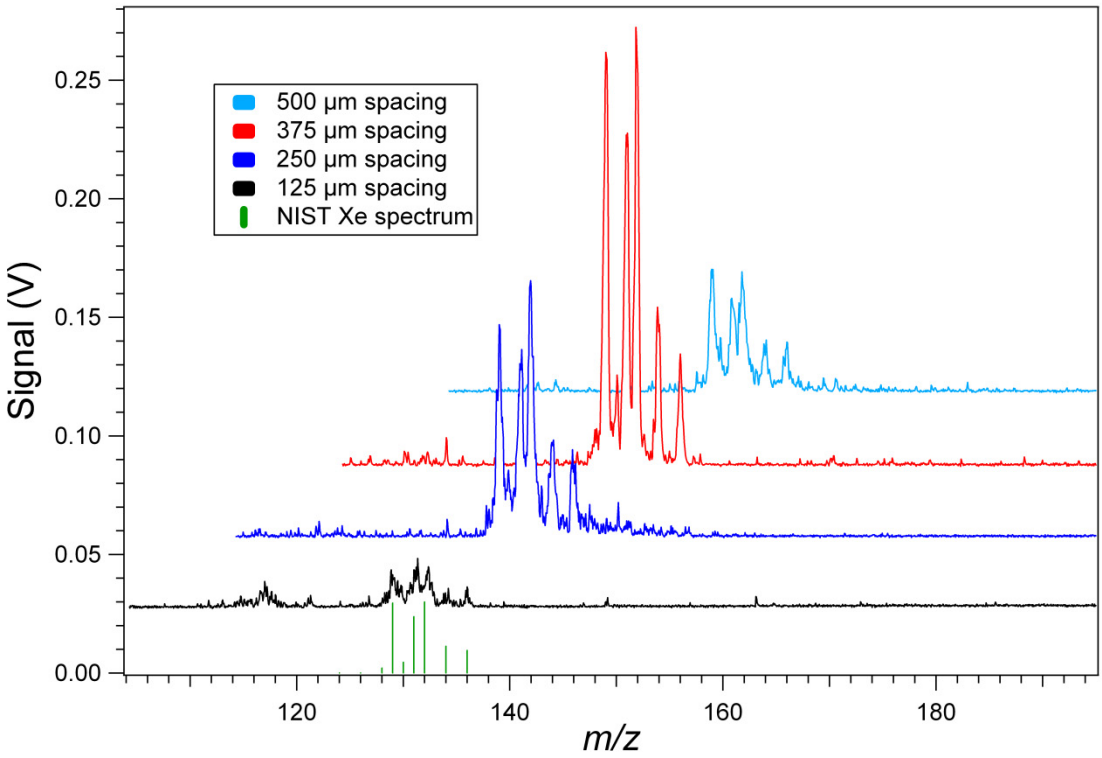

Figure 3.11: Electrode spacing experiment where four spacing values between 125 and 500 µm were evaluated by manually changing the number of spacers between electrodes. These data indicate an optimal inter-electrode spacing of 375 µm for a r_0 = 500 µm CIT. Successive curves are mass shifted by 10 Da for display purposes.

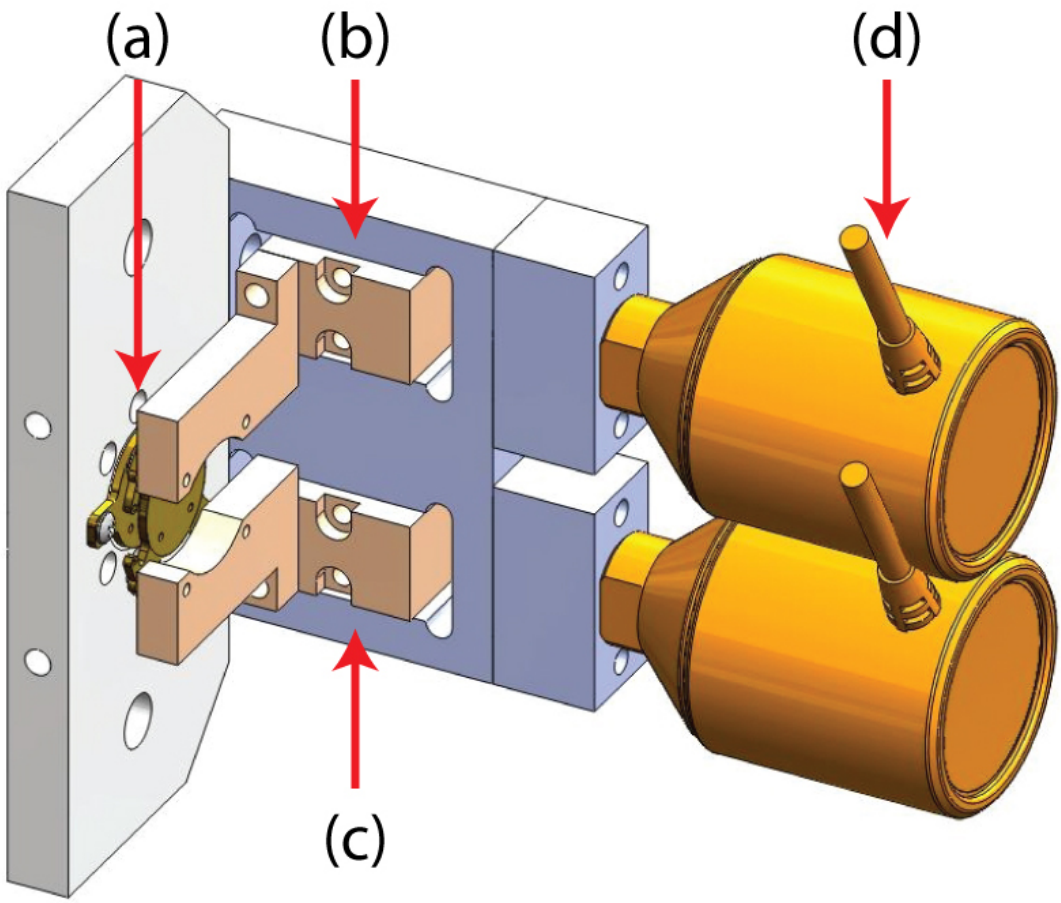

Figure 3.12: SolidWorks model of electrode positioning system showing (a) trap electrodes, (b) linear bearing for endcap, (c) linear bearing for ring, and (d) vacuum compatible linear actuators. This system was designed for adjusting electrode spacing without venting the vacuum chamber.

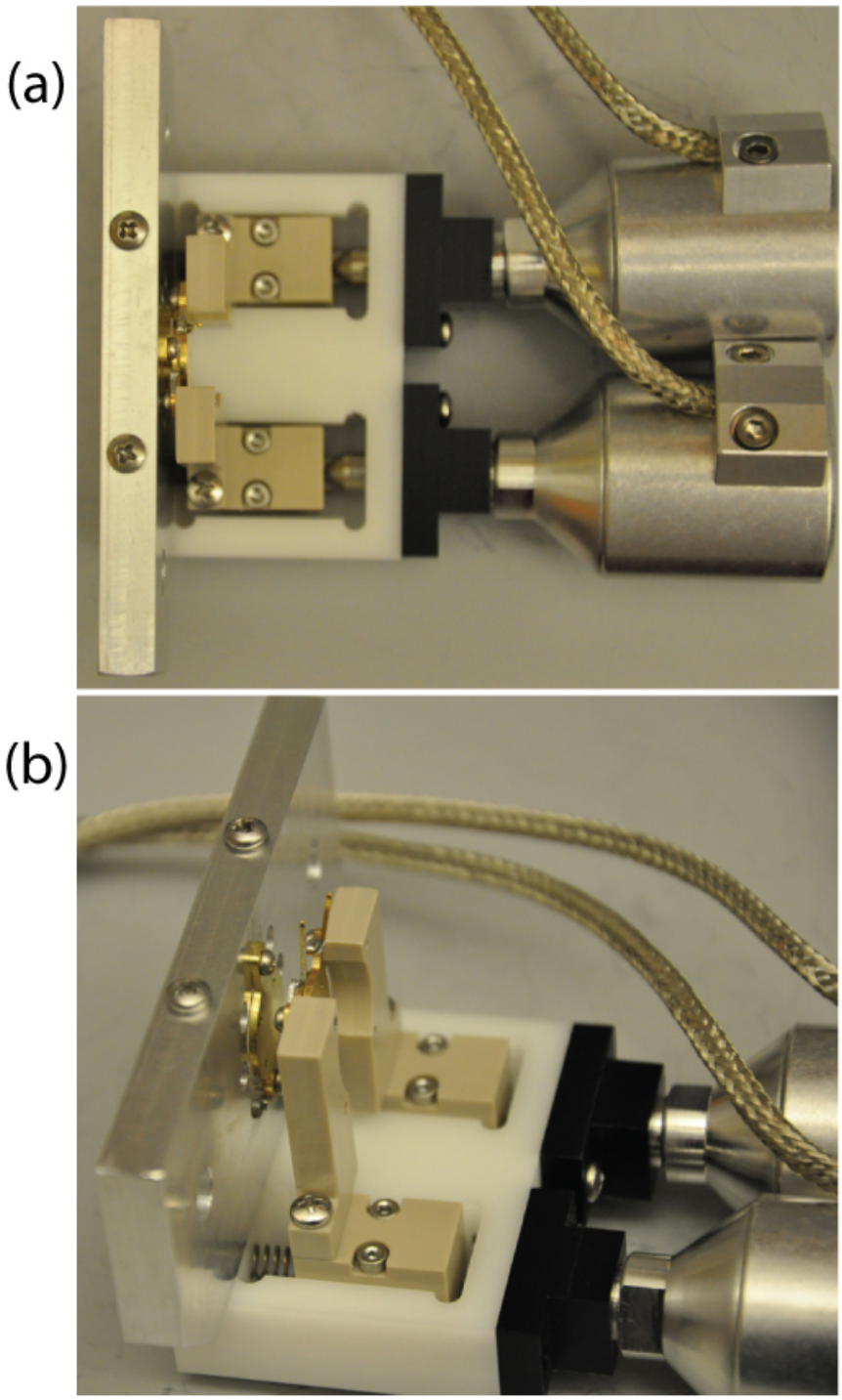

Figure 3.13: Images of the electrode positioning system from (a) top view and (b) side view.

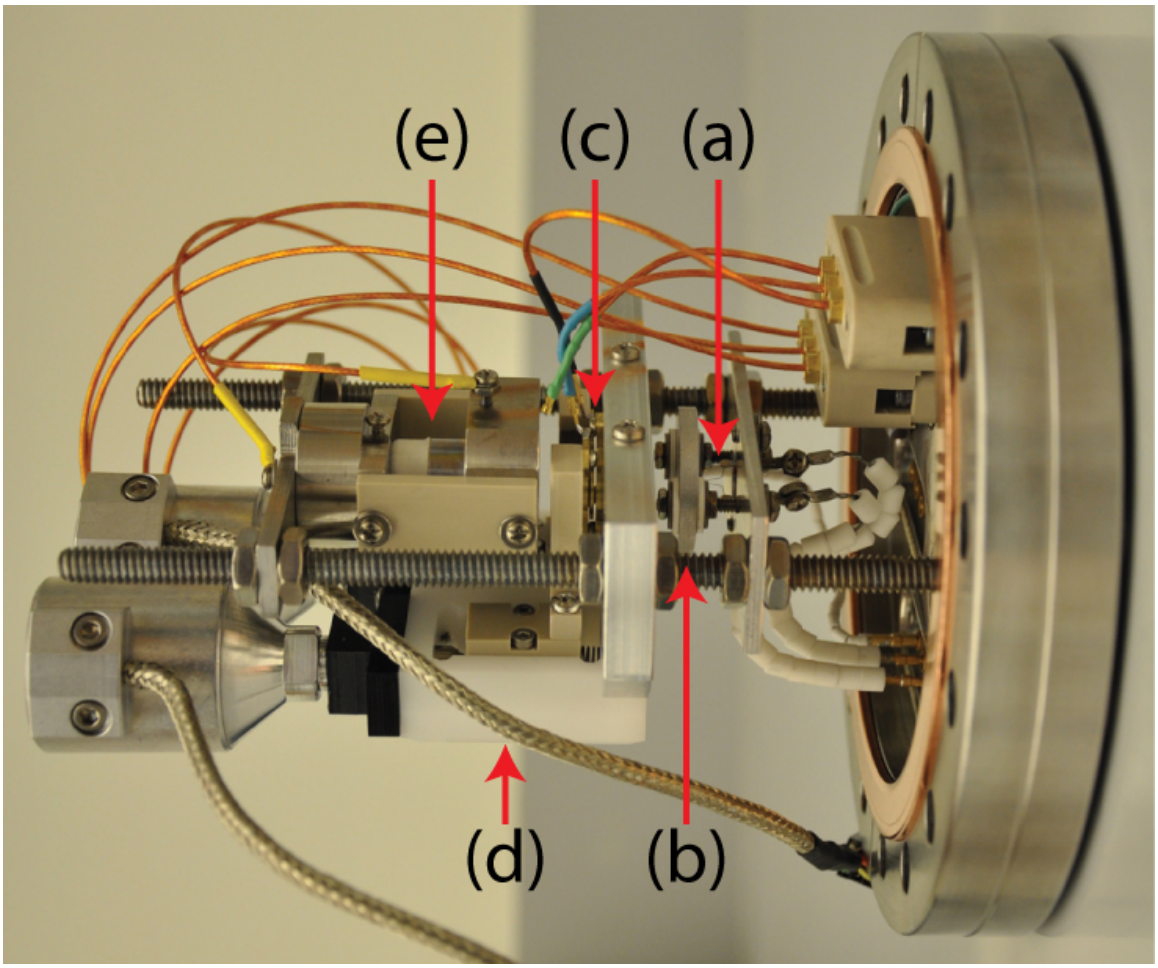

Figure 3.14: Image of the isobaric MS instrument with electrode positioning system installed on a 6" conflat flange. The instrument consists of: (a) tungsten filament, (b) gate electrode, (c) CIT, (d) electrode positioning system, and (e) electron multiplier.

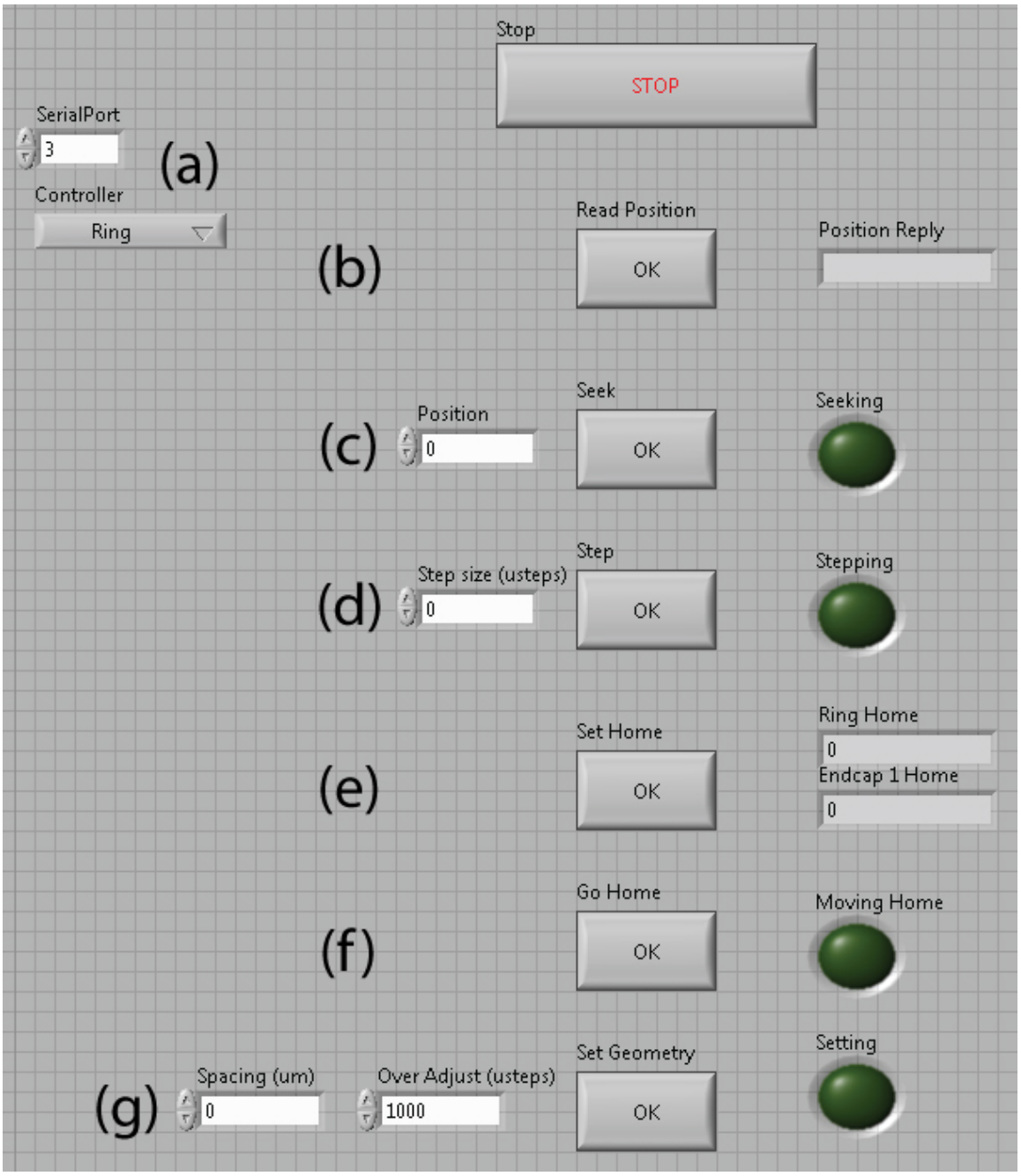

Figure 3.15: LabVIEW software for controlling the electrode positioning system. The user (a) chooses which electrode to move and then executes a command on that electrode. The software provides functionality to (b) read the current position, (c) seek to a new position, (d) move a given number of steps, (e) record a home position, (f) seek to the home position, and (g) automatically move both electrodes to create a given spacing.

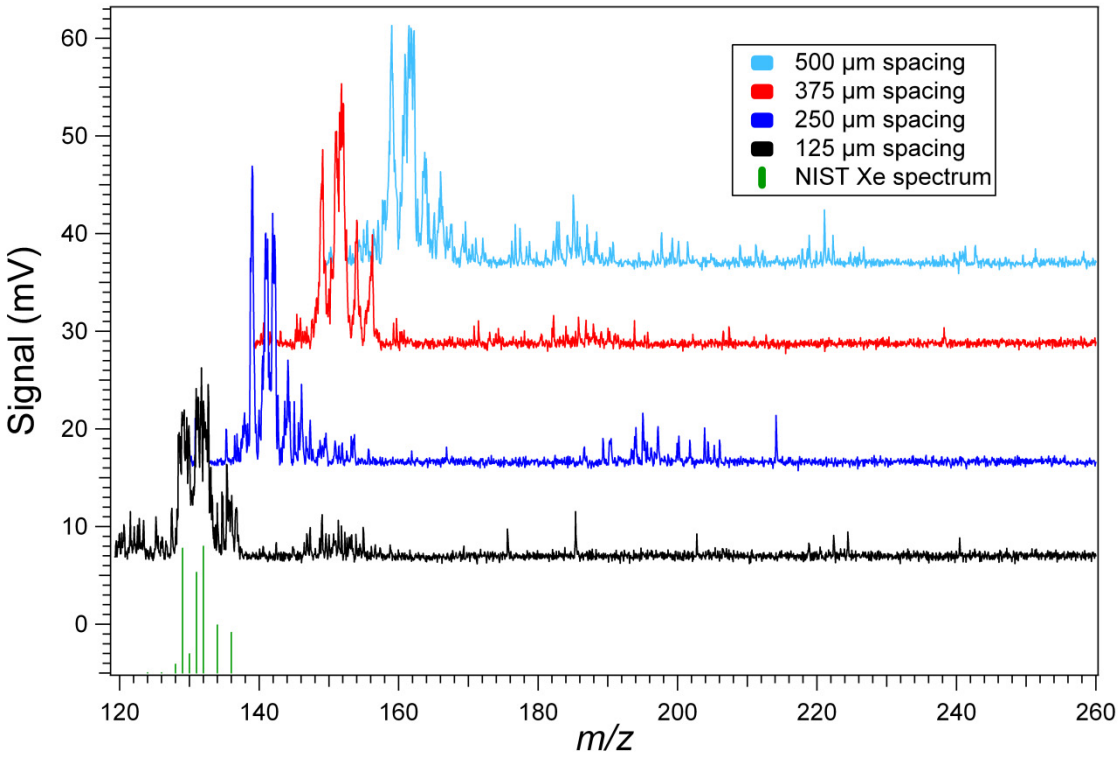

Figure 3.16: *In situ* spacing experiments with the electrode positioning system also indicate an optimum inter-electrode spacing of 375 µm for a r_0 = 500 µm CIT. The S/N is low for these data because the CIT was not producing strong signal intensities during this experiment. Successive curves are mass shifted by 10 Da for display purposes.

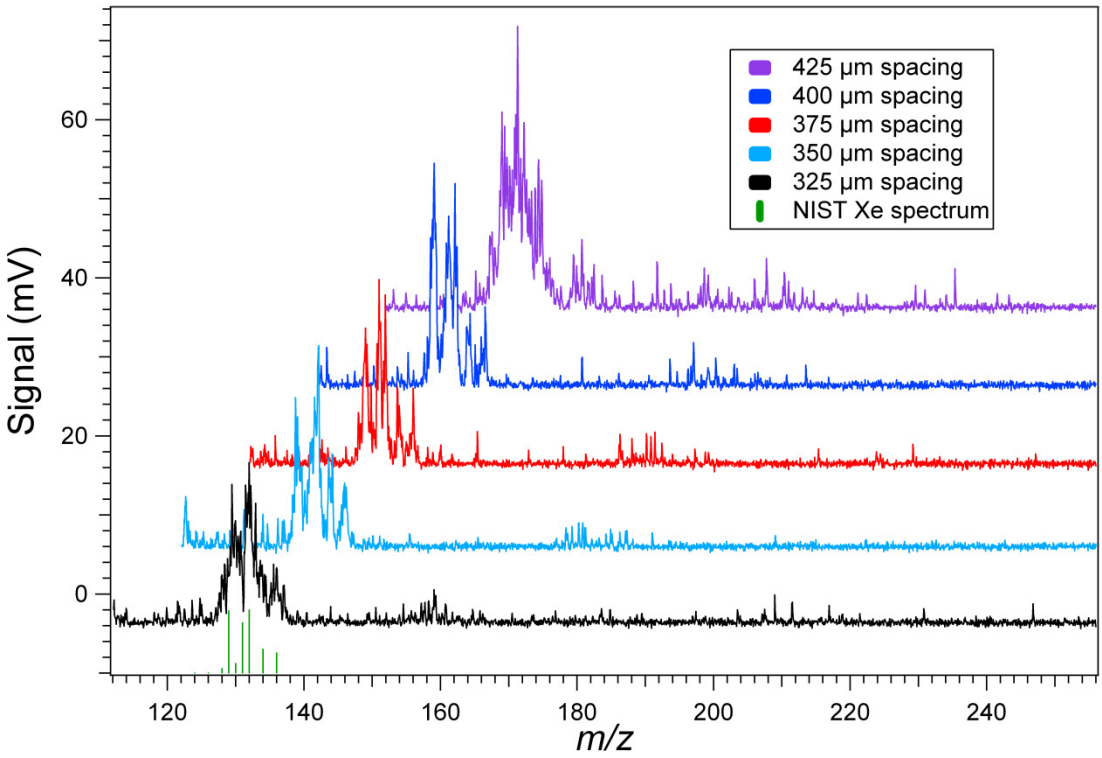

Figure 3.17: Further *in situ* spacing experiments show trap performance in 25 µm increments around 375 µm. These data indicate the 400 µm spacing is optimal for a r_0 = 500 µm CIT because proper isotope abundances are achieved while maintaining resolution. Successive curves are mass shifted by 10 Da for display purposes.

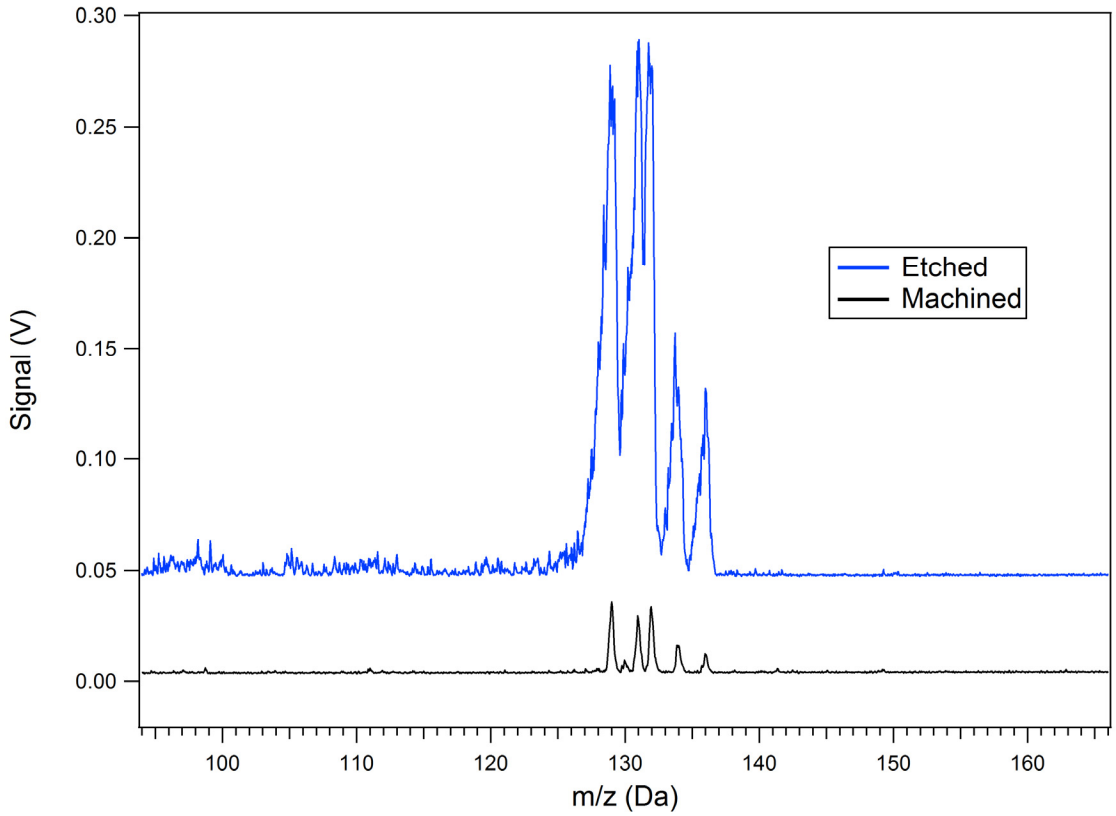

Figure 3.18: Xe^+ spectra generated by CNC machined and wet chemically etched trap electrodes. The machined traps generally give better resolution and etched traps give higher signal intensity.

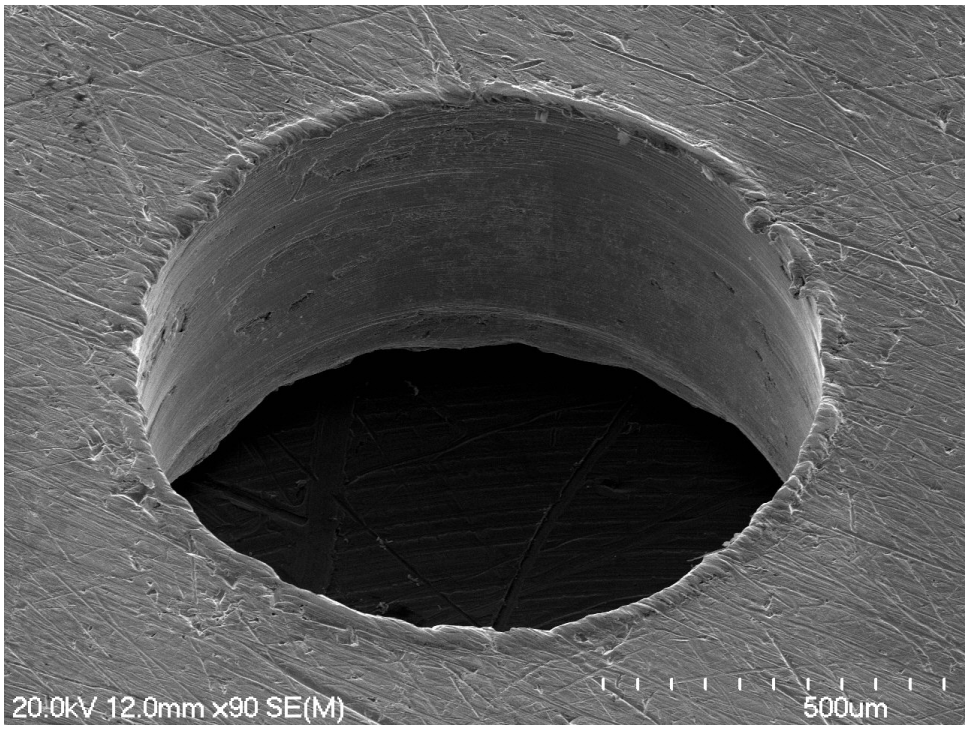

Figure 3.19: SEM image of a CNC machined 1 mm ring electrode hole. The hole profile is nearly cylindrical with small imperfections along the edge and inside the hole.

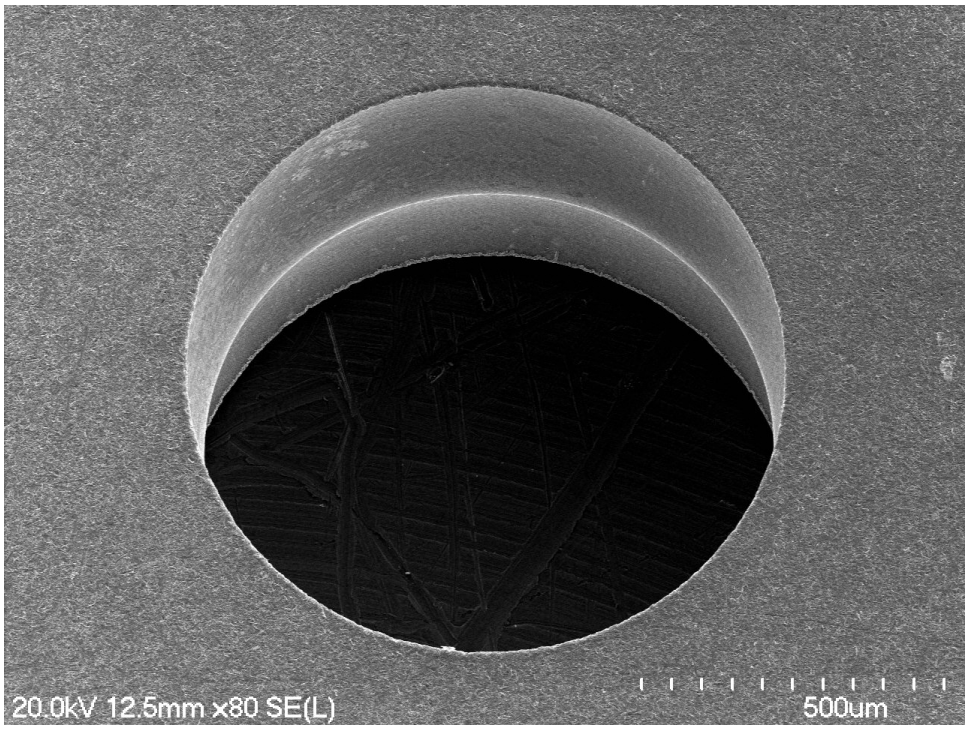

Figure 3.20: SEM image of a chemically etched 1 mm ring electrode hole. The surface finish is very smooth and uniform but there is a cusp feature inside the hole as a result of the etching process.

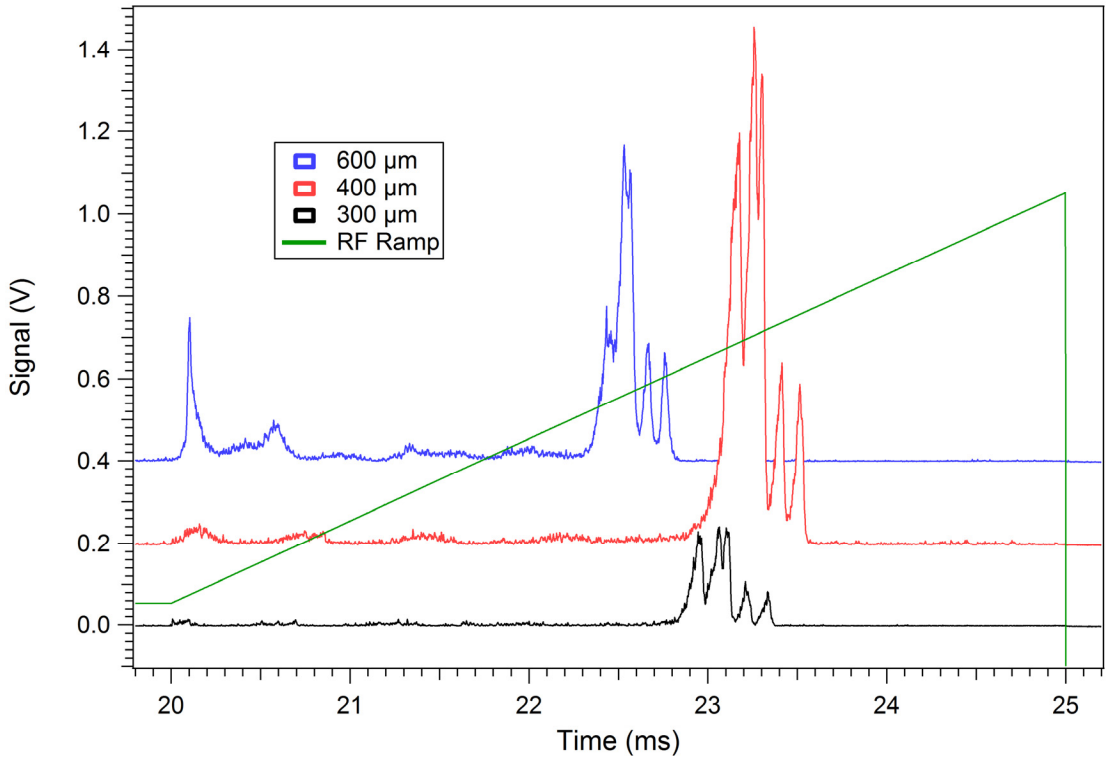

Figure 3.21: Experiment evaluating different endcap hole sizes. The 400 µm endcap has higher signal intensity than the 300 µm endcap because more electrons and ions can pass through the larger hole. The 600 µm endcap is too large, which is detrimental to the electric fields inside the trap. This results in distorted peaks and increased noise due to improper ion ejection.

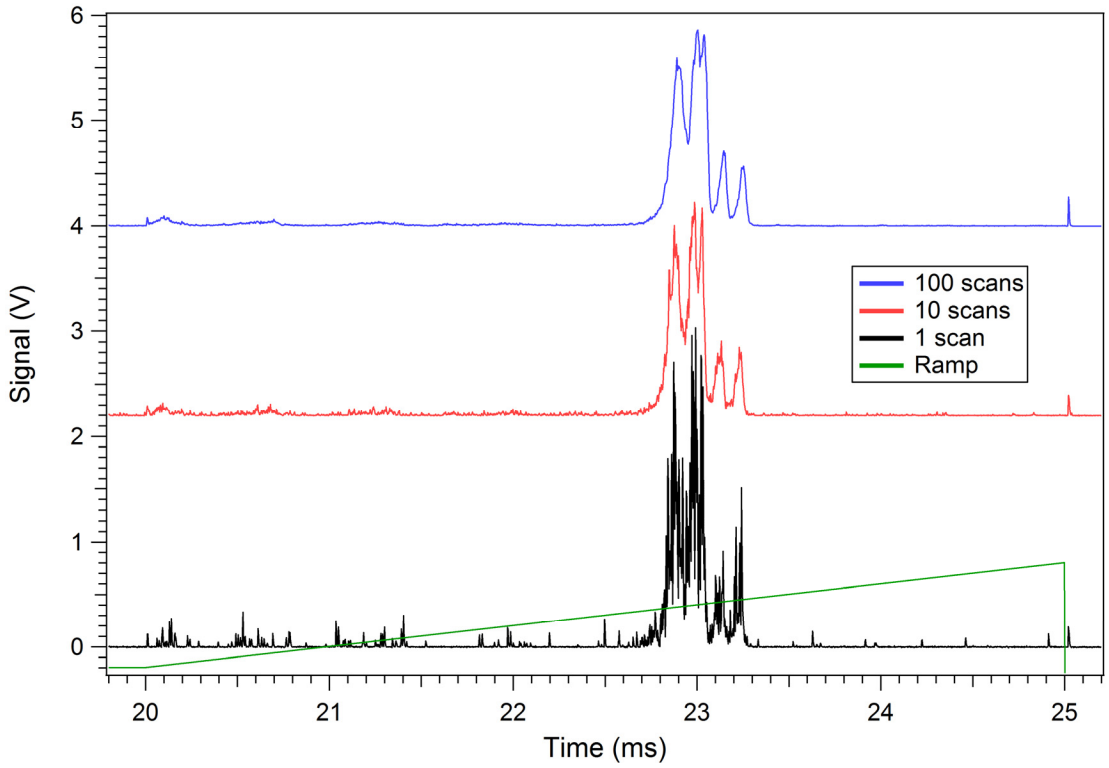

Figure 3.22: Increased signal averaging results in a corresponding increase in S/N. This data is recognizable as Xe^+ in the single scan spectra because the signal intensity is high.

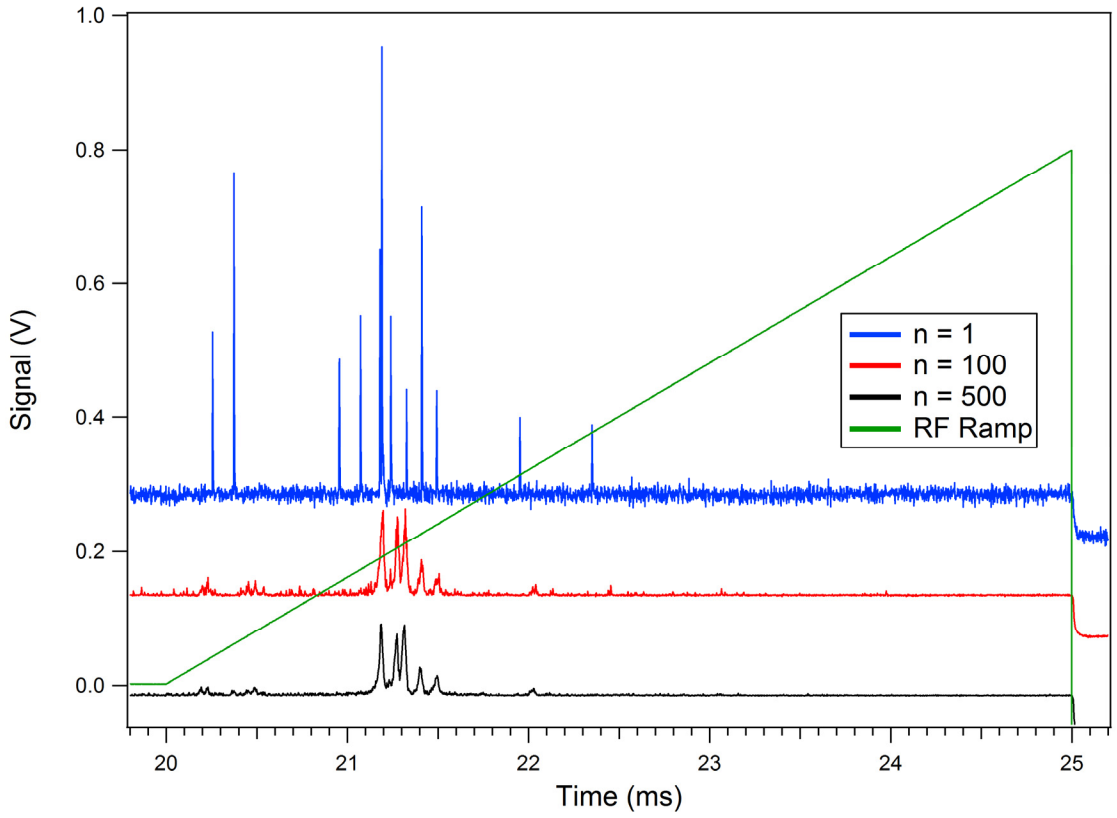

Figure 3.23: Increased signal averaging results in a corresponding increase in S/N. This data is not recognizable as Xe^+ in the single scan spectra because the signal intensity is low. This type of data typically requires between 100 and 1000 averaged scans for good S/N.

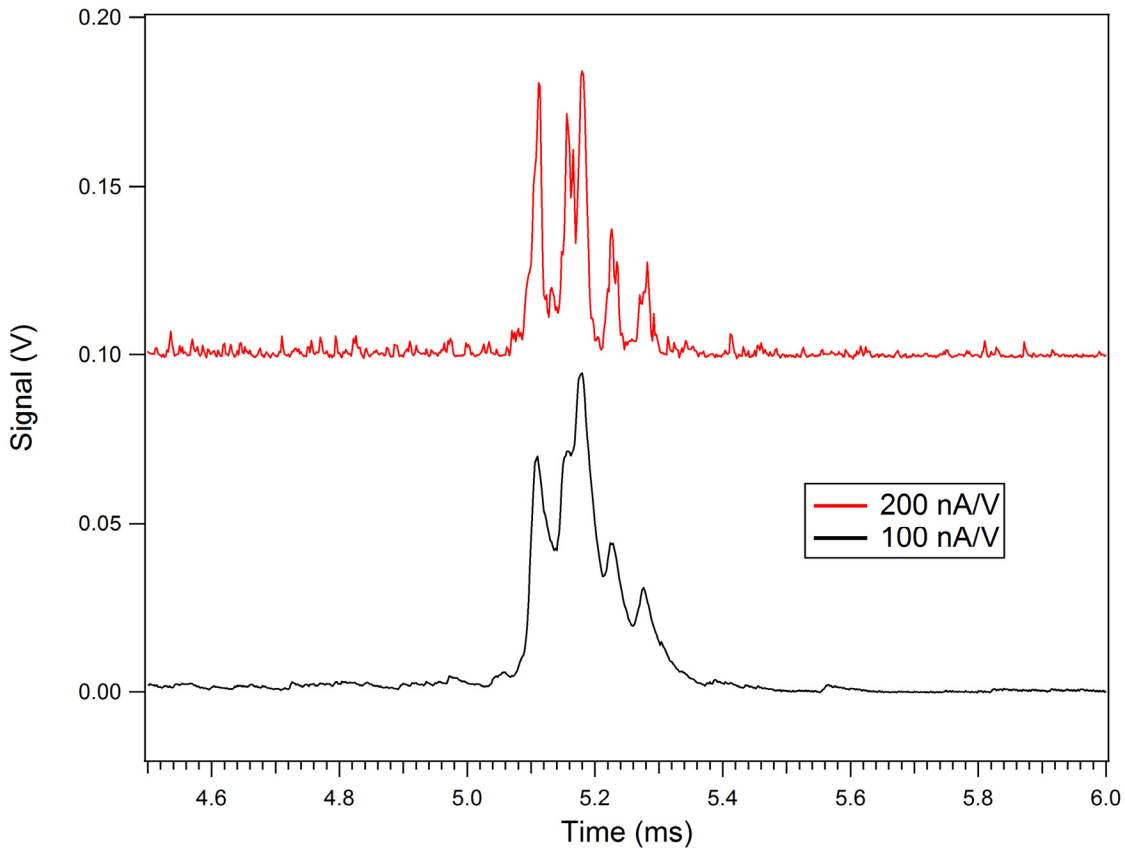

Figure 3.24: Increasing the current preamplifier gain above 200 nA/V causes a significant decrease in bandwidth. The spectrum recorded at 100 nA/V has an artificially low resolution and distorted isotope abundances due to the bandwidth change.

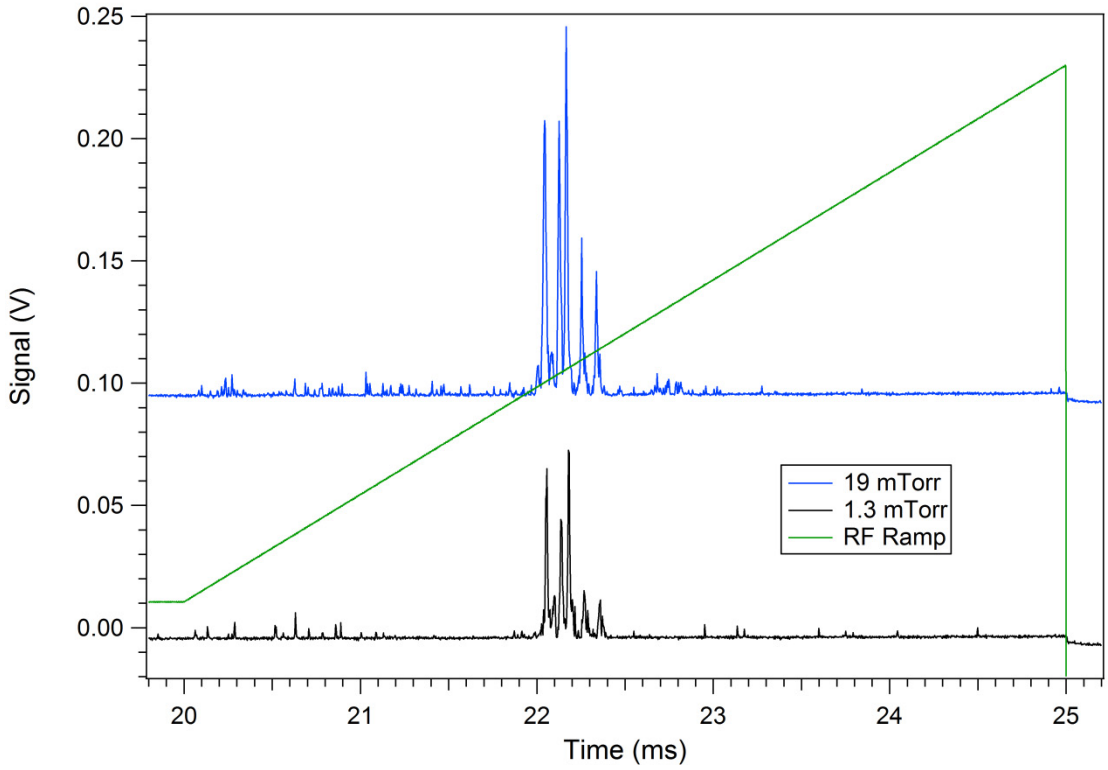

Figure 3.25: Increasing helium buffer gas pressure from 1.3 to 19 mTorr caused an increase in signal intensity and resolution.

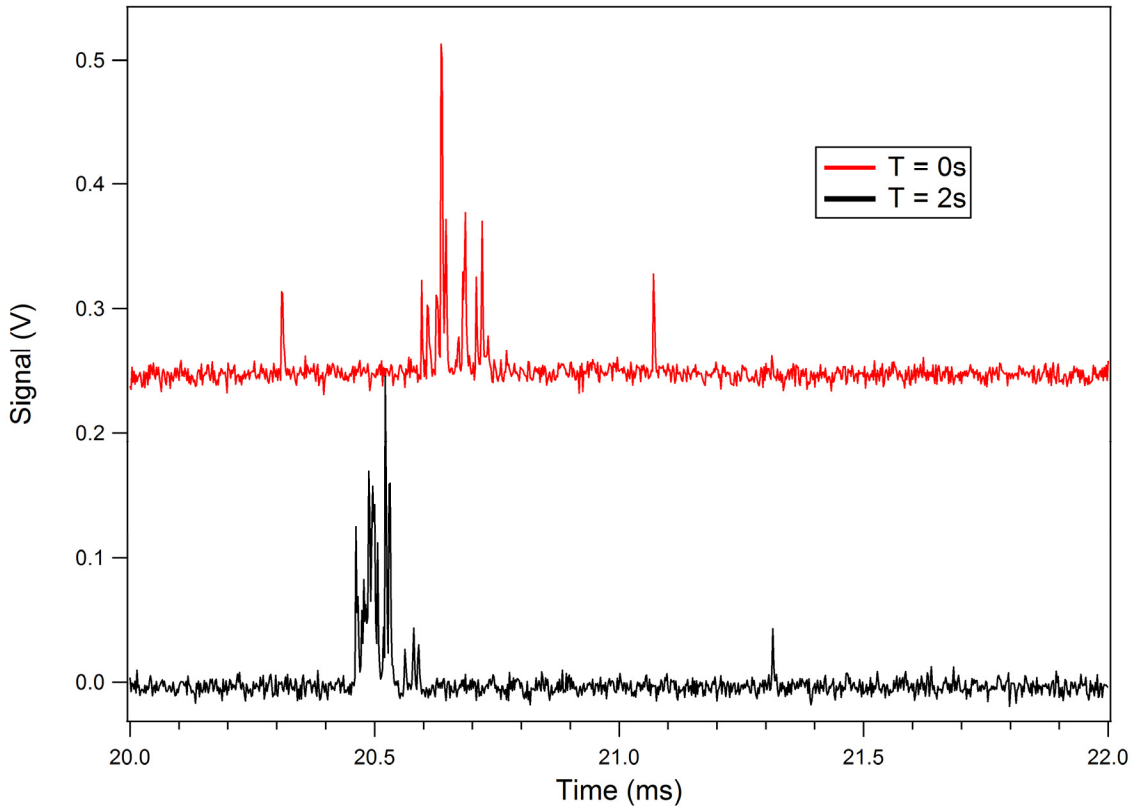

Figure 3.26: Single scan spectra recorded two seconds apart. A severe RF amplitude instability resulted in the ions constantly moving back and forth in the ramp.

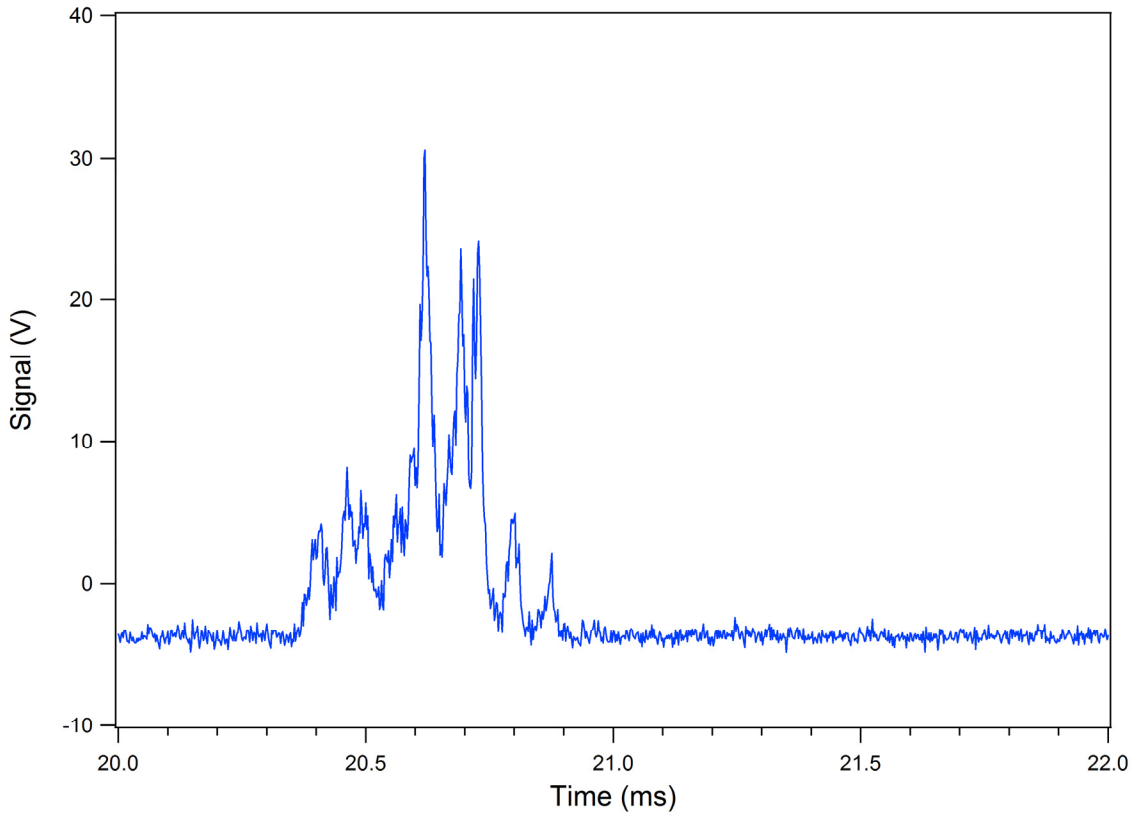

Figure 3.27: Averaged data with severe RF amplitude instability shows higher noise and decreased resolution due to the superposition of two shifted spectra.

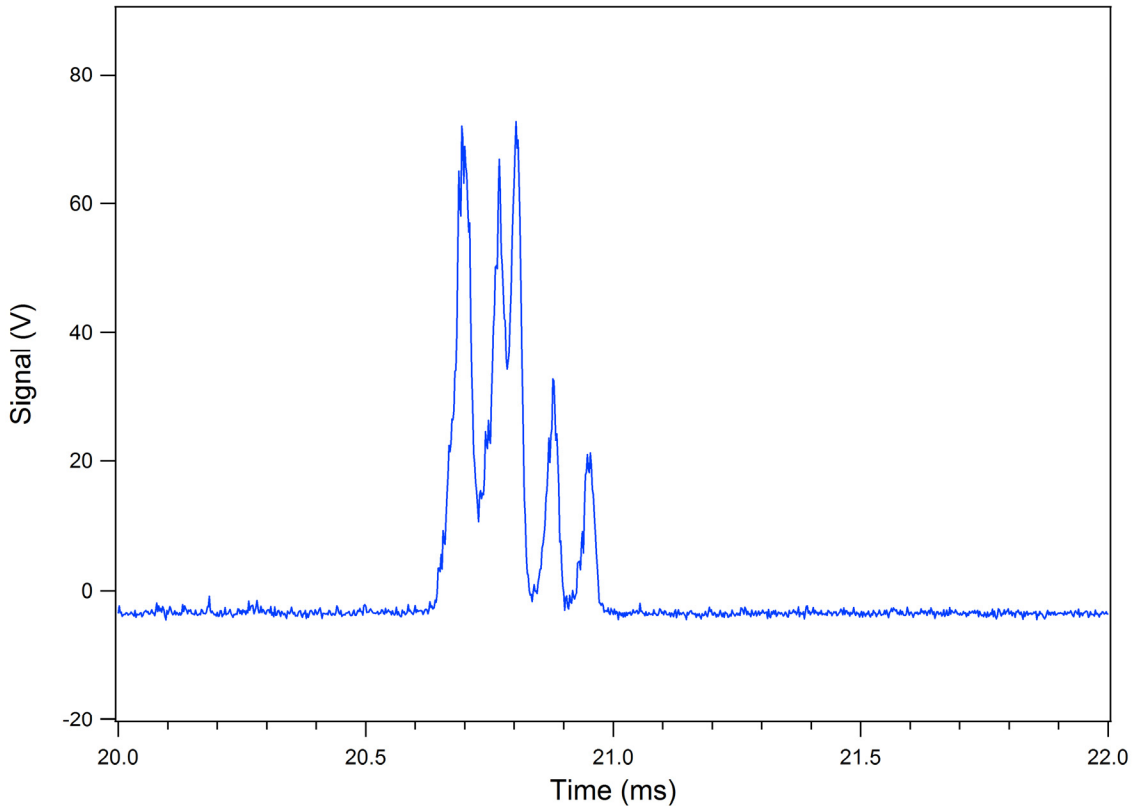

Figure 3.28: Averaged data after eliminating the RF amplitude instability by re-tuning the amplifier. These spectra show increased resolution, signal intensity, and S/N.

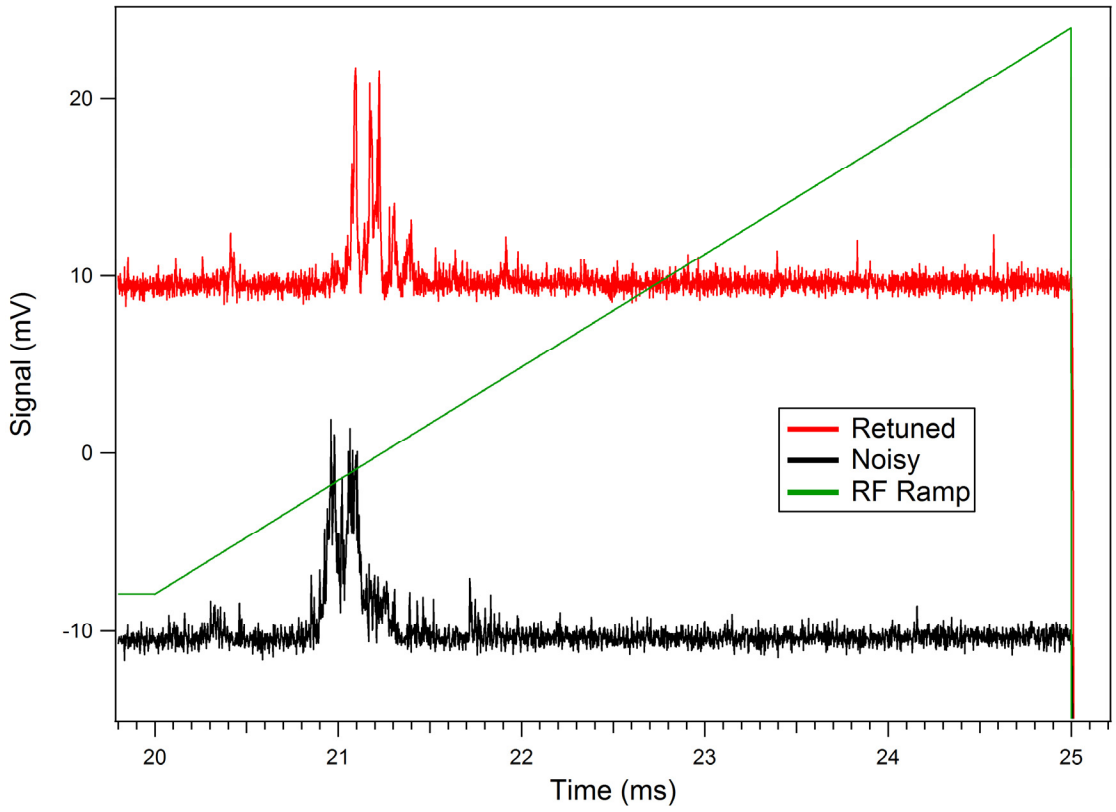

Figure 3.29: Averaged data with a small RF amplitude instability shows an increase in resolution after re-tuning the amplifier.

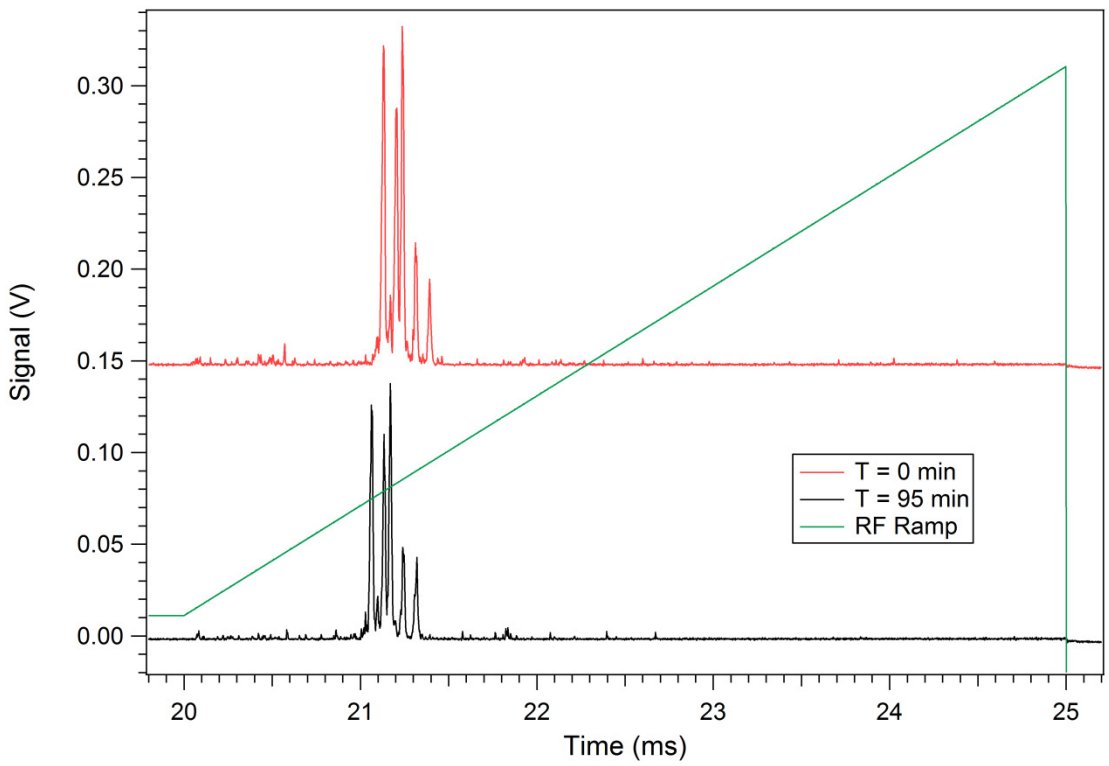

Figure 3.30: Signal drift between two spectra taken 95 minutes apart. This is caused by a long-term RF amplitude instability but doesn't negatively impact instrument resolution since the amplitude change didn't occur while the data is averaging.

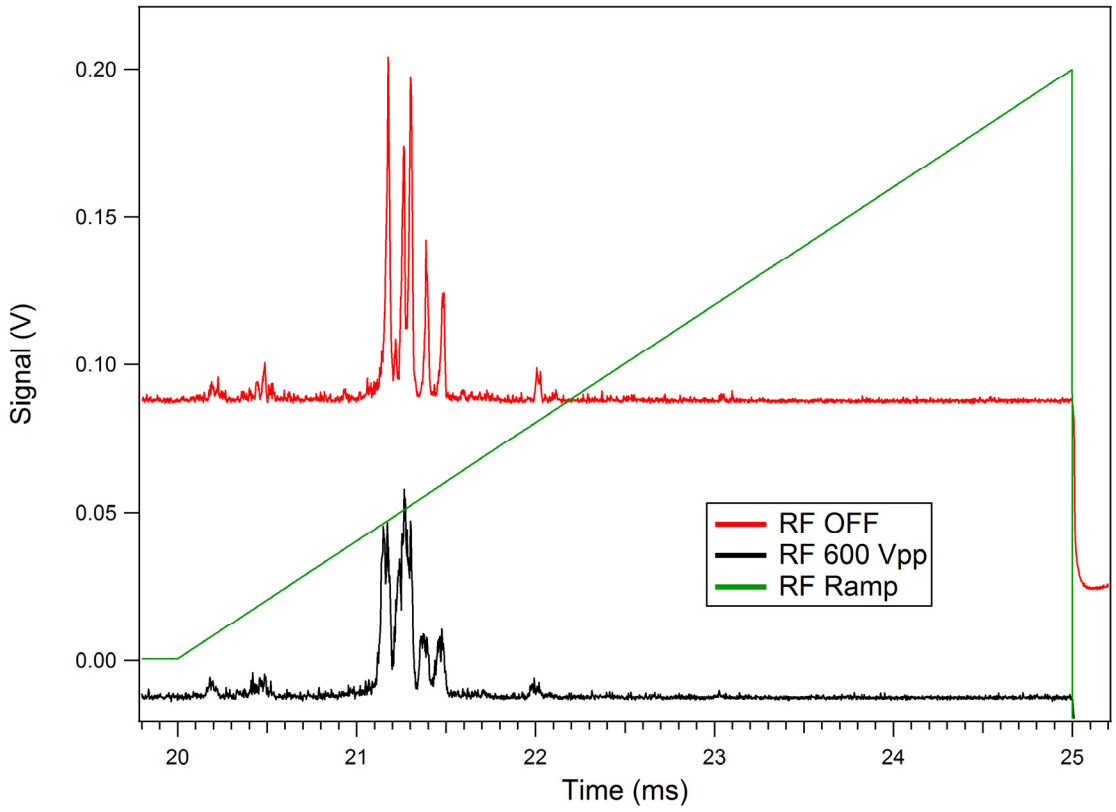

Figure 3.31: Spectra showing a decrease in resolution and signal intensity caused by crosstalk from an adjacent instrument's RF amplifier tuned to the same frequency.

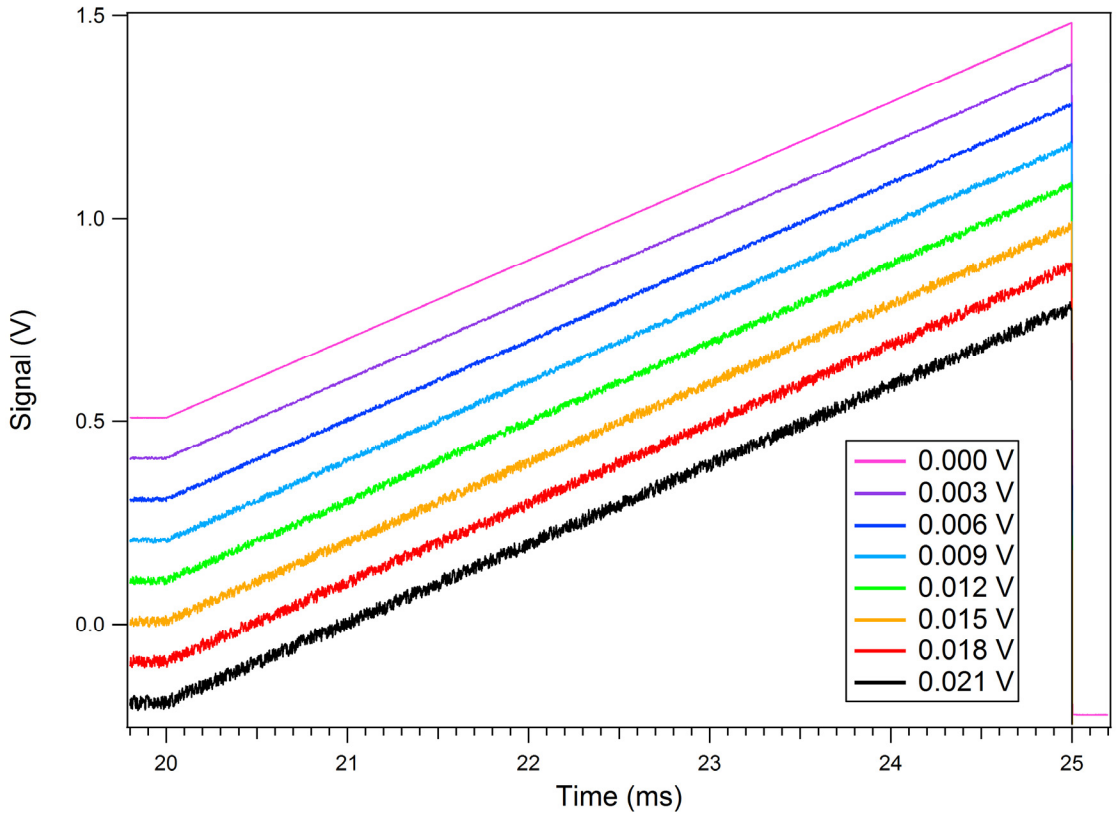

Figure 3.32: RF amplitude ramps with 0 to 21 ppth superimposed white noise.

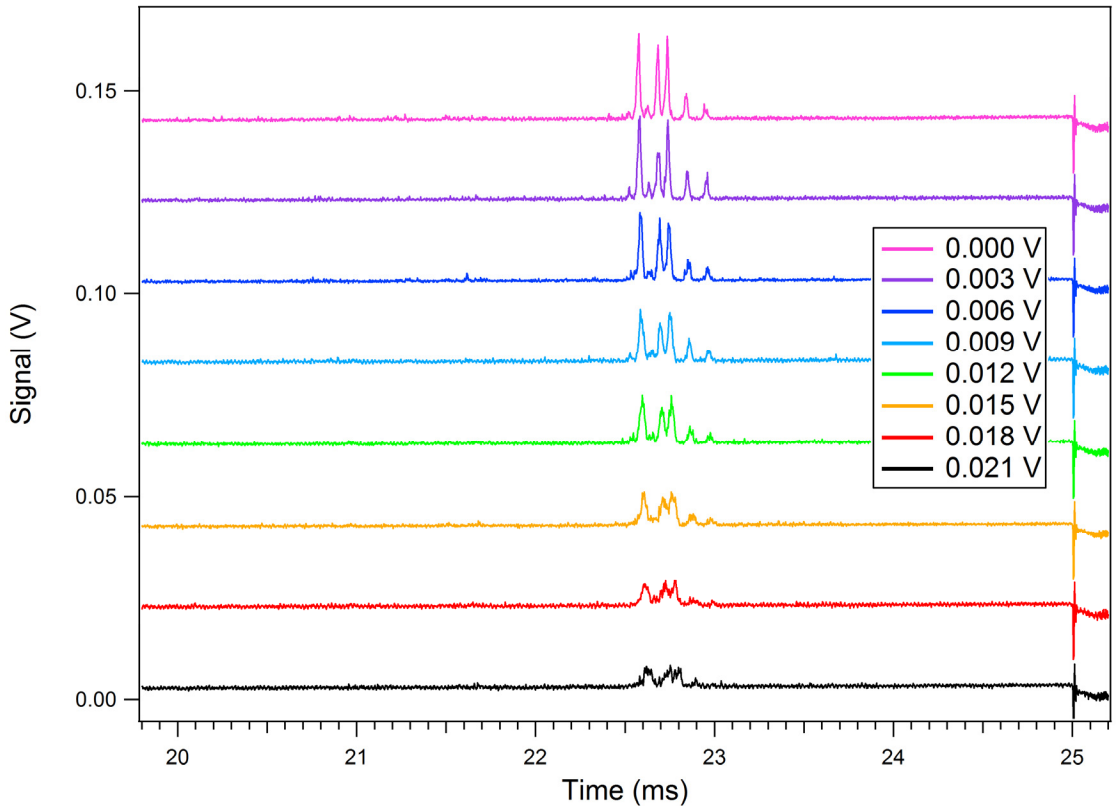

Figure 3.33: Spectra generated with noisy RF amplitude ramps. As the noise increases from 0 to 21 ppth, resolution and signal intensity decrease significantly.

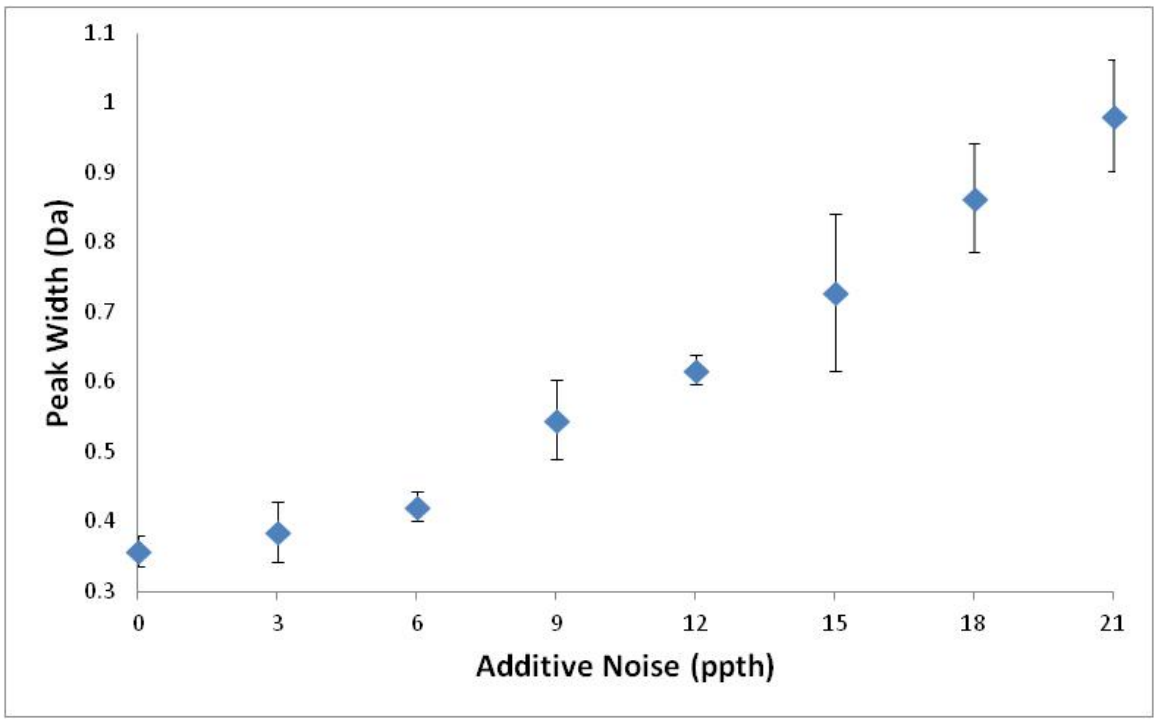

Figure 3.34: Quantitative effects of RF amplitude noise on peak width of spectra.

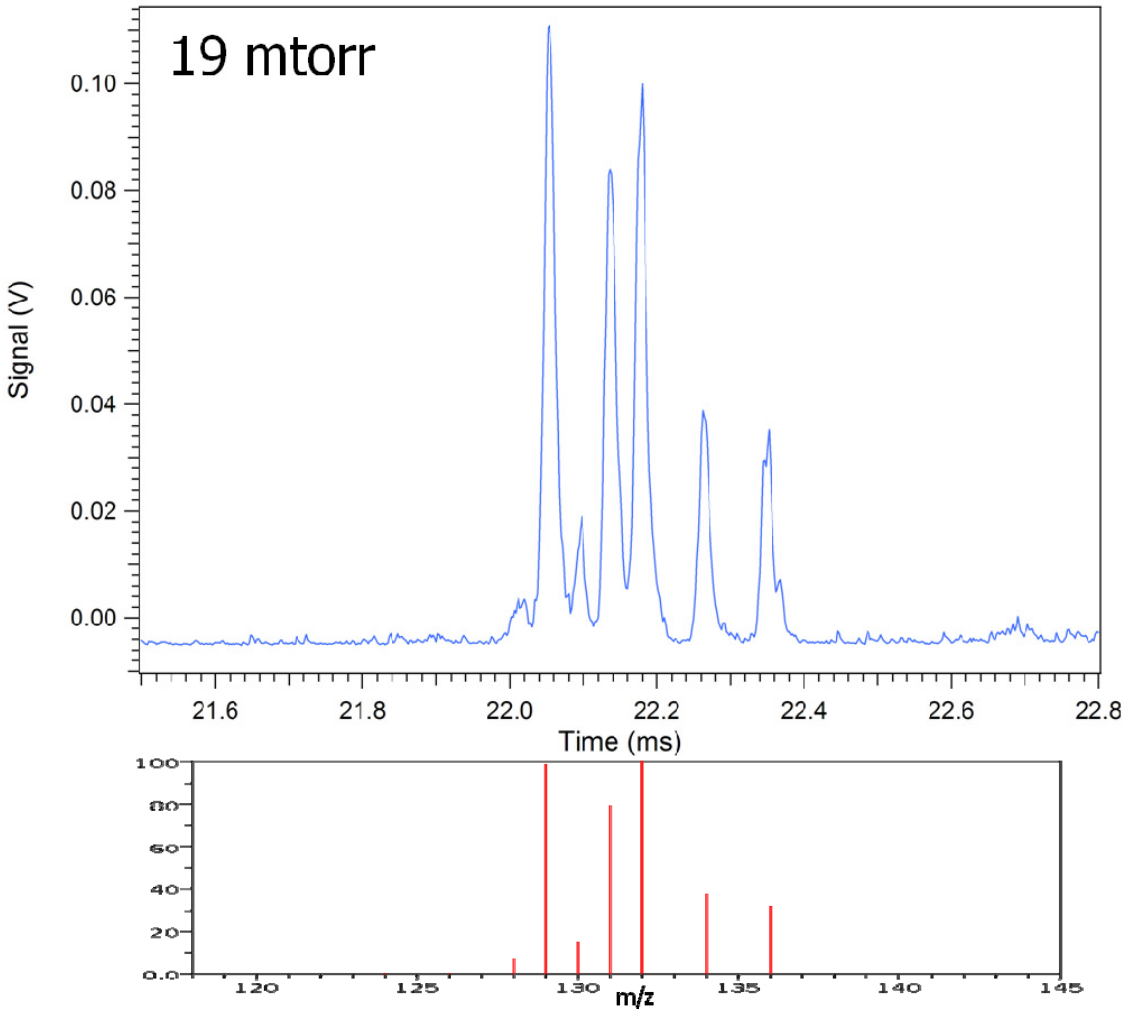

Figure 3.35: Representative mass spectrum of 7.3 x 10^{-6} torr xenon in 19 mTorr helium buffer gas compared to NIST standard. The concentration of xenon was 384 ppm relative to the helium buffer gas.

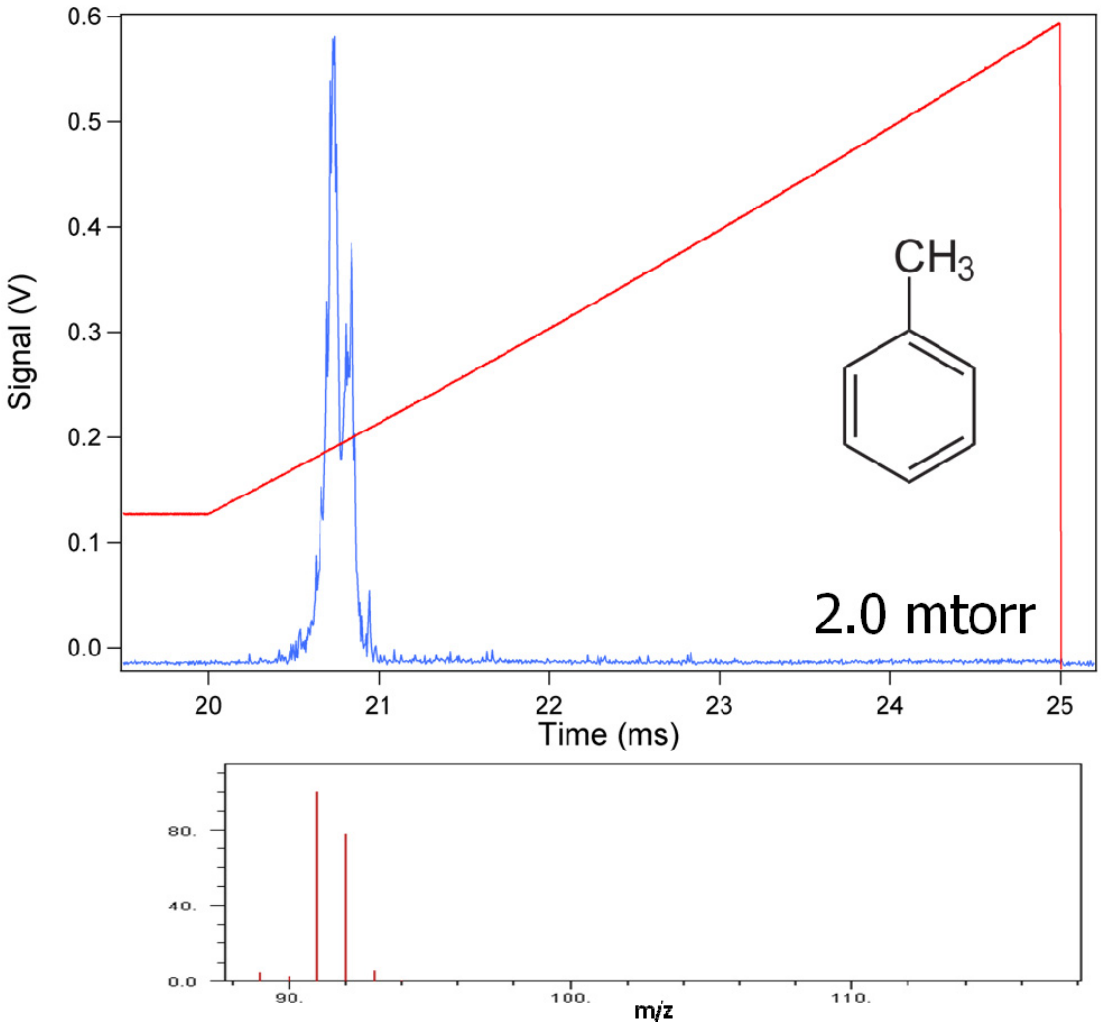

Figure 3.36: Representative mass spectrum of 8.0 x 10^{-6} torr toluene in 2 mTorr helium buffer gas compared to NIST standard. The concentration of toluene was 4.0 ppth relative to the helium buffer gas.

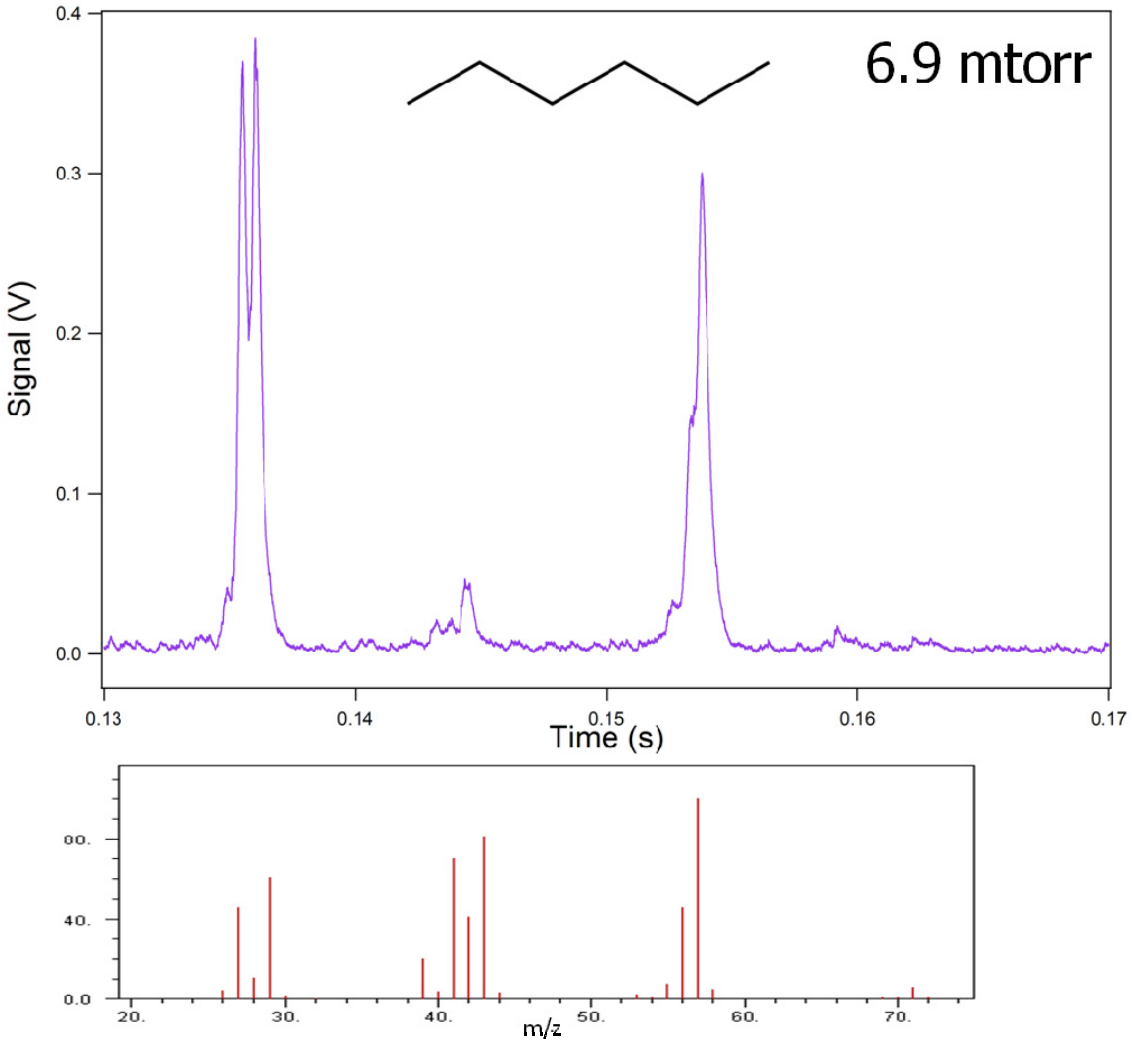

Figure 3.37: Representative mass spectrum of 9.2 x 10^{-6} torr hexane in 6.9 mTorr helium buffer gas compared to NIST standard. The concentration of hexane was 1.33 ppth relative to the helium buffer gas.

3.6 References

(1) Goeringer, D. E.; Whitten, W. B.; Ramsey, J. M.; McLuckey, S. A.; Glish, G. L., *Anal. Chem.* 1992, *64*, 1434-1439.

(2) Wu, G.; Cooks, R. G.; Ouyang, Z., *Int J Mass Spectrom* 2005, *241*, 119-132.

(3) March, R. E., *Mass Spectrom. Rev.* 2009, *28*, 961-989.

CHAPTER 4

HIGH-PRESSURE MS

4.1 Introduction

The goals of this chapter are to demonstrate mass analyzer operation at high buffer gas pressures and characterize CIT performance as a function of pressure. Previous low-pressure experiments with microscale CITs utilized a trap with radius r_0 = 500 μm and ≈3 mTorr of He buffer gas.[1-3] This trap configuration was used as a basis for these experiments since it should be capable of operating at buffer gas pressures significantly higher than the 1 mTorr levels typically used in r_0 = 1 cm commercial hyperbolic QITs. Experimental parameters were similar to those used for low-pressure experiments (Chapter 3) except where specified otherwise. For these experiments a differentially pumped CIT mass spectrometer (Chapter 2) with critical dimensions r_0 (radius) = 500 μm and z_0 (half-length) = 645 μm was used to explore MS instrument performance at previously unreported helium buffer gas pressures up to 1 torr. The results described here advance development of a high-pressure CIT mass analyzer for use in portable MS systems with smaller pumping systems and reduced SWaP.

4.2 Instrumental challenges

A number of experimental parameters needed to be optimized before successful high-pressure MS experiments were possible. Initial high-pressure MS experiments were disappointing because analyte signal intensity was found to decrease as a function of pressure. The data in Figure 4.1 show the changes in Xe^+ signal as the helium buffer gas

was increased from 13 mTorr to 83 mTorr. At the highest pressure the signal was barely discernible above the background. To enable high-pressure MS a number of parameters were addressed and investigated as discussed below.

4.2.1 RF electrical discharge

Early attempts at operating the CIT at high buffer gas pressures above 100 mTorr were limited by electrical breakdown near the drive RF pin connector (Figure 4.2). This breakdown occurred when the RF amplitude reached approximately 300 V resulting in a strong blue glow in the vicinity of the pin connector. It was impossible to perform experiments with this discharge occurring because the large amount of uncontrolled background ionization quickly overwhelmed any analytical signal by saturating the detector. Since the amplitude of the drive RF is critical for trap operation, it was possible to avoid the breakdown by covering sharp edges of the pin connector with heat shrink tubing. This effectively insulated the high electric fields from being able to discharge to ground.

4.2.2 EI source efficacy

While driving the EI source with a constant current, the applied voltage was observed to decrease as the helium buffer gas was increased. This indicated that the inherent resistance of the hot cathode was decreasing, most likely due to increased cooling at high buffer gas pressures. Since EI sources are not typically operated in the 100 mTorr regime, the efficacy of the EI source was a potential explanation for the observed signal loss. To offset these cooling effects the EI source was driven with a constant voltage power supply. At a given pressure, the temperature and resistance of the source will reach equilibrium causing the current to stabilize. As the pressure increases

and the source resistance decreases, the constant applied voltage drives more current through the source to increase the temperature and maintain emission current levels. This effect is illustrated in Figure 4.3 where a current preamplifier was used to measure emission current as a function of buffer gas pressure. The first region of the graph shows a relatively constant emission current while the source was being driven with a constant voltage. Eventually the power supply reached the current limit of the emitter and switched to constant current mode. This prevented the supply from driving the source harder and caused a noticeable emission current decrease for the last three pressure values. Therefore it is advantageous to operate the EI source in a constant voltage mode to help maintain the emission current at high pressures.

4.2.3 Axial RF amplitude increase

Since the axial RF frequency and amplitude are critical to instrument performance, these parameters are typically optimized immediately and remain unchanged throughout an experiment. Figure 4.4 shows an experiment where the axial RF parameters were optimized for operation at 12 mTorr. When the pressure was increased to 110 mTorr, two sets of Xe^+ peaks were observed. This spectrum was characteristic of a non-optimal axial RF amplitude because one population of ions resonantly ejected with good resolution while a second population ejected later with poor resolution in a 'grounded endcap' state as if no axial RF was applied. Simply increasing the axial RF amplitude from 300 to 500 mV_{pp} with no change in frequency caused the second ion population to resonantly eject and immediately merge with the first set of peaks. This resulted in a recognizable Xe^+ spectrum at 110 mTorr with good resolution

and S/N. This strategy of increasing the axial RF amplitude with pressure enabled the instrument to generate spectra at buffer gas pressures above 100 mTorr.

4.3 High-pressure MS

The differentially pumped CIT MS instrument described in Chapter 2 could maintain pressures below 1 mTorr for safe electron multiplier operation with the high-pressure inlet chamber at 1 torr. No issues related to electron multiplier ion feedback were observed during high-pressure experiments. Analyte gas pressures were chosen to be slightly above the high-pressure chamber's base pressure of 1.0e-5 torr. Helium buffer gas pressures were then set by changing the He mass flow controller setpoint until the desired total pressure was achieved. Helium gas flow rates of 1 and 34 sccm generated 38.6 and 983.5 mTorr respectively in the high-pressure chamber. To avoid overloading the electron multiplier during the ionization period it was only turned on during the mass scan. The custom HV pulsing power supply was able to bring the multiplier to a stable-on state in 3 ms by driving it from 0 V to -1600 V. Fast detector turn-on times are desirable to avoid limiting the instrument spectra acquisition rate. A disc emitter was chosen instead of a tungsten wire filament as an EI source to eliminate alignment issues between the EI source and CIT endcap. Early experiments using tungsten filament EI sources showed that signal intensity was a function of filament alignment with respect to the endcap hole as previously mentioned in Chapter 3. Electrode alignment pin holes helped to precisely and reproducibly align the CIT electrodes for optimum trap performance. CIT spacing values were empirically optimized for best trap performance by varying the electrode spacing from 125 μm to 500 μm using 125 μm polyimide spacers. The optimum signal intensity and resolution were

observed with a spacing value of 250 μm which corresponds to z_0 = 645 μm. The trap capacitance was 30 pF at 6 MHz which is in agreement with the calculated capacitance based on electrode area and spacing. A scan rate of 33,000 Da/s for these experiments produced < 1 *m/z* unit peak widths and strong signal intensities during a relatively short 5 ms mass scan. The mass range of a typical scan was ≈160 *m/z* units under these conditions. The custom RF amplification system generated the RF signal with better amplitude stability than commercially available amplifiers that were tested in the lab. Short term RF amplitude noise was measured with a spectrum analyzer to be ≈ 2 ppth under load conditions. This resulted in peak widths below 1 *m/z* unit in the acquired mass spectra. An RF frequency of 6.3 MHz was chosen due to RF amplifier bandwidth limitations at higher frequencies.

Representative spectra from a high-pressure MS experiment with 2.7e-5 torr Xe in He buffer gas pressures up to 983.5 mTorr are shown in Figure 4.5. These spectra were collected by scanning the RF amplitude from 175 to 375 $V_{0\text{-}p}$ while applying 4.23 MHz axial RF to resonantly eject the ions. The current preamplifier gain was set to 200 nA/V to provide enough amplification and sufficiently wide bandwidth to avoid broadening individual peaks. These spectra were averaged for 1000 consecutive scans to produce good S/N characteristics without any filtering or signal processing of the raw data. Analog control waveforms were written at a 500 kHz rate to generate a smooth RF amplitude ramp. Analog data acquisition rates of 500 kHz resulted in ≈20 points across a typical mass peak.

Peak width as a function of He pressure was quantitatively determined by performing a Gaussian fit on the five highest abundance Xe isotopes (*m/z* = 129, 131,

132, 134, and 136) and averaging them together at each pressure (Table 4.1). This average FWHM peak width as a function of He pressure is shown in Figure 4.6. Average peak widths for Xe^+ at 38.6 and 983.5 mTorr He were measured to be 0.40 and 0.49 *m/z*, respectively. The average peak width didn't increase significantly as a function of He pressure but a decrease in S/N was observed due to non-ideal EI source operation and trapping conditions at high pressure. The ratio of signal intensity between the spectra at 38.6 and 983.5 mTorr was 6.5:1. Spectra shown in Figure 4.5 were normalized to 1 for display purposes.

Previous theoretical work by Goeringer[4] and Xu[5] predict that peak width will increase linearly with the neutral buffer gas pressure above some optimum pressure for a given trap. This effect arises when collisions begin to dominate the trajectory of the ions and it becomes more difficult to control them with the electric fields inside the trap. Peak widths are broadened further by collisions with buffer gas molecules after the ions are scanned out of the trap towards the detector. To help offset these peak broadening effects, the axial RF amplitude was increased from 200 to 1800 mVpp to maintain strong resonance conditions as the pressure was increased. The differentially pumped chamber design also helped offset broadening due to collisions between the trap and detector by maintaining ≈1 mTorr pressures in the space between the endcap and detector. This coupled with the small distance between the trap and detector results in relatively few collisions after the ions exit the trap. Ionization time was also increased from 1 to 50 ms to help offset reduced electron flux inside the CIT caused by cooling of the relatively large disk emitter surface at high pressures. After optimization, the five most abundant Xe^+ isotopes are clearly visible at He buffer gas pressures up to 577.5 mTorr (Figure 4.5).

At 868.7 mTorr the *m/z* = 131 and 132 isotopes merge together resulting in four clearly visible peaks. The highest pressure spectrum at 983.5 mTorr is more difficult to distinguish due to decreased signal intensity but the Xe^+ isotope peaks remain visible. Performance at higher operating pressures should improve with increased drive RF frequency and decreased CIT size.

Electrical breakdown was avoided by covering sharp edges on the RF pin connectors with shrink wrap to shield the high electric fields. Discharge is unlikely to spontaneously occur inside the trap at these pressures and distances since the Paschen values are very small ($p*d \leq 0.025$ Torr*cm) and therefore far to the left of the Paschen curve minimum for He.

Recent experimental results by Song *et. al.* utilized a rectilinear ion trap (RIT) instrument to explore MS performance at elevated pressures.[6] They demonstrated full width half max (FWHM) peak widths of 2 *m/z* units at 50 mTorr of air buffer gas. Experimental exploration of high-pressure operation was limited by electrical discharge above these pressures. Theoretical models predicted FWHM peak widths of 9.5 *m/z* for the RIT operating with air buffer gas at 250 mTorr.[5] The RIT was expected to be capable of mass analysis at pressures of several hundred mTorr but with poor resolution.

The peak widths achieved here are approximately an order of magnitude lower than the 9.5 *m/z* FWHM peak widths predicted previously for a RIT instrument with air buffer gas at 250 mTorr[5]. This is possible due to the use of He buffer gas, a smaller trap size, increased RF frequency, and resonance ejection conditions.

4.4 Conclusions

The differentially pumped CIT instrument described collected mass spectra at high buffer gas pressures by maintaining a separate detection chamber below 1 mTorr for electron multiplier operation. Custom RF amplifiers, HV pulsing power supply, and LabVIEW instrument control software were developed to drive the RF, control waveforms, and data acquisition modules required for a custom built MS instrument.

The use of a r_0 = 500 μm CIT was successfully employed to generate mass spectra at previously unreported He buffer gas pressures up to 983.5 mTorr. CIT mass analyzers are inexpensive and easy to fabricate in single or batch quantities via conventional or micromachining methods. The electrodes used for these experiments were fabricated by wet chemical etching techniques in quantities of 20 per piece of 4 x 5" sheet metal. Alignment pin holes and removable RF connections simplified CIT mass analyzer construction. Due to the low manufacturing cost of an individual CIT, permanently bonding the electrodes with epoxy to prevent trap misalignment is feasible. This electrode design can also be easily modified to accommodate CIT arrays if larger signal intensities are desired. Single trap CIT electrodes were used for these high-pressure MS experiments because the differential pressure capability of the instrument will decrease with additional endcap holes between chambers. Therefore a pressure tolerant ion detector is required to take advantage of the CIT arrays.

In the high-pressure mass spectra shown here, peak widths remained relatively constant at pressures ranging from 38.6 to 983.5 mTorr. Although the peak width does increase slightly, it is much less than the order of magnitude peak width increase that would be expected over the range of pressures presented here. Increasing the axial RF

amplitude helped to maintain the performance by offsetting the effects of increasing pressure. Increasing the ionization time with pressure offset the decreasing electron flux due to emitter cooling and electron scattering at higher pressures.

The pressures described here are approximately three orders of magnitude higher than conventional ion trap operating pressures and should result in a significant reduction in SWaP for a portable MS instrument. These results demonstrate that significant increases to mass analyzer operational pressures can be made to improve MS portability while maintaining sufficient performance. Further increases to operational pressures should be possible with smaller traps, a high-pressure ionization source, and improvements in pressure tolerant detectors.

4.5 Tables and figures

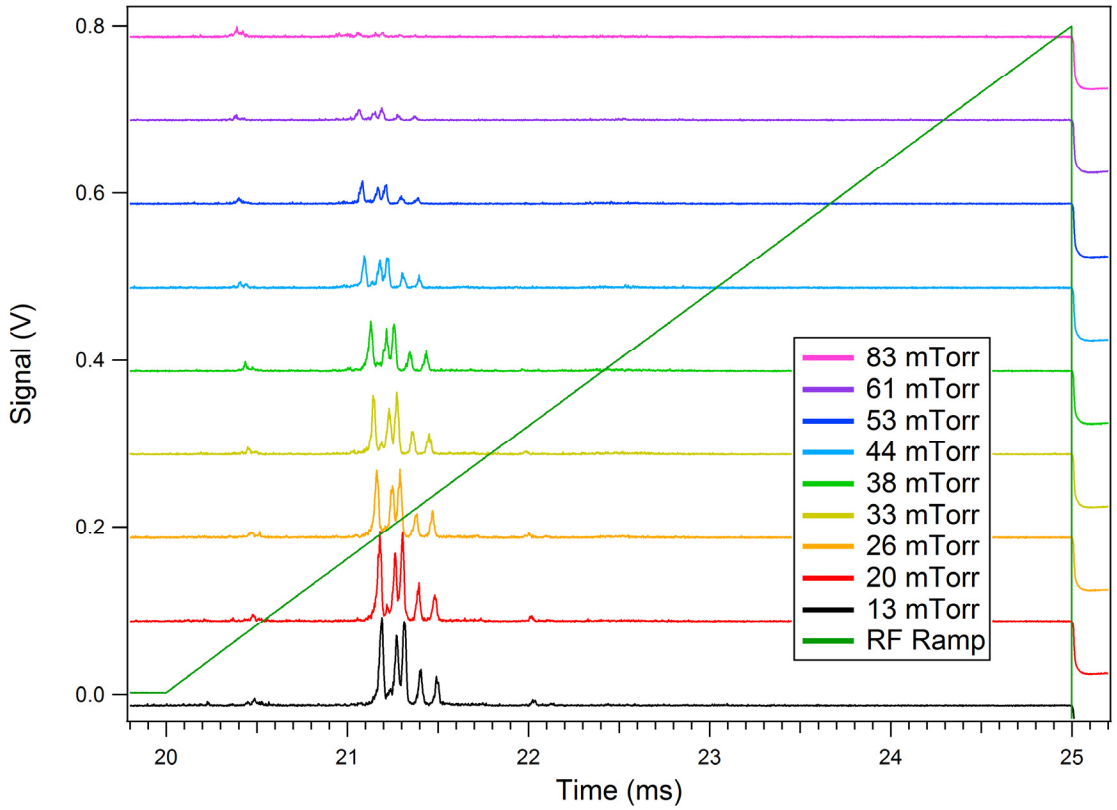

Figure 4.1: Spectra of Xe^+ acquired at He buffer gas pressures from 13 to 83 mTorr. The signal intensity decreases with increasing pressure when experimental parameters are not reoptimized.

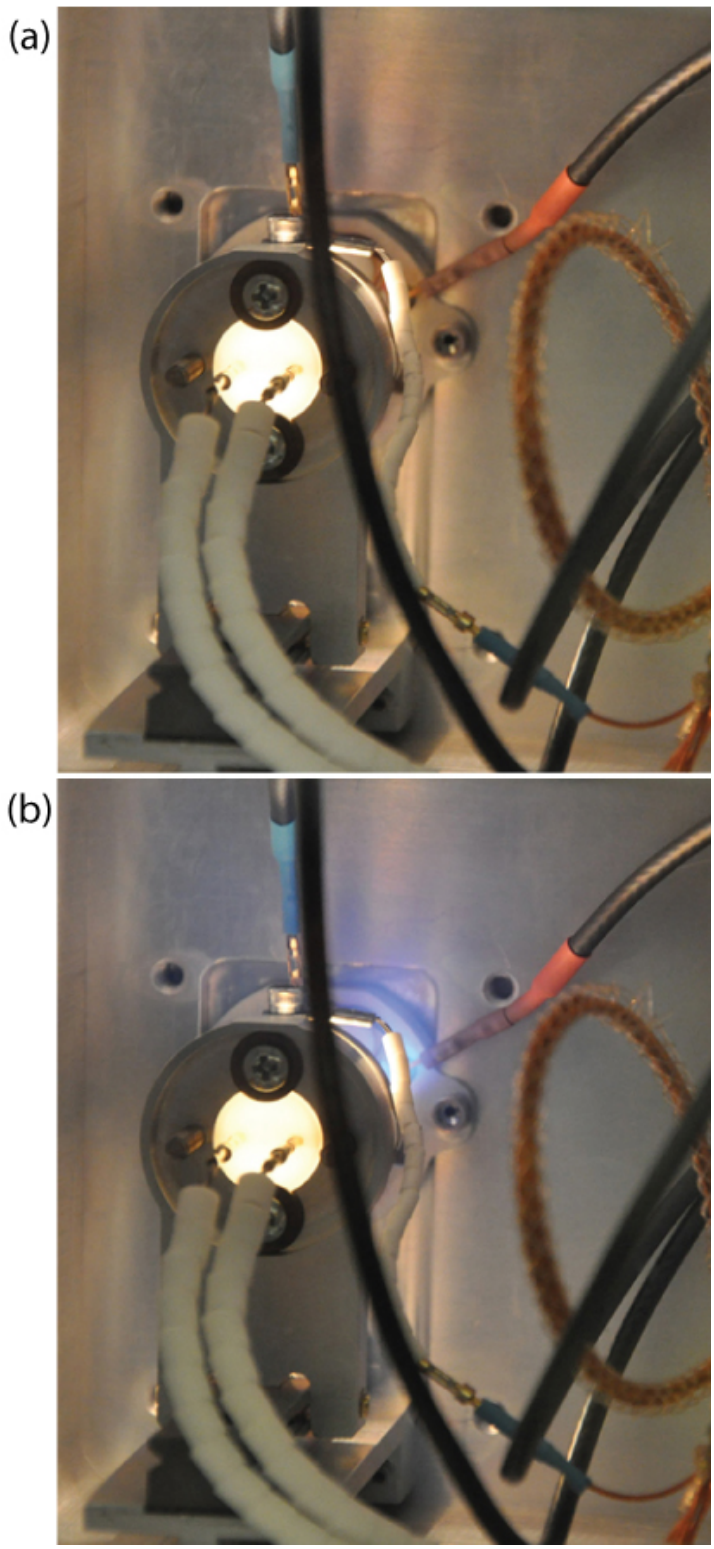

Figure 4.2: Images of the instrument operating at 86 mTorr with (a) RF turned off and (b) 700 Vpp RF applied to the CIT. The electrical discharge around the RF connection produces a bright blue light.

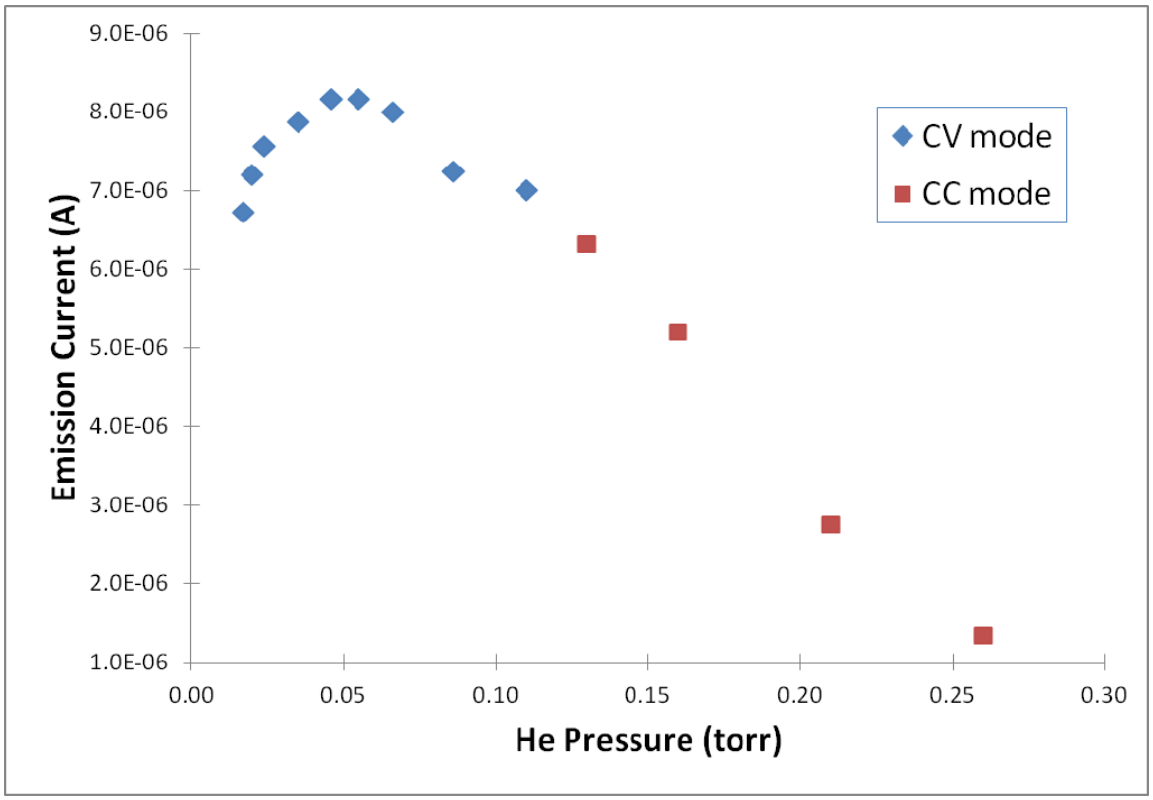

Figure 4.3: Emission current remained relatively constant as a function of the He pressure when driving the EI source with a constant voltage (CV) supply. When the supply switched to constant current (CC) mode, emission current decreased due to emitter cooling at high pressures.

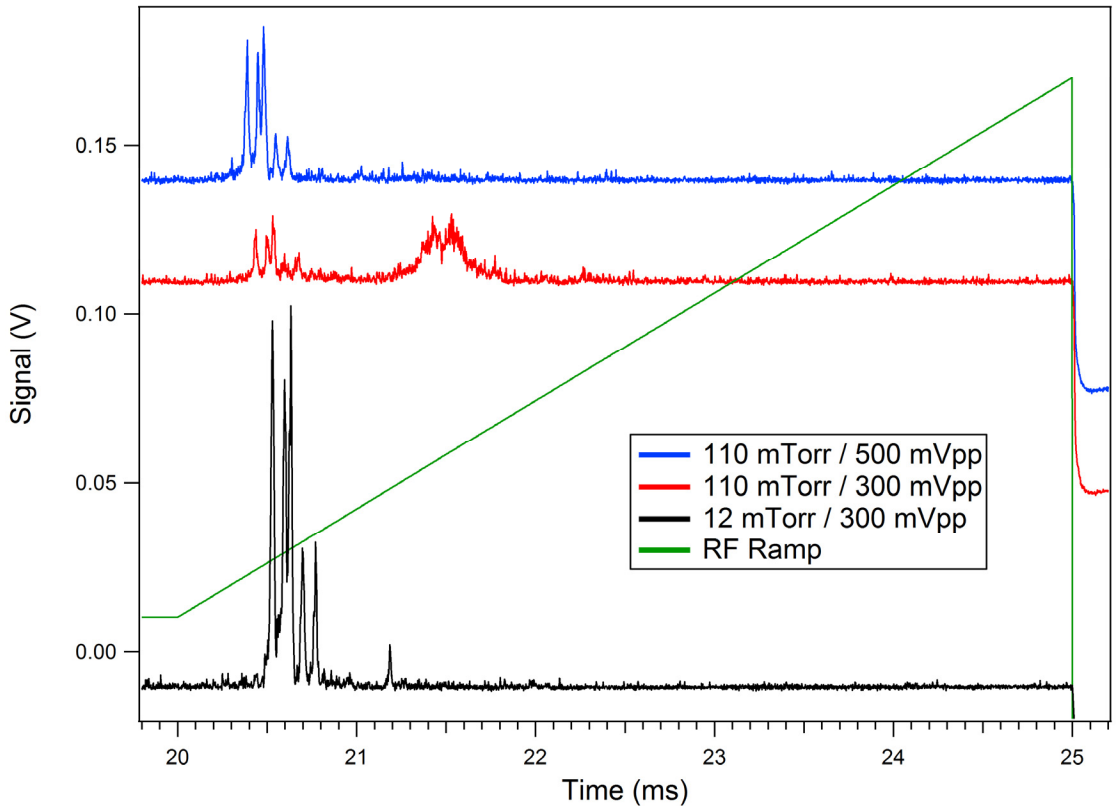

Figure 4.4: Axial RF amplitude was optimized for operation at 12 mTorr (black). When the pressure was increased to 110 mTorr, two sets of Xe^+ peaks were observed (red). This is characteristic of insufficient axial RF amplitude where some ions resonantly eject and others eject later in the non-resonant location. Increasing the axial RF amplitude to 500 mV_{pp} caused all ions to resonantly eject and resulted in improved MS performance at 110 mTorr (blue).

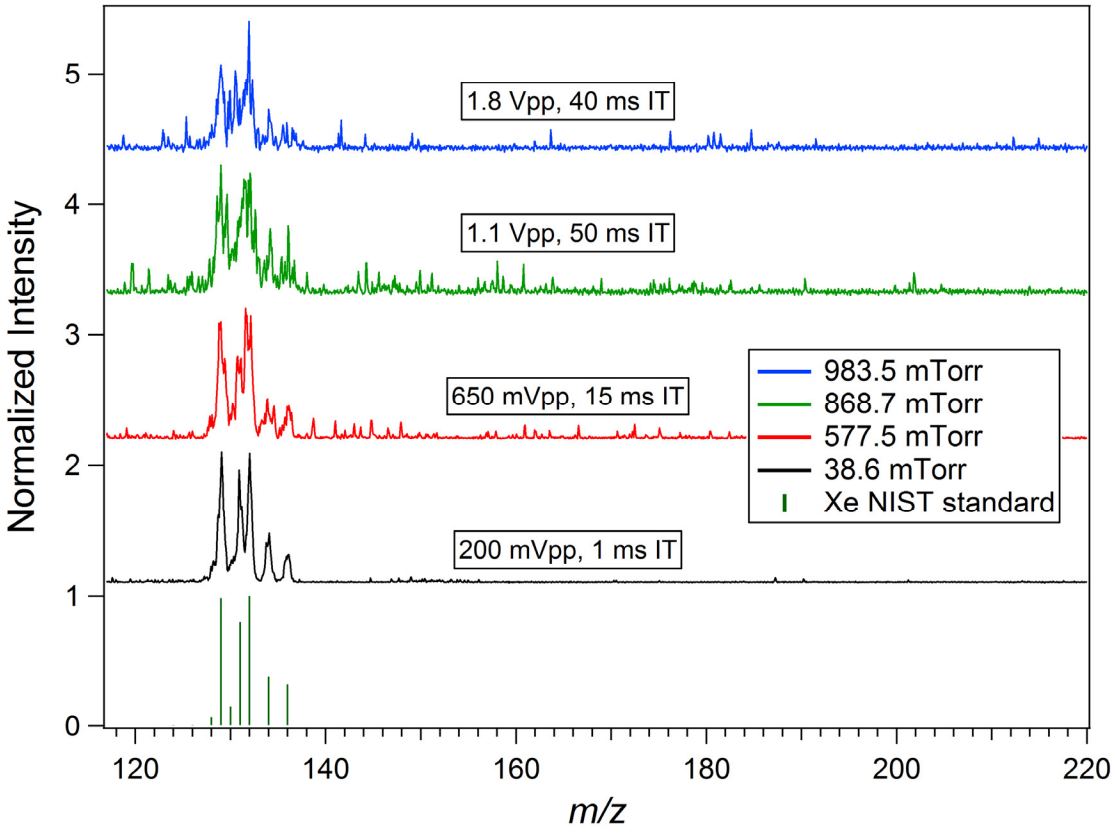

Figure 4.5: Xe^+ spectra taken with He buffer gas pressures from 38.6 to 983.5 mTorr. Peak widths remain relatively constant but there is a decrease in S/N due to non-ideal EI source operation and trapping conditions at very high pressures. Optimization of spectra required changing ionization time (IT) and axial RF peak-to- peak amplitude as indicated above for each corresponding He buffer gas pressure.

			FWHM (Th)						
Pressure (mTorr)	**Axial RF (mVpp)**	**IT (ms)**	**129**	**131**	**132**	**134**	**136**	**Avg**	**Std. Dev**
38.6	200	1	0.46	0.44	0.32	0.40	0.39	0.40	0.05
150.4	300	2	0.43	0.40	0.39	0.79	0.45	0.49	0.17
292.9	500	3	0.63	0.73	0.35	0.41	0.41	0.50	0.16
430.4	500	4	0.63	0.45	0.45	0.70	0.64	0.57	0.12
577.5	650	15	0.61	0.43	0.56	0.76	0.44	0.56	0.14
720.2	900	20	0.63	0.16	0.44	0.64	0.53	0.48	0.19
868.7	1100	50	0.78	0.54	0.56	0.47	0.39	0.55	0.14
983.5	1800	40	0.59	0.33	0.70	0.35	0.48	0.49	0.16

Table 4.1: High-pressure peak width analysis for Xe^+ *m/z* = 129, 131, 132, 134, and 136.

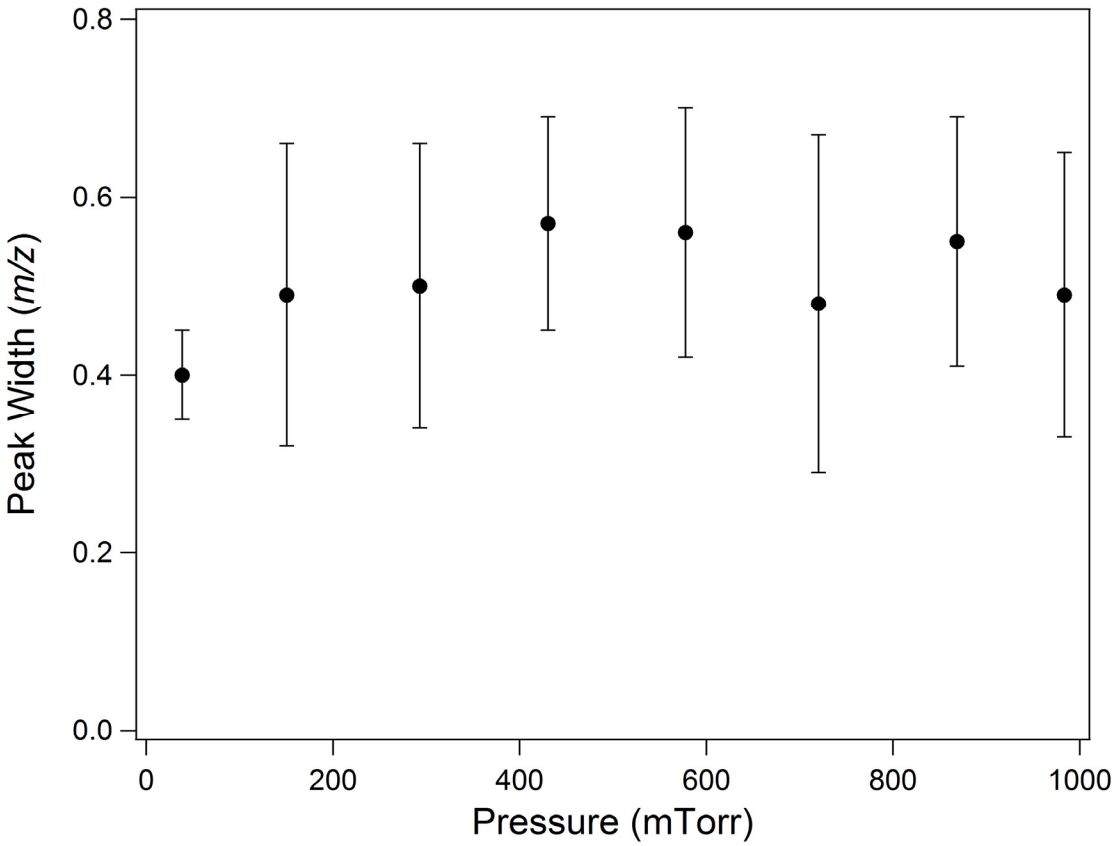

Figure 4.6: Effects of He buffer gas pressure on the FWHM peak width for the five most abundant Xe^+ isotopes (m/z = 129, 131, 132, 134, and 136) averaged together. Error bars show the peak width standard deviation at each pressure value.

4.6 References

(1) Moxom, J.; Reilly, P. T.; Whitten, W. B.; Ramsey, J. M., *Anal. Chem.* 2003, *75*, 3739-43.

(2) Moxom, J.; Reilly, P. T. A.; Whitten, W. B.; Ramsey, J. M., *Rapid Commun. Mass Spectrom.* 2002, *16*, 755-760.

(3) Moxom, J.; Reilly, P. T. A.; Whitten, W. B.; Ramsey, J. M., *Rapid Commun. Mass Spectrom.* 2004, *18*, 721-723.

(4) Goeringer, D. E.; Whitten, W. B.; Ramsey, J. M.; McLuckey, S. A.; Glish, G. L., *Anal. Chem.* 1992, *64*, 1434-1439.

(5) Xu, W.; Song, Q.; Smith, S. A.; Chappell, W. J.; Ouyang, Z., *J. Am. Soc. Mass Spectrom.* 2009, *20*, 2144-53.

(6) Song, Q.; Xu, W.; Smith, S. A.; Gao, L.; Chappell, W. J.; Cooks, R. G.; Ouyang, Z., *J. Mass Spectrom.* 2010, *45*, 26-34.

CHAPTER 5

HIGH-PRESSURE DETECTOR

5.1 Introduction

Previous high-pressure experiments with microscale CITs have demonstrated operation at pressures approaching 1 Torr using a trap with r_0 (radius) = 500 μm and z_0 (half-length) = 645 μm (Chapter 4). These experiments used an electron multiplier detector and a differentially pumped vacuum system to maintain a low-pressure region for safe detector operation. An ideal detector would be capable of operating at any pressure, which would further simplify the instrument to a single vacuum chamber.

The work presented here uses a second-generation, single-channel CTIA as a pressure tolerant ion detector for an isobaric microscale CIT instrument. The CTIA is fully differential with two inputs to reject input noise and two outputs that reject common mode noise by subtracting the outputs to generate the final signal. In this single vacuum chamber design, minimizing the distance that ions travel is important for reducing neutral gas collisions between the CIT and the detector at high pressures. Additional challenges to integrating this detector in a MS instrument include RF interference and biasing the detector for attracting positive ions. These results further advance the development of a high-pressure MS by demonstrating a pressure tolerant ion detector for use in portable instruments with smaller pumping systems and reduced SWaP.

5.2 Experimental

An isobaric MS instrument was built on a standard 6" Conflat (CF) flange for operation at high buffer gas pressures (Figure 5.1). This instrument did not require a second low-pressure chamber since the electron multiplier was replaced with a pressure tolerant CTIA detector. Custom mounting fixtures for the EI source, CIT, and CTIA detector were attached to two parallel threaded rods for alignment.

An array of 19 parallel CITs was used in these experiments to maximize signal intensity for the CTIA detector. The CIT array was constructed with a custom 790 μm thick copper ring electrode and two 250 μm thick beryllium copper endcap electrodes fabricated by wet chemical etching (Towne Technologies, Somerville NJ). Electrode spacing was set to 250 μm with polyimide washers (McMaster-Carr, Atlanta, GA) to create a CIT array where each trap had critical dimensions r_0 = 500 μm, z_0 = 645 μm.

5.3 Instrumental challenges

A number of challenges needed to be addressed before successful high-pressure MS experiments with the CTIA detector were possible. It was necessary to investigate and address the following issues to enable truly high-pressure MS in a single vacuum chamber.

5.3.1 RF interference

Working with high-frequency and high-voltage RF signals can cause interference issues when the RF appears in undesired places. The highly sensitive solid-state CTIA detector is more sensitive to this interference than electron multiplier detectors and therefore requires careful shielding for proper operation. Early unshielded experiments with the CTIA showed a large low-frequency noise component appearing when the drive

RF was activated. This resulted in large fluctuations on the CTIA outputs which made it nearly impossible to capture a small analytical signal. An electrical shielding box was designed to enclose the CTIA detector inside a grounded metal housing (Figure 5.2). Although a solid metal box would provide the best electrical shielding, there needs to be an opening for ions to pass through to the detector. To accommodate this, a hole with an integrated grid electrode was added on the front of the shield box. The grid allows ions to pass while still providing effective electrical shielding. This grid was isolated from the grounded shield box since it was desirable to apply a voltage for attracting ions. A bypass capacitor between the isolated grid and the box provided a low impedance path to ground for RF interference picked up on the grid electrode. This strategy for shielding the detector was used in all CTIA experiments shown here.

5.3.2 Floating the CTIA

Since ions eject from the CIT with relatively low energy, it is desirable for the ion detector to have a negative voltage to attract ions to the detector surface. The electron multiplier accomplishes this by applying a negative HV to the front of the detector. However, with ground referenced power supplies the CTIA detector operates with the Faraday cup electrode at ground potential. Therefore the ions need to traverse a field-free region between the trap and the CTIA to be detected. This results in fewer ions striking the detector and consequently a decrease in signal intensity. Figure 5.3 demonstrates this effect with a Xe^+ signal intensity that decreases as the CTIA bias voltage is decreased toward 0 V. At high pressures the effect is more severe because ions undergo multiple collisions in this field-free region and are more easily lost. A relatively simple solution to this problem is to float the CTIA detector to apply a negative potential to the Faraday cup

electrode. This creates an electric field between the trap and detector to attract ions and improve signal strength. Although floating the detector is easily accomplished, special considerations must be made to properly interface to the floating circuit.

The first issue is resetting the floating detector to begin the next mass scan. To accomplish this, a ground referenced TTL pulse was converted to a floating pulse using a pulse isolation circuit based on the H11N1 logic optocoupler. The output of this circuit is a 5 V pulse referenced to the float voltage. The second issue is that both detector outputs are referenced to the float voltage and cannot be directly connected to the ground referenced DAQ system. Therefore it was necessary to design a signal isolation circuit based on the HCNR201 analog optocoupler to remove the bias voltage and ground reference both detector outputs for digitization.

5.3.3 Detector response time

The first generation signal isolation circuit based on the HCNR201 analog optocoupler had a bandwidth of 10 kHz which is too low to effectively pass higher frequency components of the detector output. With this limitation in mind, the first generation isolation circuit was sufficient for all early experiments with the CTIA detector since a considerable amount of development was required before ions were observed. For comparison purposes, Figure 5.4 shows the typical time response of the electron multiplier during an experiment where the scan rate was varied. When the same experiment was performed with the CTIA detector and first generation isolation circuitry, there is a clear loss in resolution due to the decreased time response of the isolation circuitry (Figure 5.5). To improve this slow response time, a second generation signal isolation circuit based on the AD629 HV difference amplifier was later developed. The

500 kHz bandwidth of this second generation isolation circuit was a significant improvement over the first generation design and made it possible to resolve individual mass peaks. In addition, this circuit is less complex and automatically subtracts the two detector outputs so the DAQ system is simplified to a single analog input. This second generation isolation circuit was used for all high-pressure MS experiments using the CTIA detector.

5.3.4 Signal processing

The CTIA is an integrating style detector so it is necessary to perform a mathematical derivative to generate the final mass spectrum. Since the data is recorded at high sampling rates, a small amount of read noise between two consecutive points is amplified by the derivation process resulting in a mass spectrum with much lower S/N than the original integrated signal. Therefore it is important to perform some signal processing to remove this unwanted noise. Figure 5.6 compares a representative integrated Xe^+ spectrum at 260 mTorr, the resulting numerical derivative, and the results of several signal processing algorithms applied to the derivative. The various algorithms produced similar beneficial results, with the exception of the wavelet deconvolution algorithm that decreased baseline noise significantly. However, a simple low-pass filtering algorithm was used for subsequent CTIA data processing because it produced satisfactory and predictable results with minimal complexity.

5.4 High-pressure MS with CTIA

The isobaric CIT MS instrument described performed MS at pressures up to 867 mTorr with no issues related to the CTIA detector. To achieve these pressures, the turbo pump drive frequency was reduced from 1250 to 500 Hz with further reduced gas

conductance using a manual gate valve between the chamber and pump. Analyte gas pressures were then chosen to be slightly above the base pressure of the vacuum chamber, 5.9 x 10^{-5} Torr, to allow for measurement. Helium buffer gas pressures were set by changing the He mass flow controller setpoint until the desired total pressure was achieved. Helium gas flow rates of 7 and 35 sccm generated 133 and 867 mTorr in the chamber, respectively.

A disc emitter was chosen as an EI source to eliminate alignment issues between the source and CIT endcap. This prevented signal intensity from varying with small emitter alignment errors. Using a thermionic electron source was feasible at these pressures due to the inert buffer gas atmosphere. Yttria coated emitters were chosen for further resistance to oxidation. The custom HV pulsing power supply was able to control the electron beam by driving the gate electrode from 0 V to -150 V at the end of the ionization time.

CIT spacing values were previously optimized for best trap performance by varying the electrode spacing from 125 μm to 500 μm using 125 μm polyimide washers (Chapter 4). The optimum signal intensity and resolution were observed with a spacing value of 250 μm, which corresponds to z_0 = 645 μm. Electrode alignment pin holes helped to precisely and reproducibly align the CIT electrodes for optimum trap performance. The trap capacitance was measured to be approximately 30 pF at 6.000 MHz, which is in agreement with the calculated capacitance based on electrode area and spacing. A scan rate of 28,500 Da/s for these experiments resulted in ~1 Da peak widths and a mass range of ~140 Da during the 5 ms mass scan.

The electrode design previously demonstrated in a single CIT configuration (Chapter 4) was modified to produce a 19 hole CIT array for maximizing signal intensity in these experiments. It was possible to use a CIT array for these high-pressure MS experiments because the endcap electrode did not need to function as a conductance-limiting orifice as with a differentially pumped high-pressure instrument.

Electrical discharge could be a limiting factor in a high pressure MS instrument due to the high voltage and pressure present in the chamber. However, this discharge is unlikely to spontaneously occur inside the trap at these pressures and distances since the Paschen values are very small ($p*d \leq 0.025$ Torr*cm) and therefore far to the left of the Paschen curve minimum for He gas. Induced electrical breakdown was avoided by focusing electrons from the EI source to prevent them from reaching areas with high electric fields (i.e. near pin connectors).

The custom RF amplification system was able to generate the necessary RF signal with better amplitude stability than commercially available amplifiers. Short term RF amplitude noise was measured with a spectrum analyzer to be ~1 ppth under load conditions. This is sufficiently low noise to avoid limiting the instrument resolution due to RF amplitude instability. A RF frequency of 5.9 MHz was chosen due to RF amplifier bandwidth limitations at higher frequencies.

The CTIA detector was able to integrate both electrons from the EI source and positive ions from the CIT. The detector operates by collecting incoming charges at the Faraday cup electrode and storing them on the feedback capacitor. This results in an integrating style detector where the output voltage is proportional to the number of collected charges and inversely proportional to the feedback capacitance. Common mode

noise is picked up by a second reference input and the CTIA differentially amplifies the input signal and produces two identical but inverted outputs. The differential output can further reduce noise picked up after the amplifier and double the resulting signal intensity by subtracting the outputs before digitization. The only limitation for this detector at high pressures is physically transporting the charged particles to the surface of the Faraday cup to deposit the charge. To help attract electrons or ions to the Faraday cup electrode, the detector was oppositely biased to set up appropriate electric fields between the CIT and detector. To successfully interface to the biased detector, a bias voltage was added to the detector's TTL reset pulse using a pulse isolator circuit. The bias voltage was removed from the output signal by subtracting the differential outputs using a HV difference amplifier. To avoid saturating the detector during ionization it was only activated during the mass scan. High gain mode was utilized in these experiments to maximize signal intensity and therefore S/N.

Gated electrons from the EI source were used as test charges to verify the CTIA detector functionality (Figure 5.7). When electrons from the EI source pass through the gate electrode, the detector integrates negative charges and produces a constant negative slope. When electrons are subsequently gated off, the integrated signal flattens out with a small positive slope due to dark current integration. Taking the numerical derivative of the integrated signal and low-pass (LP) filtering with a 1 kHz cutoff reproduces the square wave used to generate the four pulses of electrons.

Representative spectra from a high-pressure MS experiment with 8.7×10^{-5} Torr Xe in He buffer gas pressures up to 867 mTorr are shown in Figure 5.8. These spectra were collected by scanning the RF amplitude from 160 to 360 $V_{0\text{-}p}$ while applying 3.95

MHz axial RF to resonantly eject the ions. Analog to digital data acquisition rates of 500 kHz were used to accurately record raw mass spectra by sampling ~30 points across a typical mass peak. These spectra were averaged for 1000 consecutive scans to improve S/N and processed offline with a digital 40 kHz low-pass filter to produce the final mass spectra. Attempts to obtain higher-pressure spectra were limited by the decreasing EI source efficacy and the sensitivity of the CTIA detector. An alternative EI source design that is better able to tolerate high pressures would increase the signal intensity and help to overcome these limitations.

Peak width as a function of He pressure was quantitatively determined by performing a Gaussian fit on the five highest abundance Xe isotopes: m/z = 129, 131, 132, 134, and 136 (Table 5.1). Average FWHM peak width as a function of He pressure is shown in Figure 5.9. Average peak widths for Xe^+ at 133 and 867 mTorr He were 0.84 and 1.03 Da, respectively. This is similar to a previously reported trend where the average peak width didn't increase significantly as a function of He pressure up to 1 Torr (Chapter 4). However, a decrease in S/N was observed due to reduced electron emission and energy at high buffer gas pressures. The ratio of signal intensity between the spectra at 133 and 867 mTorr was 3.2:1. Spectra shown here were normalized to 1 for display purposes.

Previous theoretical work by Goeringer[49] and Xu[20] predict that peak widths will increase linearly with the neutral buffer gas pressure above some optimum pressure. This effect arises when collisions begin to dominate the trajectory of the ions and it becomes more difficult to control them with the electric fields inside the trap. Peak widths are further broadened by collisions with buffer gas molecules after the ions are ejected out of

the trap toward the detector. To help offset these peak-broadening effects, the axial RF amplitude was increased from 600 to 1500 mV_{pp} to maintain strong resonance conditions as the pressure was increased. It was also important to position the CTIA detector close to the CIT to minimize peak broadening due to collisions between the endcap and detector. Ionization time was increased from 15 to 75 ms to help offset reduced electron flux inside the CIT caused by cooling of the relatively large disk emitter surface at higher pressures. Emitter bias voltage was increased from -70 to -120 V to offset the effects of electron scattering and energy loss at high pressures. With increased drive RF frequency and decreased CIT size even higher pressure instrument operation should be possible.

The peak widths demonstrated here are approximately a factor of two larger than previous results with a dual chamber instrument and an electron multiplier detector (Chapter 4). However, these results show similar behavior where peak width does not increase significantly with pressure up to 1 Torr. These experimental results are much better than the 9.5 Da FWHM peak widths predicted previously for a RIT instrument with air buffer gas at 250 mTorr[20]. This is possibly due to several factors, including the use of He buffer gas, a smaller trap size, reduced ion travel distances, increased RF frequency, and resonance ejection conditions.

5.5 Conclusions

The isobaric CIT instrument described here performed MS at buffer gas pressures up to 867 mTorr using a solid-state CTIA detector. Custom RF amplifiers, HV pulsing power supply, and LabVIEW instrument control software were used to drive the RF, ionization source, control waveforms, and data acquisition modules required for the high-pressure MS instrument. The second generation CTIA detector originally developed for

ion mobility spectrometry was successfully utilized in a high-pressure CIT MS instrument for the first time. The CTIA demonstrated detection of positive and negative charges at high pressure without suffering increased noise or electrical breakdown issues. Special considerations for the detector included construction of a shielded enclosure to reduce drive RF interference and custom circuitry to operate the detector in a biased configuration to attract charges. Solid-state detectors like the CTIA are ideal for portable MS instruments due to their low voltage and power consumption requirements. They could be produced quickly and inexpensively using standard silicon IC and printed circuit board manufacturing technology.

Mass spectra at He buffer gas pressures up to 867 mTorr were successfully generated using a r_0 = 500 μm CIT array. CITs are inexpensive and easy to fabricate mass analyzers that are amenable to batch fabrication via conventional or micromachining methods. The electrodes used for these experiments were fabricated by wet chemical etching techniques in quantities of 20 per 4" x 5" piece of sheet metal. Due to the low cost of an individual CIT array, the electrodes used for these experiments were permanently bonded with epoxy to prevent changes to trap alignment.

In the high-pressure mass spectra shown here, peak widths remained relatively constant at pressures ranging from 133 to 867 mTorr. Increasing the axial RF amplitude helped to counteract the effects of increased collisions at high pressures. Increasing the ionization time and emitter bias with pressure helped to offset the decreasing electron flux due to emitter cooling and electron scattering at higher pressures.

The pressures described here are similar to those previously demonstrated with a CIT MS but are more than an order of magnitude higher than previously demonstrated

with MS ion detectors. Ion detectors capable of operating at high pressures will eliminate the need for a low-pressure detection chamber and therefore result in a reduction in SWaP for a portable MS instrument. These results demonstrate that significant increases to mass analyzer and ion detector operational pressures can be made to improve MS portability while maintaining sufficient performance. This miniaturization strategy could eliminate the fragile and costly turbo pump and result in a new generation of rugged high-pressure MS instruments weighing <5 pounds with a battery life from 8-24 hours, depending on the choice of roughing pump. Further increases to operational pressures should be possible with smaller traps and a high-pressure ionization source.

5.6 Tables and figures

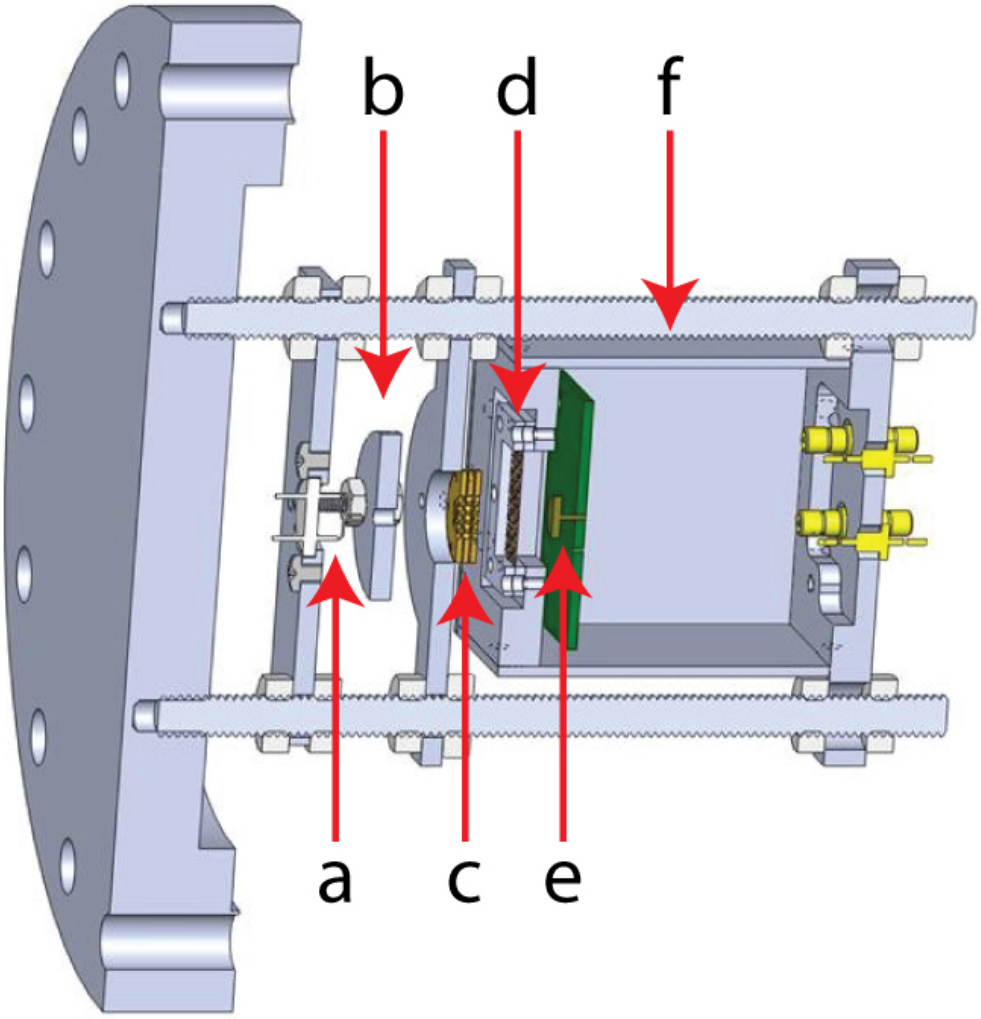

Figure 5.1: Model of isobaric CIT MS instrument mounted on a 6” CF flange. The hot cathode EI source (a), ionization gate electrode (b), 19 hole CIT array (c), detector shield grid (d), CTIA detector (e), and detector shield box (f) are mounted on threaded rods for alignment.

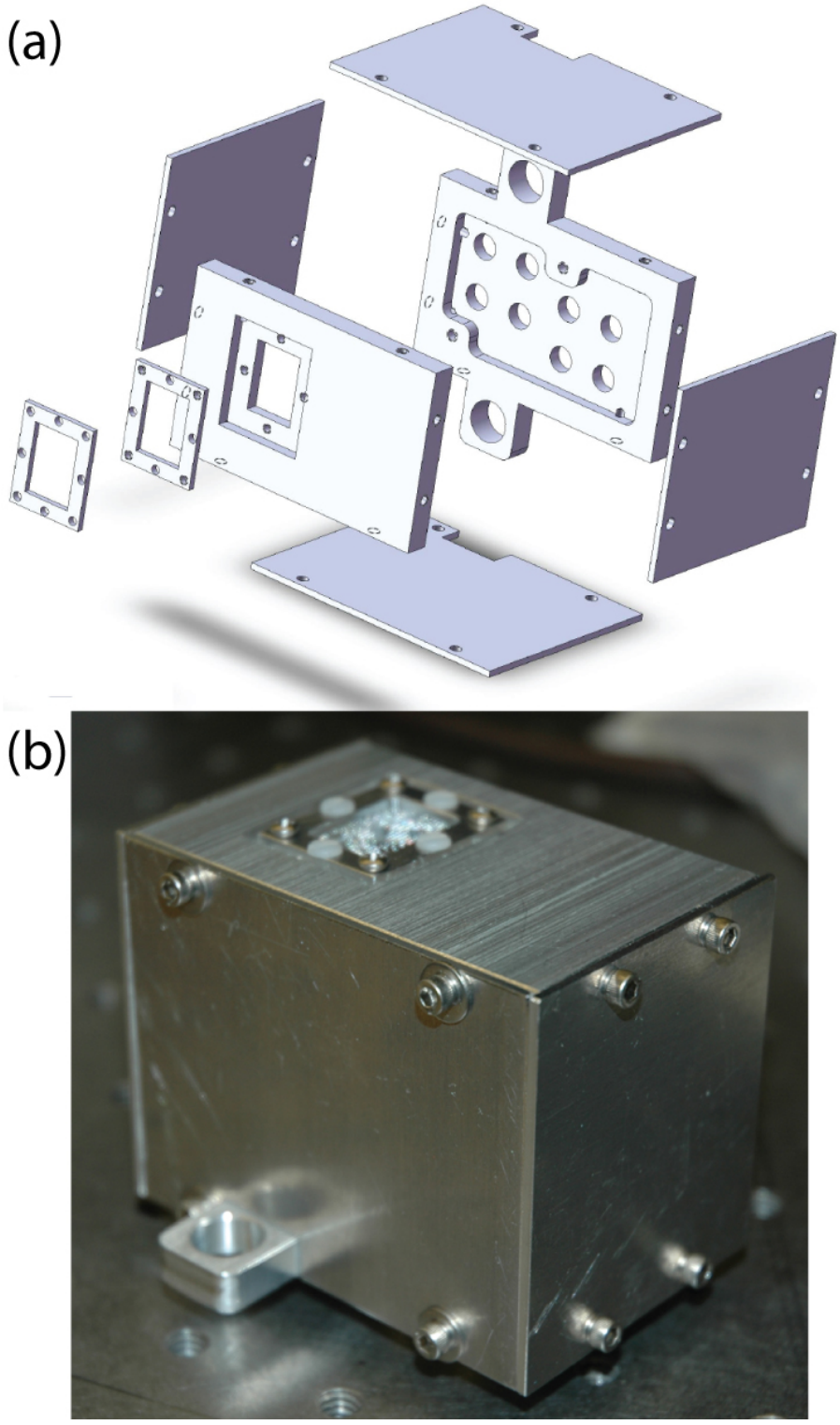

Figure 5.2: (a) Exploded CAD drawing of CTIA detector shield box and (b) finished box showing the isolated mesh grid where ions strike the detector.

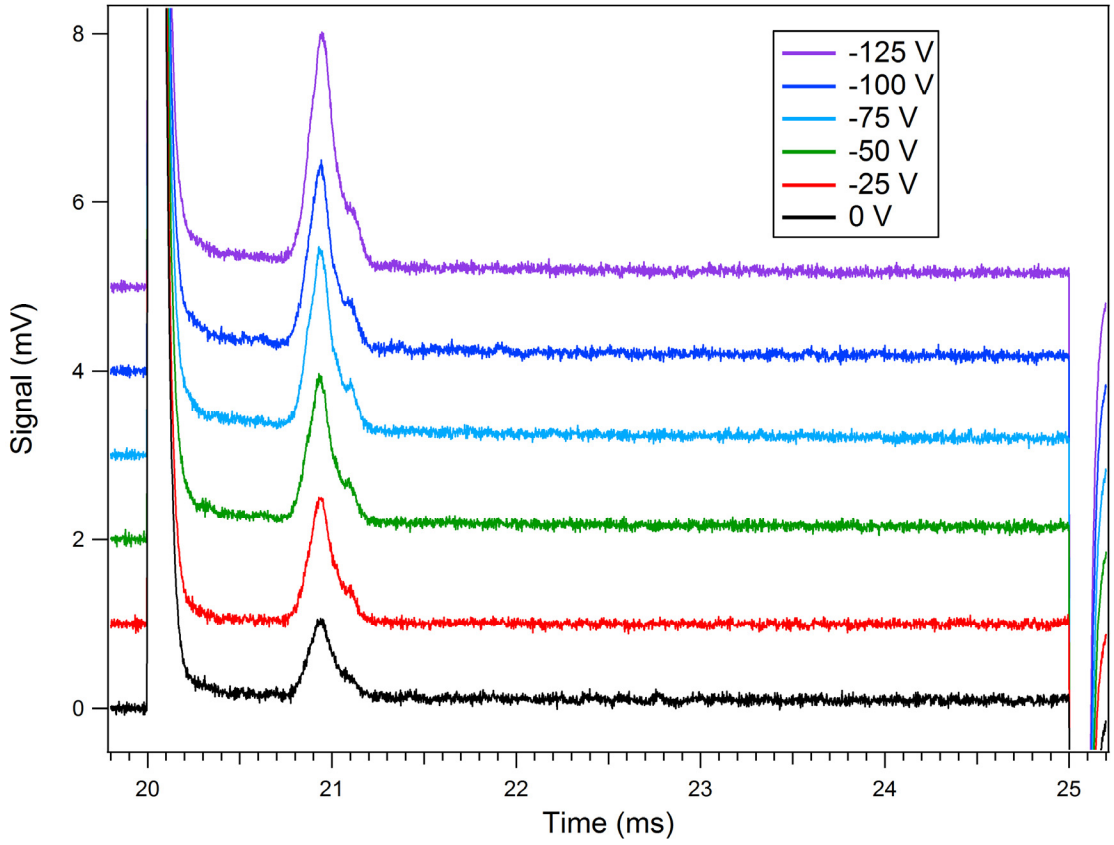

Figure 5.3: Xe^+ signal intensity decreases as the CTIA bias voltage is decreased toward 0 V. This is consistent with the negatively biased Faraday cup electrode attracting more positive ions.

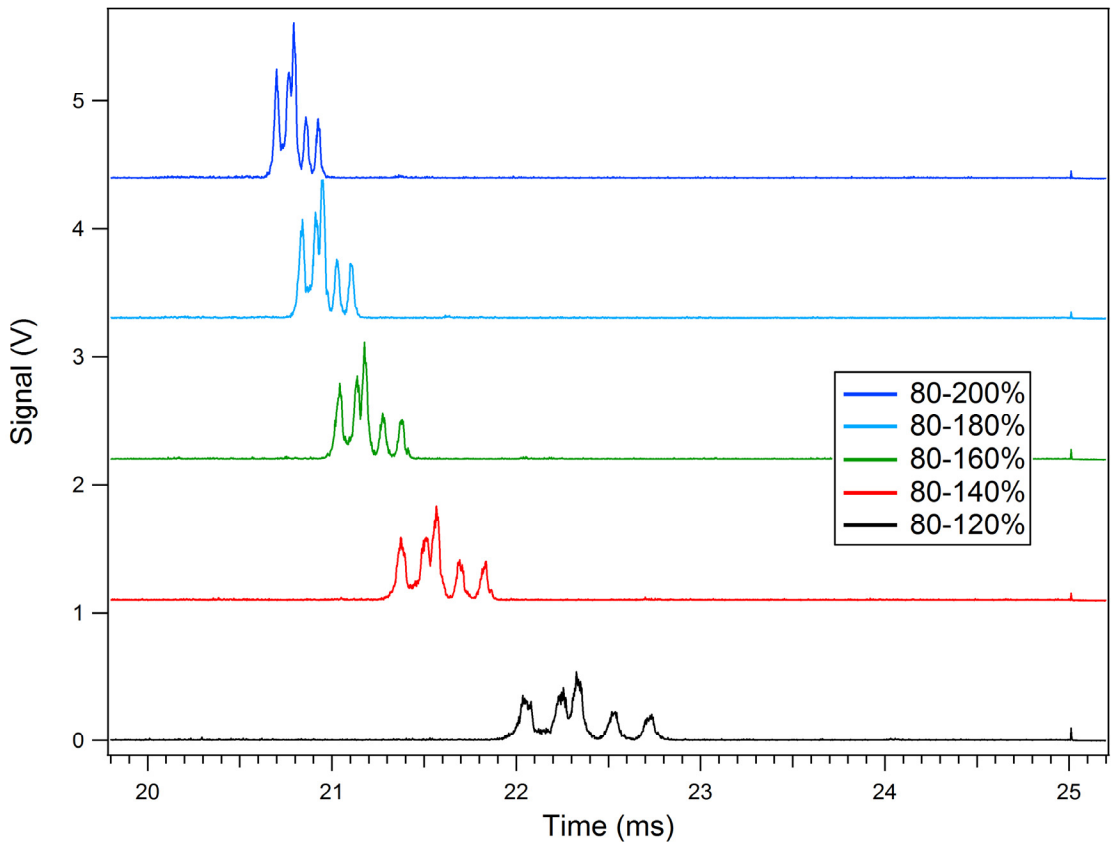

Figure 5.4: The mass scan rate of the instrument was varied to illustrate the characteristic time response of the electron multiplier detector. Individual Xe^+ peaks are clearly visible and the resolution is not limited by the detector.

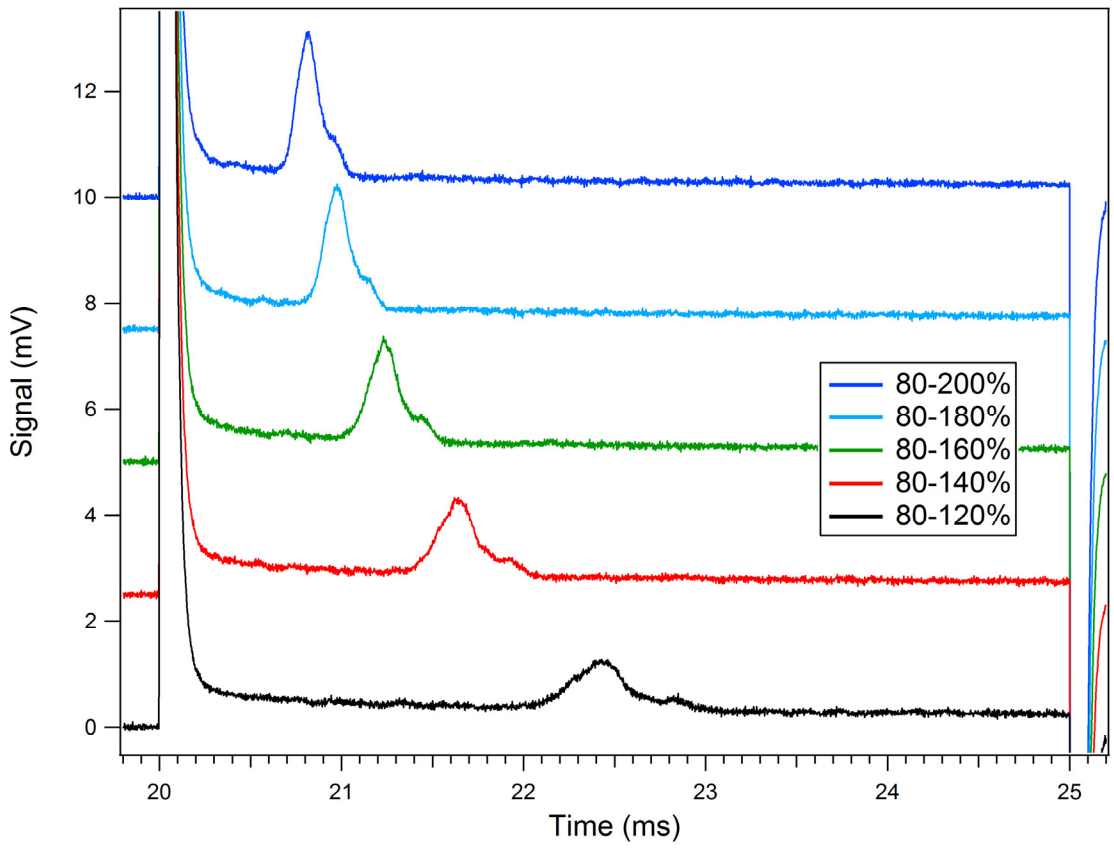

Figure 5.5: The mass scan rate of the instrument was varied to illustrate the characteristic time response of the CTIA detector with first generation signal isolation circuitry. Individual Xe^+ peaks are not visible in this experiment because the resolution is limited by the signal isolation circuitry.

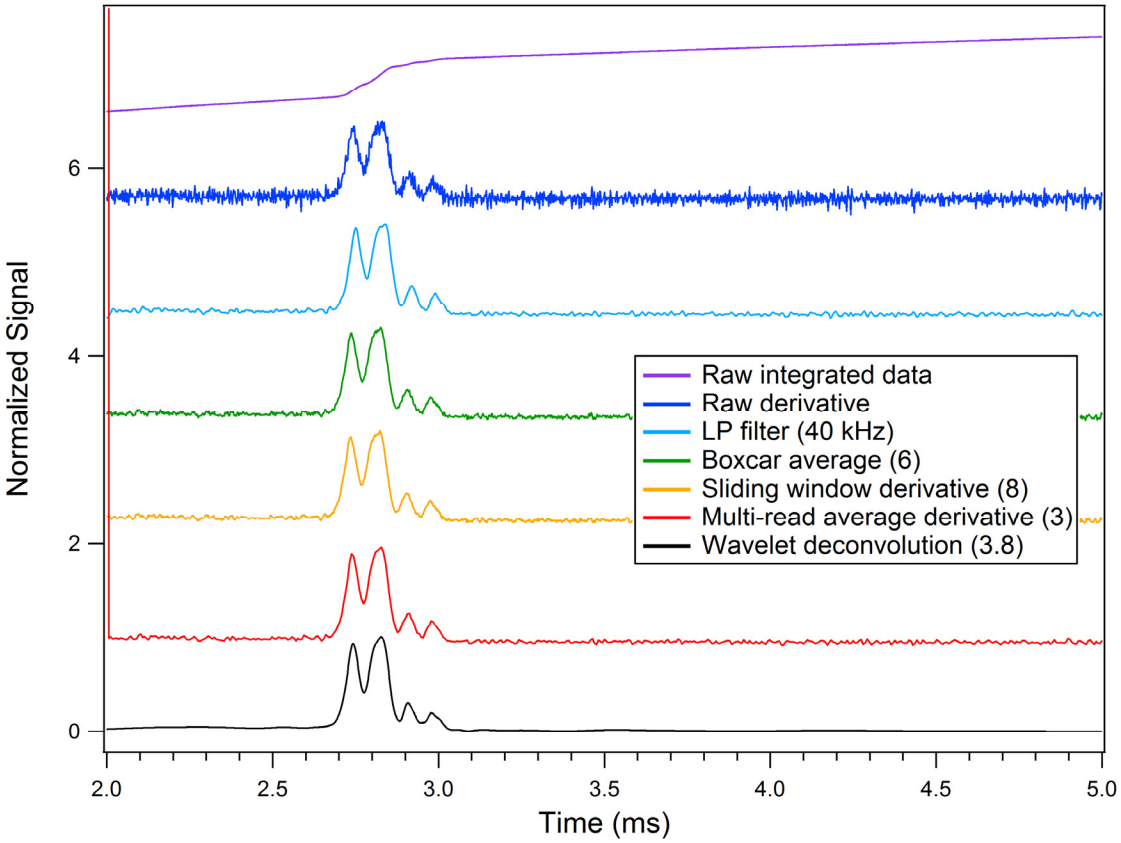

Figure 5.6: Effects of signal processing on a representative CTIA Xe^+ spectrum at 260 mTorr. The S/N in the original integrated data is high but taking a numerical derivative decreases S/N due to noise amplification. Application of various signal processing algorithms improved the final S/N. The algorithm performance is very similar except for the wavelet deconvolution algorithm which produced significantly lower baseline noise.

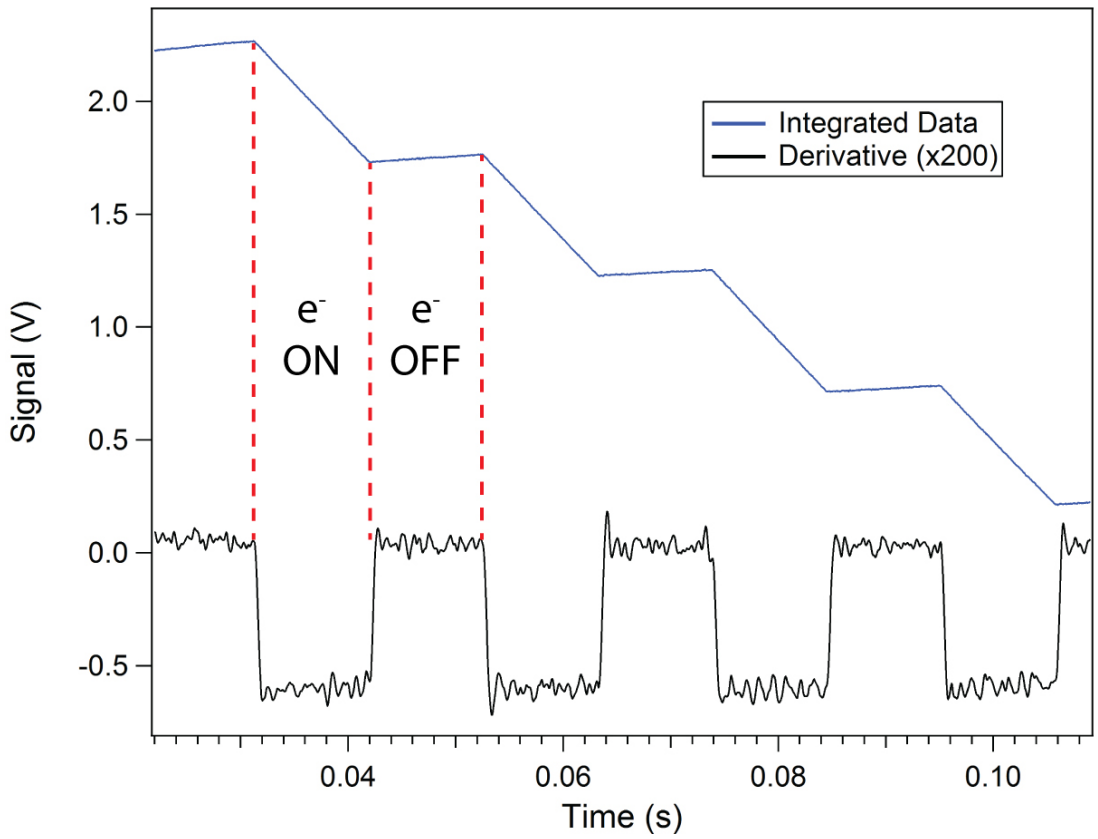

Figure 5.7: A gated electron beam produces negative integration slopes on the CTIA detector output. Taking the numerical derivative recovers the shape of the four original electron pulses from the EI source.

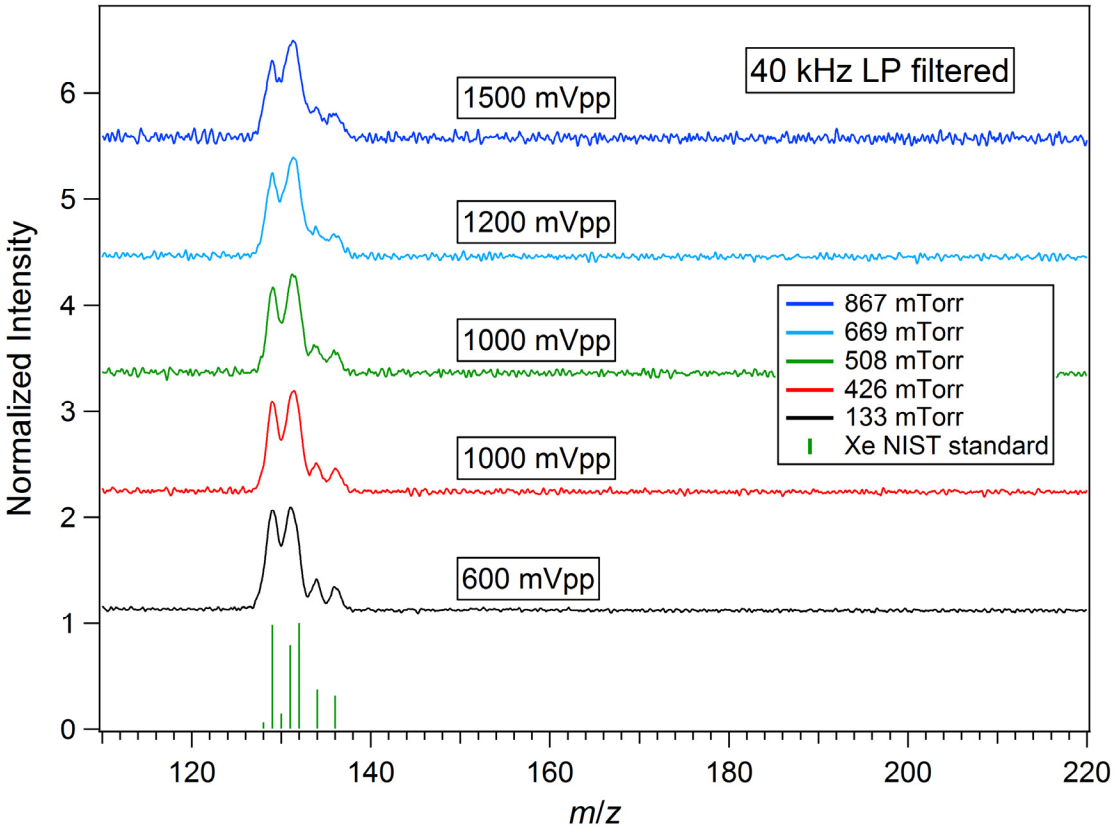

Figure 5.8: Xe^+ spectra taken with He buffer gas pressures from 133 to 867 mTorr. Peak widths remain relatively constant but there is a decrease in S/N (about a factor of 3 from 133 to the highest pressure) due to decreasing EI source effectiveness at very high pressures. Optimization of spectra required increasing axial RF peak-to-peak amplitude, ionization time (IT), and emitter bias (EB) to improve signal strength at high pressures.

				FWHM (m/z)				
Pressure (mTorr)	**Axial RF (mVpp)**	**IT (ms)**	**EB (V)**	**129**	**131**	**132**	**134**	**136**
133	600	15	-70	1.07	0.87	0.76	0.74	0.76
426	1000	50	-70	0.91	0.92	0.86	0.73	0.94
508	1000	50	-70	0.87	0.94	0.84	0.86	0.84
669	1200	50	-99.2	1.05	0.94	0.97	0.89	1.07
867	1500	75	-120.1	1.15	0.94	1.11	0.83	1.11

Table 5.1: High-pressure peak width analysis for Xe^+ *m/z* = 129, 131, 132, 134, and 136. Instrument parameters optimized at each pressure are also shown.

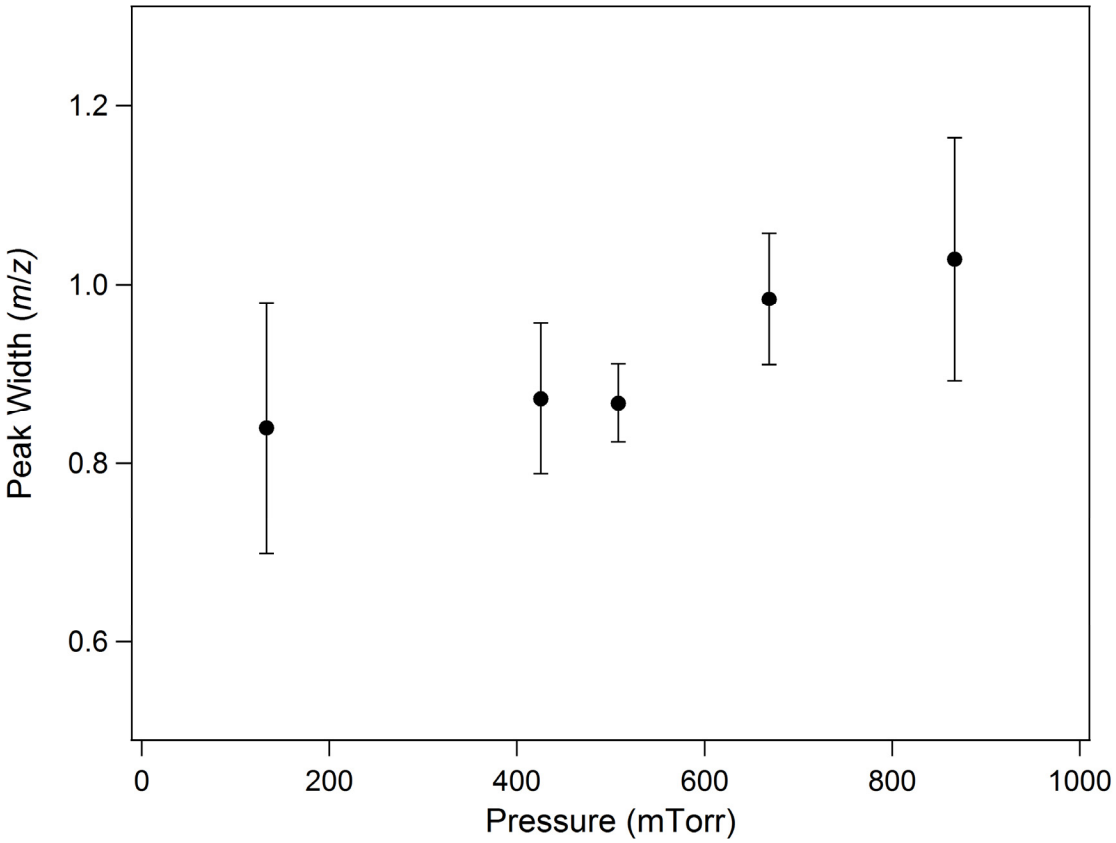

Figure 5.9: Effects of He buffer gas pressure on average peak width for the five most abundant Xe^+ isotopes (m/z = 129, 131, 132, 134, and 136). Error bars show the peak width standard deviation at each pressure value.

5.7 References

(1) Goeringer, D. E.; Whitten, W. B.; Ramsey, J. M.; McLuckey, S. A.; Glish, G. L., *Anal. Chem.* 1992, *64*, 1434-1439.

(2) Xu, W.; Song, Q.; Smith, S. A.; Chappell, W. J.; Ouyang, Z., *J. Am. Soc. Mass Spectrom.* 2009, *20*, 2144-53.